LOW-TEMPERATURE CATALYTIC SYNTHESIS of BORON NITRIDE NANOTUBES by ALKALI METAL FERRITES

by

MUSTAFA BAYSAL

Submitted to the Graduate School of Engineering and Natural Sciences
in partial fulfillment of
the requirements for the degree of
Doctor of Philosophy

Sabancı University
January 2018

LOW-TEMPERATURE CATALYTIC SYNTHESIS of BORON NITRIDE NANOTUBES by ALKALI METAL FERRITES

APPROVED BY:

Prof. Dr. Yuda Yürüm
(Thesis Supervisor)

Prof. Dr. Emin Arca

Prof. Dr. Fatma Yüksel

Prof. Dr. Melih Papila

Assoc. Prof. Dr. Selmiye Alkan Gürsel

DATE OF APPROVAL: 03/01/2018

ABSTRACT

LOW-TEMPERATURE CATALYTIC SYNTHESIS of BORON NITRIDE NANOTUBES by ALKALI METAL FERRITES

Mustafa Baysal

PhD Dissertation, January 2018

Advisor: Prof. Dr. Yuda Yürüm

Keywords: BNNT, Catalytic CVD, Thermal CVD, Catalyst, $KFeO_2$, Alkali Metal Ferrites, Nanostructure growth

Chemical Vapor Deposition (CVD) is an advantageous technique that allows synthesis of boron nitride nanotubes (BNNT) of high purity in large volumes. The product quality and energy efficiency of the CVD processes are mainly governed by the appropriate choice of catalyst. In this study, we achieved BNNT growth by alkali metal ferrites with thermal CVD (TCVD) method. Three steps were applied through the whole research. **i)** Before proposed new catalyst for BNNT synthesis, conventional catalyst system (MgO and Fe_2O_3) was utilized for BNNT production between 1000 ^oC and 1200 ^oC with TCVD growth vapor trap (GVT) approach. Moreover, CVD system parameters were investigated. The temperature was found to be the most crucial factor to BNNTs to form. **ii)** To reduce BNNT synthesis temperature, we report the use of a novel alkali based catalyst, $KFeO_2$, to trigger the BNNT formation by TCVD. When $KFeO_2$ was replaced with the conventional catalyst, BNNT synthesis temperature was reduced to 750 ^oC – 800 ^oC, which is significantly lower than the typical temperatures of TCVD reported in the literature (1100 ^oC -1300 ^oC). Growth mechanism and effect of alkali metal were investigated. **iii)** To support the idea of alkali assisted BNNT synthesis, other alkali metal ferrites from Cs to Li were used in the BNNT synthesis with TCVD. It was proved that without alkali metal catalyst in the growth vapor BNNT synthesis was not possible at temperatures below 1000 ^oC. Moreover, synthesis temperature and final morphology changed depending on the alkali metal used as in ferrite form.

ÖZET

BOR NİTRÜR NANOTÜPLERİN ALKALİ METAL FERRİTLERLE DÜŞÜK SICAKLIKTA KATALİTİK SENTEZİ

Mustafa Baysal

Doktora Tezi, Ocak 2018

Tez Danışmanı: Prof. Dr. Yuda Yürüm

Anahtar Kelimeler: BNNT, Katalitik Kimyasal Buhar Biriktirme (KBB), Termal KBB, Kataliz, $KFeO_2$, Alkali metal ferrit, Nanoyapı Büyümesi

Kimyasal buhar biriktirme (KBB) büyük hacimlerde yüksek saflıkta bor nitrür nanotüplerinin (BNNT) sentezlenmesine olanak tanıyan avantajlı bir tekniktir. KBB işleminin ürün kalitesi ve enerji verimliliği esas olarak uygun katalizör seçimi ile yönetilir. Bu çalışmada, BNNT'ler termal KBB (TKBB) metodu kullanılarak alkali metal ferritlerle sentezlenmiştir. Araştırma üç basamakta çalışılmıştır. i) Yeni kataliz önerilmeden önce, geleneksel katalizörlerle (MgO ve Fe_2O_3) BNNT'ler 1000 - 1200 ^oC arasında TKBB metoduyla kimyasal buhar tuzaklama yaklaşımıyla büyütülmüştür. Ek olarak, KBB sistem parametrelerinin ürüne etkisi incelenmiştir. BNNT'lerin oluşumundaki en önemli faktörün sıcaklık olduğu belirlenmiştir. ii) BNNT sentez sıcaklığını düşürmek için özgün alkali tabanlı katalizör, $KFeO_2$ önerilmiştir. $KFeO_2$ geleneksel katalizör ile değiştirildiğinde, BNNT sentez sıcaklığının, literatürde bildirilen tipik TKBB sıcaklıklarından (1100 ^oC -1300 ^oC) oldukça düşük olan 750 ^oC - 800 ^oC 'ye düştüğü görülmüştür. Buna ek olarak nanotüp büyüme mekanizması ve alkali metal etkisi incelenmiştir. iii) Alkali metal yardımıyla BNNT sentezi fikrini desteklemek için, Cs'den Li'ye kadar diğer alkali metal ferritler TKBB ile BNNT sentezinde kullanılmıştır. 1000 °C'nin altındaki sıcaklıklarda BNNT sentezinin, reaktif gazlar arasında alkali metal katalizörü olmadan mümkün olmadığı kanıtlanmıştır. Dahası, sentez sıcaklığının ve nihai morfolojinin, ferrit formunda kullanılan alkali metala bağlı olarak değiştiği görülmüştür.

To my mother, Şengül Baysal

Unconditional one…

ACKNOWLEDGEMENTS

First of all, I would like to express my gratitude and special thanks to my advisor Prof. Dr. Yuda Yürüm for his guidance through my PhD. Ever since I was in Sabancı university, he was always there for me with his endless support, patience and wisdom. Thanks to him, I never felt alone through my academic life, he always backed me up and motivate me during my research. He taught me how to stand on my own feet and gain my scientific self-confidence by trusting my ideas and my work. He prepared me for my professional life both academically and socially. He is the kindest person that I know, treats people with compassion and respect without separating them according to age or any difference. Hopefully, one day I can be as polite as him.

I would like to thank Prof. Dr. Melih Papila for his guidance and support during my research. His comments were always valuable to me and improve my knowledge and perspective.

I would also like to thank the members of my advisory committee, Assoc. Prof. Dr. Selmiye Alkan Gürsel, Prof. Dr. Emin Arca and Prof. Dr. Fatma Yüksel, for reviewing my thesis and valuable comments.

Also, I would like to thank all professors of materials science and engineering department for their contributions to my scientific education. Especially Prof. Dr. Mehmet Ali Gülgün and Prof. Dr. Yusuf Menceloğlu for being there every time I needed. Every conversation with them prepared me for my professional carrier.

Furthermore, I would like to thank our project partners, Assoc. Prof. Dr. Çınar Öncel for his advices and knowledge, and Yelda Yorulmaz. Without them this study could not be completed.

I would like to thank Hasan Kurt, Güliz İnan Akmehmet, Canhan Şen, İpek Bilge for their friendship and fruitful conversations. I also would like to thank my group members. Alp Yürüm, Ezgi Dündar, Aysu Yurduşen, Zahra Gohari Bajestani, Sahand Harzand and all MAT family. It was great being a part of this team.

Very special thanks go for my bros, Kaan Bilge, my idea partner and Oğuzhan Oğuz. Living with them and sharing academic and social life was a privilege. Most of the academic curiosities were realized by our endless discussions and different point of views.

Additionally, I must separate whole paragraph for my best friend in Sabancı University and İstanbul, the one and only true angel; Melike Mercan Yıldızhan. She is the one always who was there for me with her endless compassion and patience. Her joy for life is so overflowing, she infected everyone around her. I would like to thank her forever for her support and guidance. I learned too much from her.

A very special thank goes to Suna Tepeli for her caring presence and endless positivism. I always found comfort and peace on her eyes.

Finally, I would like to express my sincerest gratitude to my whole family, especially the reason of my very existence; my mother Şengül Baysal, my sisters Atiye Eşsiz and Nurdan Aydıner for their unconditional love and support.

TABLE OF CONTENTS

TABLE OF FIGURES

LIST OF TABLES

CHAPTER 1

1 INTRODUCTION

1.1 Summary

After the Iijima's first report of carbon nanotubes (CNTs)[1], nanotube structures drew attention due to their unique properties (high surface to bulk ratio, high anisotropy) against their bulk structures. This high interest towards the nanotube structure from the literature, initiated development of new inorganic tubes and application areas [2, 3]. Amongst these inorganic tubes developed in 25 years, boron nitride nanotubes (BNNTs) are probably the one that attracted the most attention after CNTs. BNNT is structurally analogous to CNT. Nevertheless, the hexagonal network consists consecutively ordered boron and nitrogen atoms instead of graphitic carbon atoms [4]. In addition to structural similarities, BNNTs and CNTs have close mechanic properties and thermal conductivities [4]. On the other hand, due to their composition differences, BNNTs demonstrate high chemical [5], and thermal stability (oxidation stability up to 1100^{o}C) [6], piezoelectric properties [7, 8], neutron screening [9] and superhydrophobic [10, 11] properties. Apart from these, BNNTs are insulating materials with wide band gap (5-6 eV) due to their partially ionic nature. Moreover, their band gap is independent of nanotube diameter and chirality unlike CNTs [12]. As consequences of all these unique properties, BNNT is considered as a potential candidate in nanoelectronics (nano insulators, nanosensors), optic applications (Deep-blue and infrared lasers), magnetic application (targeted drug delivery), biomedical applications (scaffolds, biosensors), energy applications (hydrogen storage), ceramic and glass composites and polymeric composites.

Despite all these unique properties and potential applications of BNNTs, synthesis of material is still in development process. After the first production by Chopra et al. in

1995 [13], there had been many efforts made in the synthesis procedure. In general, arc discharge, laser ablation, pressurized vapor condensation, atom deposition, plasma-jet method, reactive ball milling, substitution by CNTs and chemical vapor deposition method were used to synthesize BNNT. All methods that had been used in BNNT synthesis have some advantages and drawbacks; More detailed information can be found in somewhere else [3, 4, 14]. Besides these production methods, CVD technique can be considered as one of the most important techniques and most used one in the literature [15, 16]. Since CVD technique was successfully applied for the mass production of CNTs for years with high quality and purity. Also, easy adaptability of CVD system in laboratories and relatively low operation temperatures make this method more applicable. From this point of view, CVD technique has privilege over other methods for BNNT production on behalf of industrialization. However, using CVD technique was not straightforward as expected. Unlike CNTs BN crystallization requires high temperatures and low solubility of BN in metals limits the use of traditional metal catalyst [17]. BNNT growth by CVD using borazine has many examples in the literature[18-21] but were not considered as common as other CVD methods. Most significant developments of CVD growth of BNNTs were achieved by boron oxide based CVD, commonly known as BOCVD [22, 23] and thermal CVD (TCVD) methods [24-26]. BOCVD method was designed based on a vertical induction furnace, which operates at high temperatures (1000 ºC – 1700 ºC) and creates a large temperature gradient. Tang et al. first introduced this method by producing BNNT using MgO as a precursor [22] then Zhi et al. [23] further developed the method by introducing FeO and MgO as a catalyst system. Since then, many studies based on BOCVD were conducted for producing a large quantity of BNNTs. Nevertheless, the specific design of the experimental setup restricted its extensive usage by other research groups. In 2008 Lee et al. [24] used thermal

CVD method in a specific way by trapping precursor vapors in an inner tube which called growth-vapor trap CVD. In this approach, the traditional horizontal furnace was coupled with quartz tube vacuum system and inner small quartz tube for trapping without using any specific attachments. Although produced BNNTs were not in large quantities compared to the BOCVD, they demonstrated that BNNTs could be grown on the substrate and inner walls of the crucible. In addition, pattern growth of BNNTs on the specifically coated substrates was enabled in another work of this method [25]. Even though there were many attempts using different catalytic materials such as Ni, Co, MoO_3, V_2O_5, CuO, PbO, FeO, Fe_4N [3, 17, 27, 28] for increasing the BNNT growth efficiency, same catalytic materials contain FeO/Fe_2O_3 and MgO as precursors were used in both BOCVD and TCVD methods due to efficiency of catalytic system. The MgO/FeO system proved itself as one of the most efficient precursors for creating B_2O_2 vapor at temperatures above 1100 ^oC for large quantity BNNT production.

In 2011, Huang et al. first introduced Li_2O as a new catalyst for BNNT synthesis for BOCVD system.[29] By using Li_2O, they obtained small diameter BNNTs in large quantities due to high oxidation capacity and promotion effect on crystallization of Lithium. Furthermore, in 2013, Li et al. used same precursors by using ball milling procedure.[30] To the best of the authors' knowledge, these are the only examples of the application of alkali metal oxide as a catalyst in BNNT synthesis. However, using Li_2O requires relatively high temperatures to create Li vapor that can partially condense afterwards as an active catalyst in VLS mechanism.

Studies used FeO/MgO or Li_2O as an active catalyst in BNNT synthesis were usually conducted at temperatures around or beyond the boiling point of metallic forms of Mg and Li, 1091 ^oC, 1330 ^oC respectively. In conclusion, most of the CVD synthesis of BNNTs were conducted over 1000 ^oC. In this study, we aim to introduce new catalytic

materials for BNNT synthesis by just using conventional horizontal furnace, which open up a new way of commercialization of BNNTs due to the low synthesis temperature, energy efficient synthesis with CVD method. Moreover, new catalytic materials used in this study brings a breath of fresh air to catalytic material research on BNNT growth with CVD which is mostly stuck to the same catalytic materials that only work over 1000 ^{o}C. Additionally, and most importantly, low temperature BNNT synthesis of this work can instantly be used on the hybrid composite or electronic device fabrication fields like the direct growth of BNNTs on ceramic or polymeric fibers or different substrates, which loses structural integrities at high temperatures over 1000 ^{o}C.

In the first part of this work, existing conventional catalysis (MgO and Fe_2O_3) system was used for BNNT production between 1000 ^{o}C and 1200 ^{o}C with GVT TCVD approach. Although this catalyst system is the most commonly used one for CVD synthesis of BNNT, for every different system and experimental conditions, BNNT structure was changing. Since, small perturbations on the system like precursor particle size, efficient vapor trap, affect the final product. Effect of CVD process parameters (maximum temperature, flow rate, and heating rate) on the growth quality and the aspect ratio of synthesized BNNTs with conventional catalyst were experimentally investigated. A systematic optimization study was performed to design the experiments at the settings of reaction temperature (f_1), heating rate (f_2) and reactive gas flow rate (f_3). Three main responses such as substrate coverage, film thickness, and BNNT aspect ratio were considered.

The second part of this work focused on reducing BNNT synthesis temperature in TCVD approach by introducing new catalyst system that allows BNNT formation and crystallization at low temperatures. From this point of view, BNNT synthesis

temperatures by CVD may be further reduced by using high vapor pressure metals in their oxide form as a catalyst. Potassium can be considered as a good candidate due to its high vapor pressure (B.P. = 759 ^{o}C) compared to the other metals, but it is not stable in air, reacts vigorously with water. In addition, its oxide form is also highly reactive, and direct usage of potassium oxide (K_2O) is restricted by the unstable nature of the compound, which prevents most of the potential application of K_2O as a catalyst. Here, we demonstrate that highly crystalline BNNTs can be synthesized efficiently at as low as 800 ^{o}C by using potassium ferrite ($KFeO_2$) as a catalyst which might serve as a parent material for K/K_2O as an active catalyst and with iron oxide species for B_2O_2 formation.

Given the success of $KFeO_2$ in TCVD and the effect of potassium as a new catalyst for the BNNT production, the other alkali metal ferrites were further investigated in order to have a better understanding of the role of the catalyst in the growth process. Consequently, $CsFeO_2$, $NaFeO_2$, and $LiFeO_2$ were used to introduce new catalytic materials that can be utilized and developed for BNNT synthesis at different temperatures. $CsFeO_2$ which has the highest partial pressure did not give successful BNNT growth due to the very low temperatures and very high molecular diameter. On the other hand, BNNT growth was achieved with $LiFeO_2$ above 1000 ^{o}C and $NaFeO_2$ at 900 ^{o}C. Different BN morphologies like BN microtubes were also observed with these catalysts. In conclusion, with the help of the alkali metal oxides, BNNT growth and crystallization temperature were reduced as low as 750 ^{o}C. Moreover, different yield and morphologies were obtained at various temperature ranges according to the alkali metal used as a catalyst.

CHAPTER 2

2 LITERATURE REVIEW

2.1 Boron nitride

Boron nitride (BN) is a chemical compound, which is not found in nature, only form after synthetic routes. Balmain first synthesized BN in 1842 by reaction of the molten boric acid with potassium cyanide. [31] It was a binary compound formed the same composition of boron and nitrogen atoms. Its properties (polymorphism and mechanical properties) are very close to the carbon, instead of other nitride compounds formed by same group elements such as gallium nitride.[2] BN can be formed in amorphous or crystalline form. Crystallization of BN is very similar to the graphite and diamond; it occurs either layered or tetrahedrally attached structure depending on the synthesis conditions. This correspondence can be summarized as BN is isoelectronic and isostructural to carbon.[32] Like carbon, there are different polymorphs exist for BN with different properties. Four different polymorphs of BN are classified as hexagonal BN (h-BN), rhombohedral BN (r-BN), cubic BN (c-BN) and wurtzite (ɣ-BN) in Figure 2.1.

In h-BN, layered hexagonal units contain sp^2-hybridized B and N atoms are held together by Van der Waals forces. The structure is analogous to graphite. Layered construction can also be arranged in the rhombohedral structure (r-BN), which consists of a shifted phase of three layers of BN (ABC). The second most common form of BN after h-BN is c-BN, which is similar to the diamond structure. It is the second hardest material known. The rare form ɣ-BN resembles lonsdaleite. Both c-BN and ɣ-BN are tetrahedrally bonded form of BN.[33]

This work is focused on h-BN, specifically about h-BN nanotubes. Information about other BN structures can be found in the literature, especially on c-BN.[34-36]

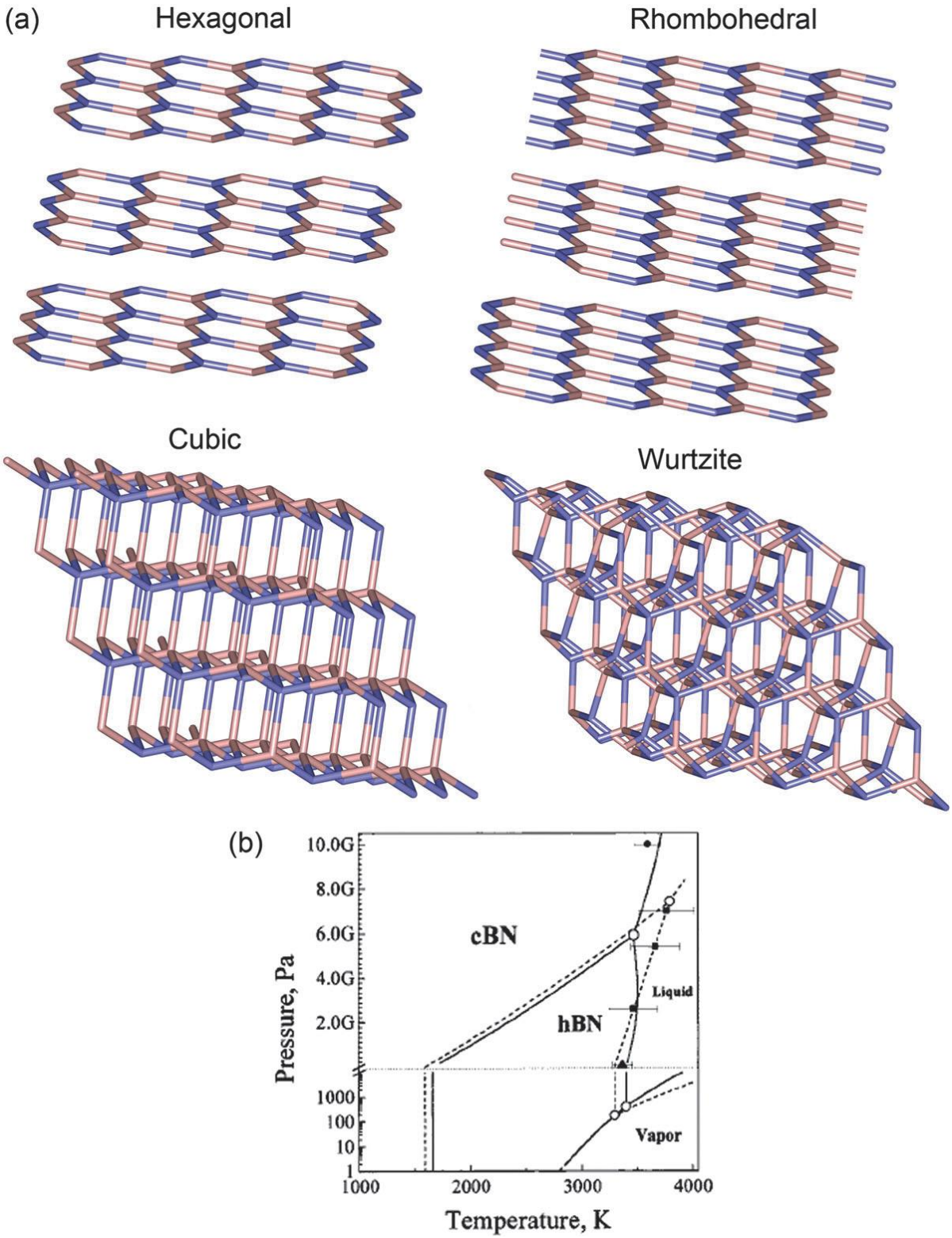

Figure 2. 1: A) Four different polymorphs of BN B) Phase diagram of BN. (adapted from reference 34)

2.1.1 Boron nitride nanotubes

Three years after the discovery of CNTs, Rubio et al. proved BNNTs theoretically in 1994 [12, 37]. One year later, BNNTs were successfully produced by arc-discharge method [13]. As mentioned before, BNNTs are structural analogous of CNTs. Boron and nitrogen atoms ordered alternatingly in the hexagonal network instead of carbon atoms in a graphitic sheet with almost same atomic distance. Increasing interest in one-dimensional materials with pioneering structure CNT, BNNT has been attracting more attention as an inorganic nanotube due to the similar extraordinary mechanical properties, high thermal conductivity like CNTs, and more importantly insulator character of BNNTs in contrast with metallic or semiconducting CNTs.[38, 39]. Electronegativity differences of boron and nitrogen atom result in the partially ionic character of B-N bond compared to the covalent C-C band in CNTs. As a result, BNNTs have a large bandgap >5 eV and independent of diameter, morphology, and chirality of the tubes.[37] Moreover, BNNTs possess many advantages compared to the CNT, such as higher thermal and chemical stability (detailed information was given in 2.1.2). However, the number of studies conducted on BNNT in the literature is surprisingly lower than CNTs as shown in Figure 2.2. According to the search on Web of Science database based on keywords, the number of publications about CNTs are 50 times higher than BNNTs and additionally only 128 studies were conducted about CVD synthesis of BNNTs between 2000 to 2015. A significant factor that limits the exploration of BNNTs, is not because it does not attract attention, but because of the very challenging synthesis of BNNTs compared to carbon based nanomaterials.[3] Most of the well-defined techniques for CNTs do not work on BNNTs due to the requirement of excessively high growth temperatures, specialized equipment and dangerous chemicals for BNNT synthesis. [4]

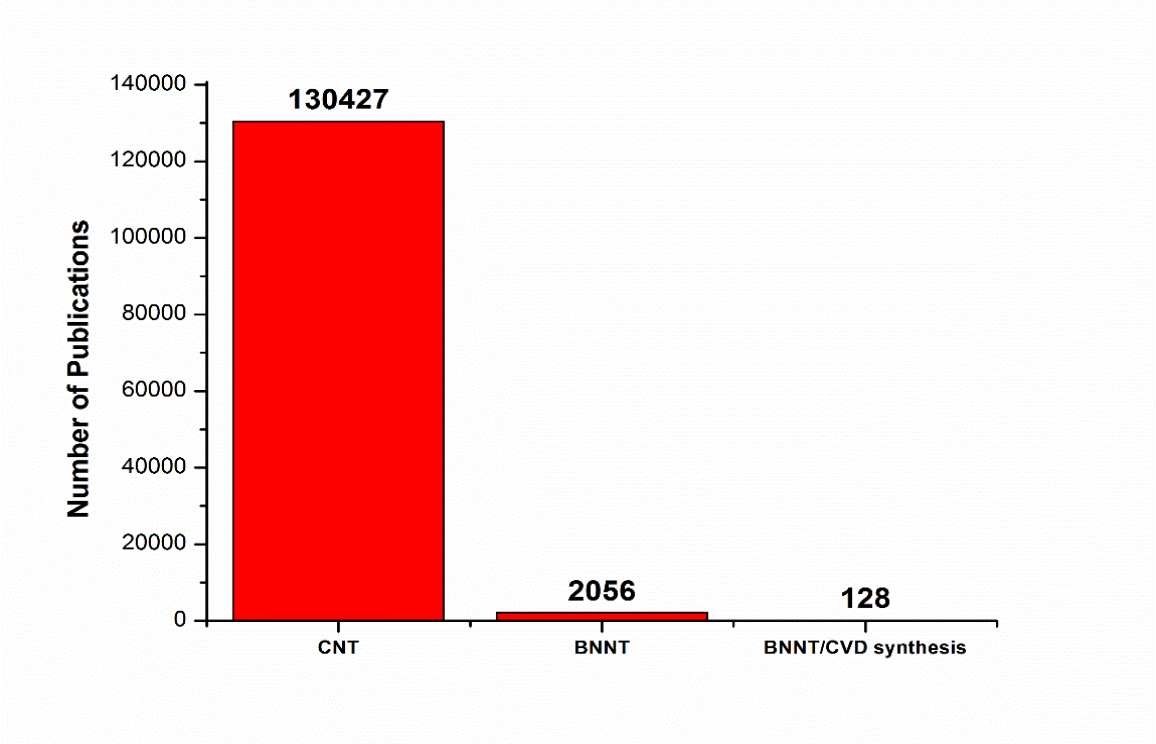

Figure 2. 2: The number of publications on CNT, BNNT, and CVD-BNNT between 2000 and 2015 (ISI Web of Science database)

2.1.2 BNNT properties

Unique characteristics of BNNTs demonstrate high chemical stability [5], high thermal stability (oxidation stability up to 1100^{o}C) [6], high thermal conductivity [40], piezoelectric properties [7, 8, 41], neutron screening [9], deep UV emission[42], transparency at visible region[43] and superhydrophobic [10, 11] properties. All properties were summarized in this chapter.

- Morphology of BNNTs

BNNTs can be formed in single wall or multiwall structures. However, single walled BNNTs are not common like single walled CNT. Generally, double or multiple walled structures are formed due to the ionic nature of the B-N bond. The partial ionic character of the band causes so-called “lip-lip interaction” between BN layers. Because of this, layers were stacked on each other that result in multiwall formation and structure stabilization. On the other hand, weak interactions between carbon layers

result in the easy formation of single-wall CNTs. Interlayer distance between two walls in BNNT are very close to the characteristic d spacing of bulk h-BN (0.33 nm).[44]

Helicity of the sheets relative to tube axis gives a limited number of conformations. Three types of helicities are possible for nanotube formation from a hexagonal layer. For hexagonal lattice, we can define two vectors (n, m) and unit cell is made of 2 atoms. For "armchair conformation," two vectors should be equal, and the angle is 30°. For "zigzag conformation," m is equal to 0 and angle is 0° as well. In addition, for helical conformation varying degrees are possible. In Figure 2.3, possible conformation and resulting single wall BNNTs were shown.

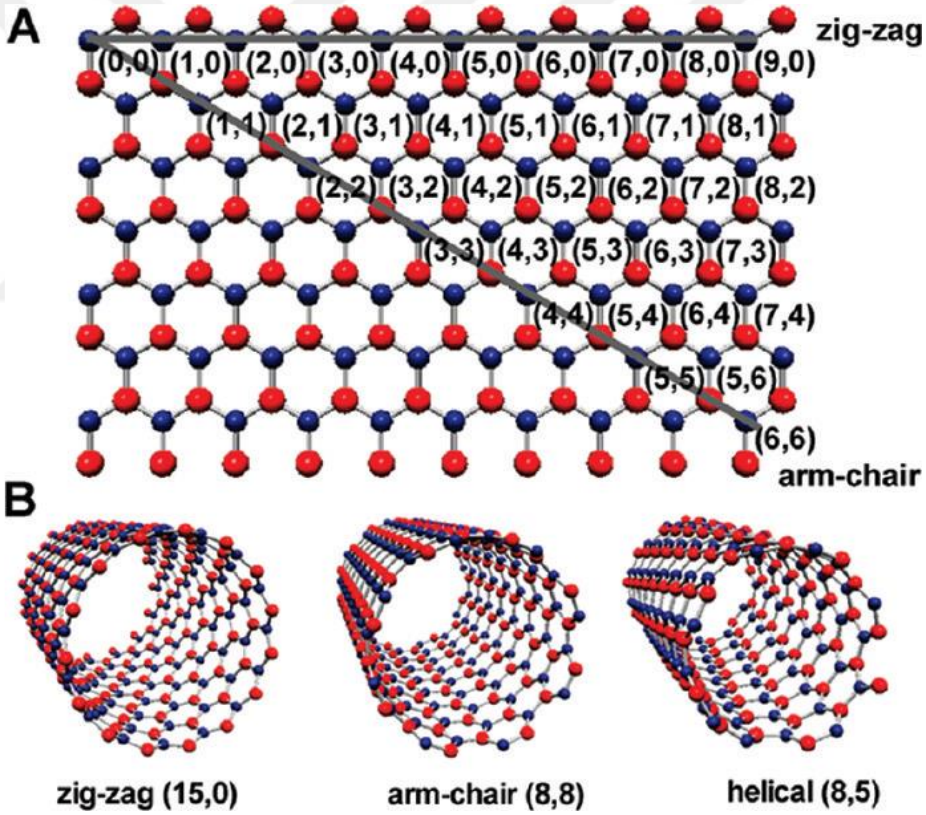

Figure 2. 3: A) BN sheet with possible nanotube formation directions shown with (n,m) indices. (B) Ball and stick structural models of BNNT, zig-zag (15,0), arm-chair (8,8), and a helical (8,5). red and blue balls represent B and N atoms, respectively. (Adapted from reference 3)

All conformations are equally possible for nanotube formation. However, for BNNT case, the zigzag or near zigzag formation was commonly reported by researchers with minor armchair and helical configurations. The reason for that, BN tends to crystallize

perfectly in layers due to the strong interactions of the consecutive layers very close to the bulk h-BN. This leads to the same orientation of layers in multiwalled BNNTs. On the other hand, for CNTs, all conformations were equally possible because of the degree of freedom in neighboring lattices leads to the wide variety of helicities.

- Thermal properties

BNNT properties are always compared with CNTs in the literature. Thermal properties of BNNTs are also one of them. Thermal stability of multiwalled BNNTs synthesized at 1500 ^{o}C in air was found to be 1100 ^{o}C, much higher than CNTs which is around 500 oC.[6] It means that oxidation resistance of the BNNTs much higher than its counterpart CNTs.[5, 45] Modelling on the BNNT ropes showed that oxidation of the BNNTs start with B_2O_3 formation at 950 ^{o}C, then vaporization occurs around 1200 ^{o}C.[5]

Another crucial thermal property of the BNNTs for nanocomposite applications is thermal conductivity. Theoretical studies showed that thermal conductivity BNNTs is similar to that of CNTs. In fact, larger low-temperature thermal conductivity is expected for BNNTs at the same phonon mean free path compared to the CNTs.[46] At room temperature, researchers measured the thermal conductivity of BNNTs with a diameter of 30-40 nm as 350 W mK^{-1}.[47] The measured value is very close to the measured thermal conductivity of CNTs with the same diameters [4].

- Mechanical properties

BNNTs have similar mechanical stiffness like CNTs. The elastic modulus of the individual MW-BNNTs was measured by thermal vibration method and found to be 1.2 TPa.[48] Experimentally calculated value consistent with the theoretically calculated results.[49] Therefore BNNTs are the stiffest material with insulating properties. In addition, another theoretical work showed that BNNTs has lower elastic modulus but higher yield resistance. [50] Lastly, in 2013, measurements from 16 individual tubes give

Young's modulus, and shear modulus of the BNNTs are 1800 ± 300 and 7 ± 1 GPa, respectively.[51] In another work, exceptional shape recovery of the BNNTs was observed after releasing the load for bending.[52]

- Electrical properties

As mentioned before, BNNT has wide band gap like other nitrides due to the partial ionic nature of the BN bond. Moreover, the band gap of the BNNTs is independent of the tube wall number, diameter, and chirality. Instead, armchair nanotubes have an indirect band gap, whereas, zigzag tubes have a direct band gap.

Another important aspect about BNNT is its tunable band gap. The band gap of the BNNTs can be tuned by doping with carbon, applying transvers electric field and radial deformation. Theoretical studies showed that carbon substitution on BNNTs causes n or p-type semiconductor BNNTs by controlling carbon doping.[53] Radial deformation cause decrease in bandgap from 5 eV to 2 eV on zigzag BNNTs.[54] By this way, BNNTs can be used in a visible range in optical applications. In addition, calculations show that applying transvers electric field should decrease or completely removed band gap of BNNTs[55, 56].

- Magnetic applications

Many theoretical works were conducted to reveal magnetic properties of the BNNTs. Substitution with carbon cause induced spontaneous magnetization of BNNTs of zigzag nanotubes. It appeared magnetism disappeared in the armchair configuration. Magnetic properties of the BNNTs can also be changed with adsorption of other molecules on the BNNTs, for example, Fe_3O_4 introduction to the BNNT or Fe nanoparticle coverage. In addition to that, authors showed that F adsorption on boron sites in BNNTs cause enhanced magnetization. There are also other works on piezoelectric properties of

BNNTs[7, 41]. Studies show that under electrical field axial deformation of the BNNTs was up to 1 % which is almost 9 times higher than conventional ceramics. [8]

- Optical properties

It is known that the BNNTs are a good candidate for deep UV applications, since band gap of the BNNTs gives absorption peak around 205 nm. First, cathodeluminescence experiments of BNNTs gave strong absorption band around 320 nm and a weak band at 223 nm. Then, optical adsorption measurements showed two small bands at 325 nm and 260 nm with strong band 210 nm (5.9 eV). Later, researchers found that adsorption bands depend on the quality of the nanotubes. Highly crystalline BNNTs demonstrate one strong band at 205 nm (6 eV) without any subbands.

- Thermal neutron adsorption

BNNTs with $_{10}$B-enrichment showed far better thermal neutron adsorption than its bulk structure. Highly crystalline multiwall structure of BNNTs increase the efficiency of the solid-state neutron detectors.[57]

- Other properties

Toxicity of the BNNTs is still controversial; there are numerous studies based on the BNNT toxicity. However, depending on the experimental conditions that assessment was conducted, most of the studies showed BNNTs are non-toxic. More information about toxicity can be found in detail somewhere else.[58]

The Super hydrophobic behavior of vertically aligned BNNTs on the substrate was discovered by Lee, although BN thin films showed hydrophilic behavior.[11] Nanoscale surface roughness is believed to be the reason for this properties. Also, other researchers found similar results for BNNT thin films, randomly oriented BNNTs and BN nanosheets.[10, 59, 60]

2.1.3 BNNT applications

As consequences of all these unique properties, BNNT is considered as a potential candidate for various applications. These applications are summarized below.

- Hydrogen adsorption

Nanomaterials always attracted more attention compared to the bulk structures due to their high surface to volume ratios. BNNTs have higher hydrogen adsorption capacity compared to the CNTs. It is known that carbon materials have weak binding with hydrogen. On the other hand, partial ionic nature of the B-N bonds cause induced dipole moment which make hydrogen adsorption stronger [61]. Ma *et al*. also reported MW-BNNTs could adsorb 1.8 to 2.6 wt.% hydrogen at 10 MPa for MW-BNNTs and bamboo like BNNTs respectivly[62]. This number even upgraded by using collapsed BNNTs, experimentally reported hydrogen uptake at 10 MPa is 4.2 wt.% [63].

- Polymeric composites

Thanks to the exceptional thermal and chemical stability, high thermal conductivity, dissipation of visible light and piezoelectric properties of the BNNTs, polymeric composite application of the BNNTs seems promising. NASA produced electromechanical energy conversion devices by BNNT/polyimide composites. Composites can withstand extreme space conditions [41] [64]. Last decade, interest in BNNT/polymer nanocomposites increased. In 2006, PS/BNNT composites were prepared, and transparent films were produced by 1 wt. % BNNT addition due to the white color of the BNNTs. Also, the elastic modulus of the as-prepared films increases 21 % compared to the pure polymer film [65]. Another group worked on PMMA/BNNT composites; they also found 19 % increase in elastic modulus, however tensile strength and elasticity were decreased with BNNT addition [66].

In the case of thermal properties of the polymeric nanocomposites, BNNTs have a little effect on antioxidation and glass transition temperature of matrix[67, 68]. On the other hand, the thermal conductivity of the nanocomposites increased significantly, PMMA films with 10 wt.% BNNT showed 3 times better thermal conductivity than raw films [66]. This indicates that polymeric nanocomposites with BNNT as filler can be used in electronic coatings and applications with heat emission are essential. Recently 30 wt.% BNNT addition in epoxy resin was achieved by functionalization with POSS. The thermal conductivity of the BNNT/epoxy resin was increased 1360 % [69]. In another work, PVA sheets were prepared with electrospinned PVA fiber with 10 wt.% of BNNTs reinforced. During electrospinning, fibers and BNNTs were aligned. After processing (Hot pressed at 90 ^{o}C) fully transparent sheets were produced and thermal conductivities of the films were increased threefold [70].

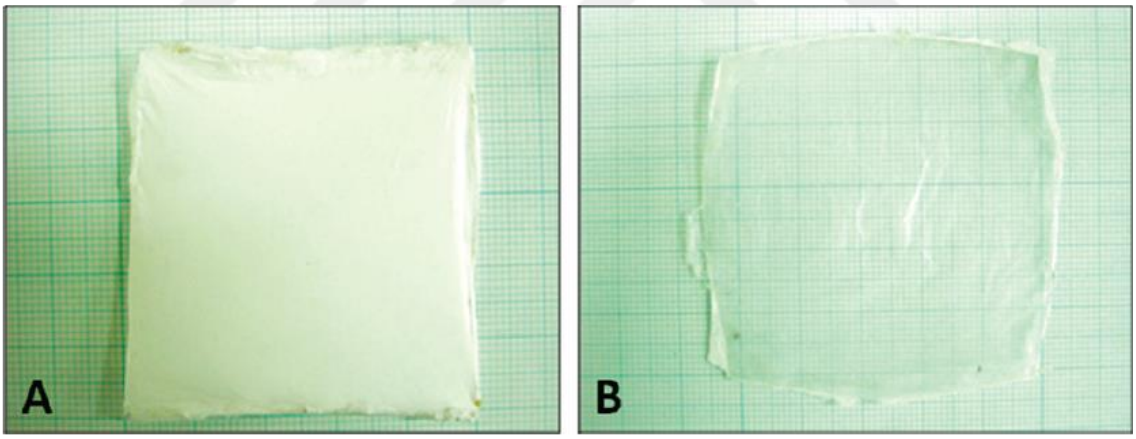

Figure 2. 4: BNNT/PVA sheet before (A) and after (B) hot pressing (Adapted from reference 3)

- Ceramic composites

BNNTs found some application in ceramic composites as a reinforcement. There are several studies used BNNT in the industrial glass as a softening agent, for example, 4% of BNNT loading in barium-calcium aluminasilicate glass increased fracture strength and fracture toughness 90% and 35% respectively [71]. In addition, BNNTs were used with conventional ceramics Al_2O_3 and Si_3O_4, and BNNT addition causes significant

improvement of high temperature superplasticity. Moreover, ceramics became more deformable [72].

- Nanoelectronics

BNNTs can be used as a nano insulator. Researchers proposed insulated cables using BNNTs with metallic or semiconducting wires inside [44]. However, there are still some unsolved issues for this technology due to the low interaction between BNNTs and metals. Coating with BNNTs is one of the possible solutions for the problem. In addition, using sandwich like tube formation, BN coated CNTs, or BCN tubes can be produced [73, 74].

- Deep UV laser and nanosensor and field emitting device applications

For UV lasers, BNNTs can be utilized instead of GaN lasers due to their large band gap. Direct band gap and defect free BN give stable luminance peak at 215 nm [75]. For this point, using highly crystalline BNNTs (only one adsorption peak around 205 nm) can also be used in laser systems and significantly decrease the size due to the small dimension of the nanotubes.

BNNT based pH sensor production was reported by using biotin-fluorescein functionalized MW-BNNTs with Ag particles. The spatial resolution of the sensor was spot size and diameter of the BNNTs. By using BNNT based pH sensor, environmental pH of the living cell could be monitored [76].

Many potential applications were proposed for BNNTs from biomedical to aerospace field. However, the realization of the potential applications always run into obstacles related to the slow progress of the BNNT synthesis.

2.2 Synthesis techniques of BNNTs

Synthesis techniques for CNTs are also used for BNNT synthesis, although the success of the techniques is not at the level of CNT production. Most of the applied techniques were modified for BNNTs synthesis due to the high temperature requirements and low solubility of BN in the catalyst. Methods can be classified into two categories according to the temperatures used; high temperatures synthesis over 2000 ^{o}C and low-temperature synthesis below 2000 ^{o}C.

2.2.1 High-temperature techniques

High-temperature techniques mostly conduct on over vaporization point of the Boron. Most used ones are arc-discharge, laser ablation and modified methods generalized as high temperature and pressure methods for large scale production

- Arc-discharge

Arc discharge method was the first method used for synthezing BNNTs. Due to the insulator nature of the compound, BN powder filled tungsten electrode used as anode and copper rod was a cathode. Single and multi-walled BNNTs were produced however final product contained metal impurities and BN structures [13]. Then, the method was improved by using conductive boron compounds as an electrode. Luisao used HfB_2 rods as an electrode, and single and double wall BNNTs were synthesized [77]. ZrB_2 and YB_6 were also used for electrodes [78, 79]. Researchers also used conductive electrodes by melting boron with Ni and Co and produced BNNTs by arc-discharge method [80]. Later arc jet technique was applied for continuous production of single and MW BNNTs at high temperatures (5000-20000 K) [81]. With the arc-discharge method, smaller diameter nanotubes can be synthesized, however, low yield, different BN structures and metal impurities from electrode were disadvantages of the technique.

- Laser ablation

Golberg first used this method in 1996 by using single crystal c-BN or h-BN source under high pressure N_2 with a CO_2 laser at 5000 K [82]. A significant amount of BN flakes and particles were found in the final product. With this method, catalyst-free BNNTs can be produced. Then, the method was improved by using catalyst particles and BN source in the synthesis [83]. Bulk quantities of BNNTs were produced by using laser heated rotating BN target under N_2 atmosphere [84]. In 2007, the method was used to synthesize high yield single and multiwall BNNTs with the h-BN target and continuous CO_2 laser under N_2 at 3500 ^oC [85]. Nevertheless, final samples usually contain unwanted BN morphologies except for tubular structures.

- Modified methods

❖ Pressurized vapor condenser/High Temperature High Pressure (HTP) method

In 2009, significant development of high yield BNNT synthesis was achieved by laser evaporation technique called pressurized vapor condenser method by NASA [86]. The technique used higher laser power than other laser ablation process. High power CO_2 laser (wavelength of 10.6 μm) was used to evaporate boron target in the chamber, which is filled with high-pressure nitrogen gas (6 to 14 bar). NH_3 reacted with boron vapor at 4000 K. Upward steam of boron vapor over 4000 K in nitrogen allowed to form liquid boron droplets as nucleation sites without any catalyst. Metal wires were used as a condensation sites, which promotes BNNT fibrils growth. The method was further developed by Tiano, using higher pressures chamber (68 bars) and 2.5 kW CO_2 laser [38]. Resulting BNNTs were highly crystalline, exceptionally long, and 2 to 5 walled. However, a considerable amount of boron particles and BN structures also formed inside the BNNT fibrils.

- Inductive thermal plasma methods

Further improvement of HTP system was made in 2014 [43]. A laser source, inherently small spot size limiting the area exposed, was changed with large volume induction plasma source which increased BNNT production rate significantly. In this process, at atmospheric pressure, BN powder source and the N_2/H_2 mixture were fed to the system through the plasma region which operates over 8000 K. BNNTs below 5 nm diameter were produced with this method in large quantities. Authors claimed that hydrogen gas in the system promotes the BNNT formation.

The same year, a similar system called extended pressure inductively coupled plasma (EPIC) was build that operated with plasma power between 40 to 50 kW [87]. High pressure nitrogen and boron source were used in the induction plasma system without hydrogen gas. Small diameter BNNTs (2-6 walled) were produced. However, entangled BNNTs contained solidified boron and BN side products.

2.2.2 Low temperatures techniques

These methods are operated under 2000 ^oC below the melting point of boron. The low energy demand of these methods attracts the attention of researchers for reducing the price and leads to worldwide usage of BNNTs. Most used ones are reactive ball milling/annealing, carbothermal synthesis, and CVD methods.

- Reactive ball milling annealing method

In this approach, precursor materials were mixed under ammonia or nitrogen gas in a pressurized vessel via stainless steel balls that causes defective BN based structures. Then, further annealing between 1000 – 1300 ^oC led to the formation of BNNTs mostly in bamboo-like morphology. Chen et al. first introduced the method in 1999 by ball milling of B powder under 3 bar NH_3 atmosphere for 150 hours, then annealing at 1200 ^oC [88]. The method was further developed and extensively used by the same group using boron ink [30, 59, 89, 90]. Boron ink sample was prepared by first ball milling B powder in

the N_2/NH_3 atmosphere for about 150 hours before applying catalyst ($Fe(NO_3)_3$ or $Co(NO_3)_2$) in ethanol. Then, boron ink was annealed under NH_3 or N_2 between 1000 – 1300 ^oC around 6-8 hours. After the process, bamboo like BNNTs was produced with diameters ranging between 50 to 80 nm and with lengths over 100 μm. However, the as-synthesized material was in the form of bamboo and suffered from impurities such as BN layered structures, amorphous boron particles, which were very hard to purify, and metal particles from ball milling process.

- Carbothermal synthesis/templated synthesis

Another low temperature method is the substitution method that CNT used as a template for BNNT growth. Han et al. used CNTs to synthesize BNNTs by substitution of C atoms with B, and N. CNTs were mixed with B_2O_3 and heated at 1500 ^OC under nitrogen in the induction furnace [91]. C was oxidized while B and N take their place. BNNTs were synthesized with a diameter very close to the CNT template. The method was further used with SWCNTs. However, the final product has carbon impurities, BC and B-C-N nanotubes. The major drawback of carbon templated BN structures is carbon based impurities, which were reduced by Golberg by using MoO_3 as a promoter [92]. Most effective promoters were found MoO_3, CuO, and PbO. In addition, porous Al_2O_3 templates were also employed in BNNT synthesis at 1200 ^oC [93, 94].

- CVD

CVD synthesis of BNNTs can be considerably more explored compared to the other methods for BNNT synthesis. Still, further improvements are necessary to use it as a conventional method. Information about CVD can be found in chapter 2.3

- Other synthesis methods

Plasma enhanced pulsed-laser deposition (PE-PLD) method was successfully applied by Wang et al. in 2005. BNNTs were grown vertically and highly crystalline on the substrate decorated with catalytic Fe particles. BNNTs with a diameter of 10 to 20 nm were produced at 600 ^{o}C substrate temperature. However, resulting BNNTs are very short in length (Figure 2.5).

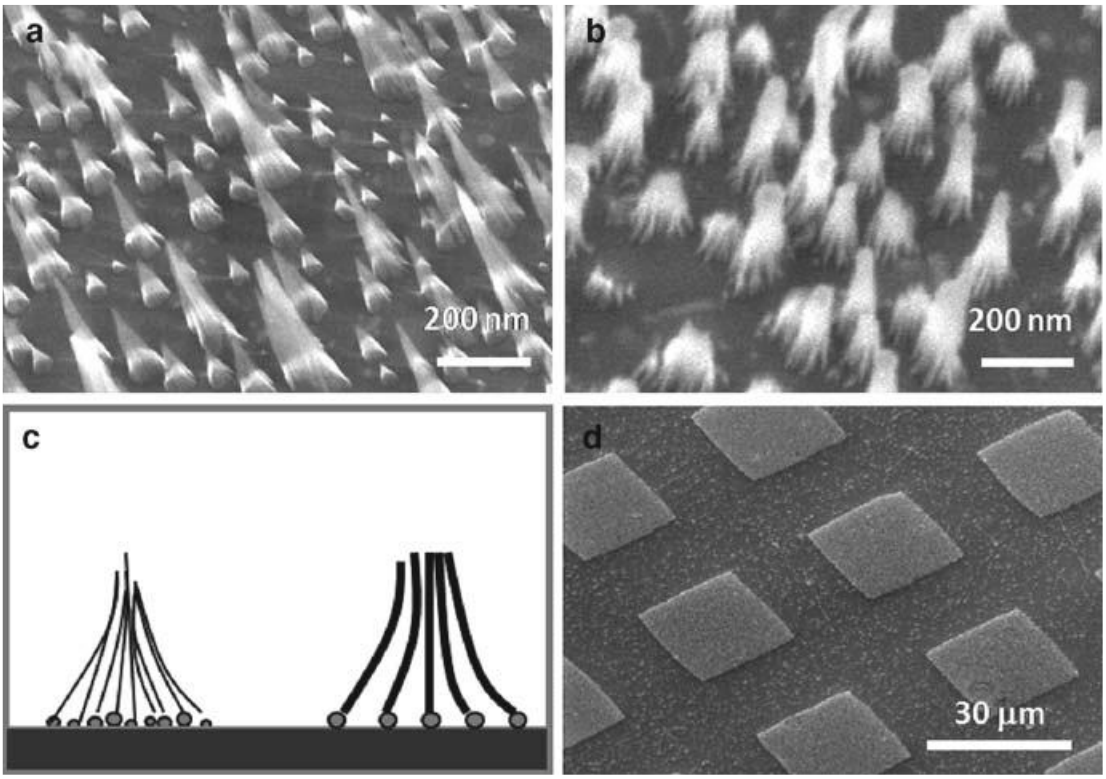

Figure 2. 5: Aligned BNNTs by PE-PLD technique

In addition, the autoclave was also applied to produce BNNTs at low temperatures around 600 ^{o}C. However, a limited number of attempts were made using this approach due to the low crystallinity of the resulting material and unreacted boron based impurities [95, 96].

2.3 CVD in BNNT production

CVD is a significant method, which frequently used in CNT production. For CNT synthesis, CVD is widely explored and parameters of the system is mostly optimized due to the well-understood carbon chemistry and role of catalyst. For now, CNT

production with CVD is commercialized since the high amount of well crystalline CNTs can be produced at low temperatures. From these points, researchers have tried to adapt CVD method for BNNTs due to the successful synthesis of similar structures. However, unlike CNT which has lots of valid carbon source and catalytic materials, suitable precursor materials for BNNT production are limited especially as a boron source due to the toxic nature of the boron-based gases and unavailability of the well-defined catalyst for BNNT synthesis [17, 42].

Early attempts through the CVD synthesis mostly focused on liquid boron sources. Sen *et al.* used $LiBH_4$ and $(NH_4)_2SO_4$ to produce H_3N: BH_3 for the pyrolytic growth of the BNNTs [18]. However, only small number of BNNTs were observed. Shelimov et al. used 2,4,6-trichloroborazine ($B_3N_3H_3Cl_3$) as precursor and micrometers thick BN fibers were produced [19]. A significant development was achieved in 2000 by Lourie et al.[20].They used borazine ($B_3N_3H_6$) that derived from $NaBH_4$, $(NH_4)_2SO_4$ and CoO_4 then produced borazine were pyrolyzed at 1100 ^oC with Nickel Boride (Ni_2B) catalyst. At high temperature, borazine was decomposed to form BN, which dissolved in Ni_2B particles. After saturation, BNNTs precipitated on the catalyst particles. However, resulting nanotubes were bamboo like with bulbous, flag and club-like tips and their diameters were around micrometer size. Kim conducted promising work with borazine precursor by using floating nickelocene catalyst CVD in 2008 [21]. At low borazine pressure double walled BNNTs, at high borazine pressure, BN fibers were produced at 1200 ^oC. However, Ni impurities from the catalyst were found in the product. Then, the process further utilized decaborane or borazine as boron precursors with floating nickel catalyst between 1100 ^oC to 1400 ^oC [97]. Floating Catalyst system offered non-toxic boron precursor with the scalable process for double-walled BNNTs.

There were some attempts at the non-catalytic growth of BNNTs from as synthesized B-N-O sources around 1200 - 1700 ^{o}C [98-100]. Depending on the reaction parameters and oxygen content of the precursors, other morphologies were obtained. A limited number of works were published about non-catalytic CVD growth of BNNTs. In addition, there is also a small amount of study from boron base gases used as a precursor due their price, toxicity and explosive properties. Still, plasma enhanced CVD (PE-CVD) studies were reported by using Ni, Co and iron supported Fe/SiO_2-Al_2O_3 (Figure 2.6) [101-103].

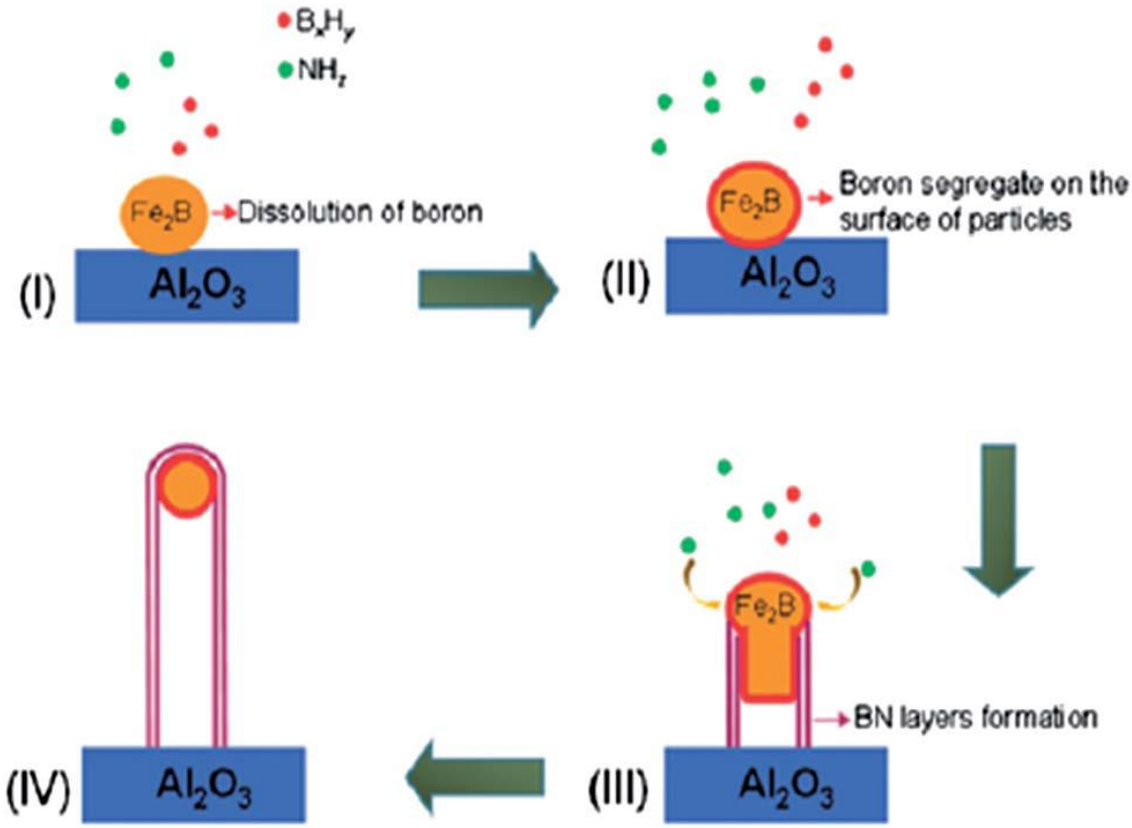

Figure 2. 6: Growth mechanism of PE-CVD method BNNT growth at reference 103

Lots of CVD growth methods with different parameters were studied during last two decades. Nevertheless, most significant development was achieved with two methods, so-called Boron oxide CVD and Thermal CVD. Researchers widely explored these two

approaches due to their promising capability of well crystalline, high yield BNNT growth.

2.3.1 Boron Oxide CVD

BOCVD method was first introduced by researchers from Japan National Institute for Material Science (NIMS). In this method, solid boron powder was used as a precursor with metal oxide catalyst. Most important specifications of this approach are elimination of toxic precursor and carbon free environment. Tang et al. first mentioned reactive boron oxide intermediate phase in 2001 by using amorphous boron powder and Fe_2O_3 with the traditional furnace, but the name of BOCVD was not used [104]. In 2002, Tang et al. introduced the technique by using amorphous boron powder and MgO powder as a catalyst with RF induction furnace [22]. After this study, the specific name of BOCVD started to be used as a combination of boron oxide intermediate and specifically designed RF induction furnace setup. A method based on the creation of reactive boron oxide (B_2O_2) intermediate vapor by reaction between amorphous boron and the metal oxide(s) at elevated temperatures, then introducing NH_3 to react with B_2O_2 vapor at lower temperature zone of the chamber where catalytic metal particles act as a solvent for BNNT growth. The specifically designed system was shown in Figure 2.7.

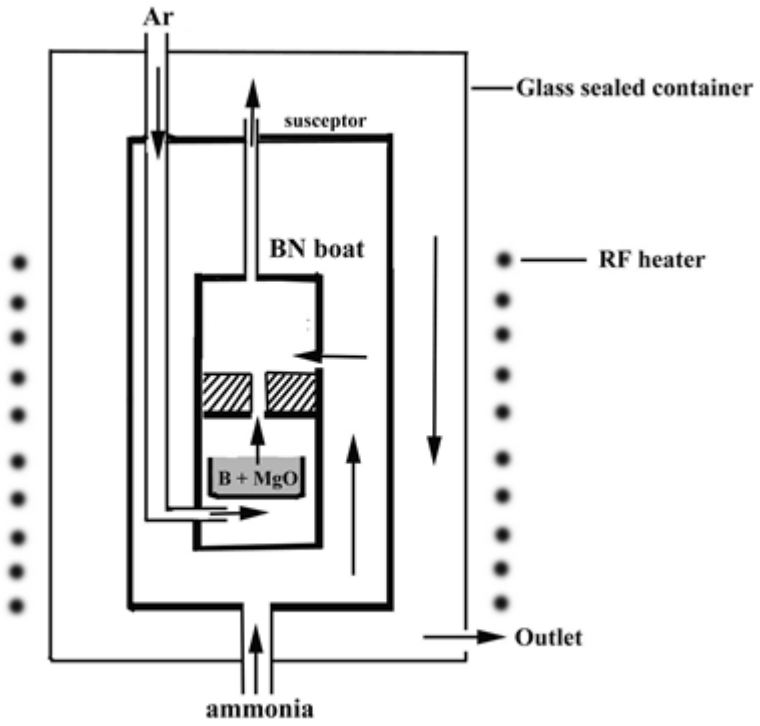

Figure 2. 7: BOCVD system setup (adapted from reference 22)

The technique includes RF induction furnace with two inlets from base and top and one outlet on the side. Amorphous boron powder and MgO was loaded in the BN crucible, which was placed in the BN reaction tube. Then, precursor mixture was heated to 1300 ^{o}C by RF induction furnace under the argon flow. At this high temperature zone, boron was oxidized by MgO to produce reactive boron oxide vapors.

$$2MgO(s) + 2B(s) \rightarrow B_2O_2(g) + 4Mg(g)$$

Then, magnesium vapor and B_2O_2 were transferred to upper zone by argon flow. In the top zone of the chamber, the temperature was controlled at 1100 ^{o}C where NH_3 gas was introduced to the system. At this lower temperature zone, B_2O_2 was reacted with ammonia in the metal vapor environment to produced BNNTs.

$$B_2O_2(g) + 2NH_3(g) \rightarrow 2BN(s) + 2H_20(g) + H_2(g)$$

After, 2 hours of reaction BNNTs were collected on the wall of the BN chamber. The diameters of the nanotubes were changing from 10 -70 nm and length of tens of micrometers. VLS mechanism was proposed for the growth. However, most of the tubes were open-ended, catalytic metal particles at the tube tip were not observed. On the other hand, with this BOCVD method, high yield BNNT production with CVD was achieved. The method was further upgraded by using FeO and MgO with B powder in 2005 [23]. The yield was exceptionally increased by increasing temperatures 1100 to 1700 ^{o}C. After that time, catalytic metal oxide double (FeO, MgO) was used to produce BNNTs for many application[52, 105, 106]. Apart from FeO/MgO, many metal oxides were also tried in the BOCVD method; however, none of them replaced existing double. Metal oxides used in BOCVD methods are listed in Table 2.1. Nevertheless, the specific design of the experimental setup and expensive parts restricted its extensive usage by other research groups; only one group used this method to produce BNNTs for further utilization.

Table 2. 1: Precursors and temperatures used in BOCVD method

Precursors	**Temperature (^{o}C)**	Catalyst	Year
[22]B, MgO	**1300**	Mg, Nanosized	2002
[107]B, GaO	**1550**	Ga	2002
[108]B, GaO	**1550**	Ga	2004
[23]B, MgO, and FeO	**1100-1700**	Fe, Mg	2005
[109]B,Li_2CO_3	**1350**	Li	2009
[29]B,Li_2O	**1350**	Li	2011
[110]B,MgO and SnO or FeO	**1500**	Mg, Fe or Sn	2014

2.3.2 Thermal CVD

Thermal CVD is another method which based on the traditional horizontal furnace and solid boron source. There were many attempts to produce BNNTs in the conventional furnace without any additional processes, specific design and expensive part but most of them were unable to achieve high quality BNNTs. Then in 2008, Lee et al. used a conventional furnace with an extra inner test tube, which is called growth vapor trap TCVD [24]. With this technique, the effective growth of the BNNTs was achieved on top of the precursor powder, inner tube, and walls of the combustion boat. In this system, the furnace was coupled with the quartz vacuum chamber (quartz tube reactor), and precursor powders were mixed and loaded into the alumina combustion boat covered with several substrates which were placed in the small quartz test tube. Then, a test tube (one end closed) was placed in the quartz vacuum chamber in a way that, avoiding direct gas flow in figure 2.8A. Precursor powder used in the GVT TCVD approach is the same as the BOCVD approach. B powder, MgO and FeO (Fe_2O_3) were used due to their effective catalyst performance for BNNT growth.

The system was evacuated before NH_3 flow at 200 sccm, then heated to 1200 ^oC and held at this temperature for 1 hour. At high temperature, B_2O_2 vapor, as in BOCVD approach was created by the reaction between B and Mg/Fe oxides. Then, growth vapor, which contains B_2O_2 and metal vapors (act as a catalyst) reacted with ammonia to form BN. Authors explained GVT approach enhance the nucleation and BNNT growth. According to the nucleation theory, probability of nuclei formation can be expressed as ;

$$P_N = Aexp(\frac{-\pi\sigma^2}{k^2T^2ln\alpha})$$

A is constant, σ is the surface energy, and α is the relative pressure of the growth species (P/P_0) where P is the vapor pressure of the growth species, and P_0 is the equilibrium vapor pressure of condensation at given conditions. At constant experimental conditions, assuming surface energy of the growth species are constant, and T is also constant, increasing the vapor pressure of the growth species (P) by trapping growth vapor result in an increase of α. Hence, the probability of the nuclei formation (P_N) for both catalyst particles and BN could be enhanced. The inner tube was allowed to trap growth vapor to increase nucleation rate, and position of the closed side of the tube does not allow to sweep away reactive vapor by gas flow before nucleation starts in Figure 2.8B.

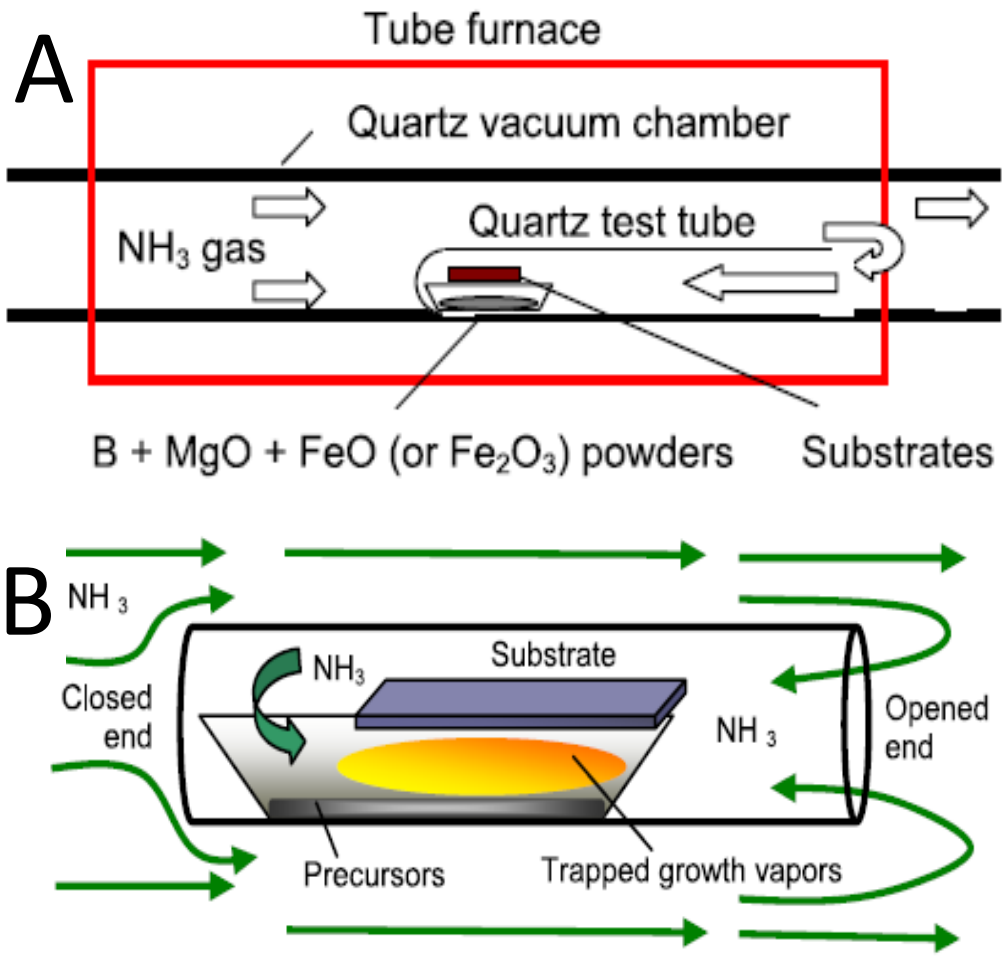

Figure 2. 8: A) GVT-TCVD system setup B) Reactive vapor trap mechanism (adapted from reference 25)

With TCVD GVT approach, as synthesized BNNTs had diameters in the range of 10 to 100 nm and the lengths were over 10 μm. Researchers proposed VLS mechanism for the nanotube growth by Mg and Fe act as a catalyst to form catalytic droplets. Next study with the same approach was published in 2010, the same group achieved vertically aligned pattern growth BNNTs on the catalytic material coated substrates [25]. Same experimental setup and precursors were used. Precursor powders were heated under NH_3 to 1100 ^oC – 1200 ^oC and Si substrates were coated with MgO, Ni, and Fe. MgO was found to be the most effective ones for BNNT growth. Highly crystalline controllable synthesis of BNNTs on the substrates was achieved by this work. Easy adaptability of the method lead to many other studies by using TCVD method for BNNT growth with or without an inner tube (Table 2.2). However, most of the studies used the same precursors and conventional MgO, FeO catalyst double. Introducing new catalyst materials for the TCVD growth of the BNNTs were rarely encountered, and these new catalysts were not able to neither decrease the BNNT growth temperature nor increase the yield compared to the conventional catalyst double [111, 112].

Table 2. 2: Precursors and temperatures used in TCVD method

Precursors	**Temperature (^oC)**	**Catalyst**	**Year**
[24]B, MgO and FeO	**1200**	Mg, Nanosized	2008
[25]B, MgO, and FeO	**1100 – 1200**	Mg, Fe	2010
[113]B, NH_4NO_3, Fe_2O_3	**1300**	Fe	2011
[27]B, MgO, and FeO	**1200-1400**	Mg, Fe	2012
[114]B, MgO, and FeO	**1350**	Mg, Fe	2013
[115]B, Fe_2O_3	**900 - 1400**	Fe	2013
[30]B, Li_2O	**1200**	Li	2013

[116]Colemanite, Fe_2O_3	**1280**	Fe	2013
[111]B, V_2O_5, Fe_2O_3 and B, V_2O_5, Ni_2O_3	**1100**	V,Fe/V,Ni	2014
[112]B/B_2O_3, NiY	**1200**	NiY	2017

CHAPTER 3

3 EXPERIMENTAL PROCEDURE

3.1 Summary

In this chapter, materials and methods of BNNT production were summarized. BNNT production technique used in this study was TCVD method; details can be seen in section 2.3.2. Even if different catalyst was introduced for BNNT synthesis, the same setup in figure 3.1 was used with some modifications. Every modification in the system was explained in corresponding catalyst experimental procedure.

Figure 3. 1: Experimental Thermal CVD setup

The main component of the system is classic horizontal furnace (Protherm PTF 12/105/900 series) coupled with quartz tube 1200 mm in length and 60 mm in diameter. Stainless steel flanges are adapted to the system with silicon rubber o-rings for gas and vacuum connections. Oil pump with vacuum gauge was connected to quartz tube

chamber, and the vacuum level of the system was measured before the gas flow. In addition, metal stands were used to support the weight of the flanges on the quartz tube.

3.2 Experimental procedure of conventional MgO/Fe_2O_3 catalyst system for BNNT production and optimization

3.2.1 Definition of an "experiment" in optimization scheme

In this experiment-oriented study an "experiment" has the following set of actions i) Preparation of MgO/Fe_2O_3 catalyst system for BNNT production. ii) Investigation of BNNT diameters by SEM analysis (iii) Initial RAMAN analysis for approximate surface coverage and BNNT film thickness.

3.2.2 Preparation of MgO/Fe_2O_3 catalyst system for BNNT production.

3.2.2.1 Materials

Necessary chemicals, which were used as precursors for BNNT production, are prepared before the experiments. Amorphous boron powder (>95 Sigma Aldrich), Fe_2O_3 (>99 Sigma Aldrich) and MgO (>99 Merck) were purchased. Silicon wafers which were used as a substrate were purchased from University Wafer Boston/USA. Ceramic and alumina crucibles and quartz tube vacuum chamber were procured. Inner quartz test tubes (one end closed) with 20 mm in diameter and 600 mm in length, which were used for trapping growth vapor, were purchased.

3.2.2.2 Method

3.2.2.2.1 Substrate coating

To make controllable experiments for optimization of BNNT growth by conventional catalyst system, Si-substrates were coated with MgO. However, direct coating of MgO onto Si substrate caused decrease of catalytic activity of the MgO due to the reaction with the substrate. For this reason, a thick Al_2O_3 buffer layer was coated onto Si substrates before MgO catalyst. This buffer layer prevents diffusion of the catalytic

material into the Si wafer and prevents reaction during coating. All coating processes were conducted at 10^{-6} torr vacuum level with "Torr E-beam and thermal evaporator" at SUNUM. To coat the substrate with active catalyst MgO, first substrates were coated with 30 nm thick Al_2O_3 buffer layer by e-beam method. Then, around 20 to 30 nm MgO active layer was coated by thermal evaporation. During MgO coating, first e-beam method was tried with as prepared MgO pellets, but the coating was not achieved. Then, MgO fine powder was used with the thermal evaporator, and successfully coated substrates were obtained. Film thickness was monitored with water-cooled quartz crystal thickness sensor integrated into the device.

3.2.2.2.2 TCVD synthesis of BNNT with conventional catalyst system

Growth vapor trap TCVD method was used for conventional system very similar to the method previously reported in the literature.[25] With this method, pure and high amount of BNNTs can grow on the substrate. In this method, classic horizontal furnace and the quartz reaction tube was coupled with quartz inner test tube. Therefore, growth vapor also called reactive vapor, could be trapped inside the inner tube. It is important to note that closed end of the test tube was placed against the gas flow. Therefore, created reactive vapor cannot escape from the substrate before nucleation vapor pressure was reached. Increased reactive gas vapor pressure enhanced the nucleation of the nanotube growth.

Schematics of experimental design was given in Figure 3.2

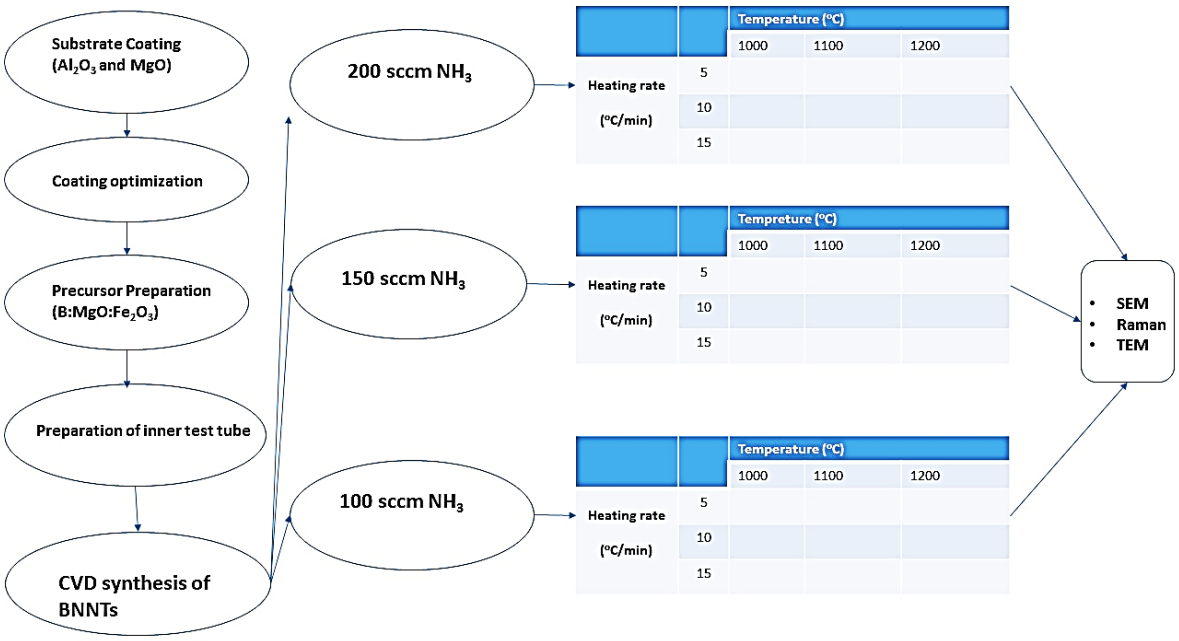

Figure 3. 2: Schematics of experimental design of TCVD synthesis of BNNT with classic catalyst system

Experimental steps for conventional MgO/Fe_2O_3 catalyst system for BNNT production and optimization was summarized in below.

- Amorphous boron powder and conventional catalytic materials (MgO and Fe_2O_3) with different molar ratios (B: MgO: Fe2O3 mole ratio, 2:1:1 and 4:1:1, respectively) were mixed.
- For optimization experiments only 4:1.1 ratio was applied. Since with this ratio, Boron to oxygen mole ratio in the precursor powder is equal to the 1:1. By this way, exact stoichiometry was achieved to create a B_2O_2 intermediate compound.
- Mixed precursor powders around 200 mg were ground and placed in the crucible.
- Top of the crucible was covered with substrates already coated with active catalyst. In addition to that, coated faces of the substrates were not placed

looking directly to the precursor powders, i.e. the coated surface was looking upwards.

- Then, crucible and the substrates were placed inside the quartz test tube near to the closed end side.
- The prepared test tube was then loaded into the furnace inside the quartz tube vacuum chamber. A crucible inside the test tube was carefully arranged so that it was in the stable heating zone of the horizontal furnace.
- Then, the system was sealed and vacuumed around 15 minutes by controlling the vacuum gauge. Then, argon flow was introduced to the system for 15 minutes to get rid of remaining oxygen and vacuumed again.
- After the system was thoroughly vacuumed, the system was heated with the NH_3 flow.
- Three different NH_3 flows were used. (100, 150 and 200 sccm)
- Three different maximum temperatures were chosen (1000^{o}C, 1100 ^{o}C and 1200 ^{o}C).
- To understand the effect of the heating rate at low temperatures, three different heating rates were used (5 ^{o}C/min, 10 ^{o}C/min, and 15 ^{o}C/min).
- Resulting products were characterized by SEM, TEM, EELS, and Raman spectroscopy techniques.

3.2.3 Investigation of BNNT diameters by SEM analysis

The primary focus was on the effects of process parameters on the nanotube diameter and its statistics over each BNNT grown on Si substrate. Several images from each substrate surface were analyzed under SEM (LEO 1530VP). SEM images with same magnification (x50k) are then analyzed by an image processing software (Image-J).

Diameter measurements are performed from 100 different nanotubes or nanotube like formations observed on the substrate surface. The average diameter and standard deviation values were calculated for each set of image.

3.2.4 RAMAN Spectroscopy for Surface Coverage and Film Thickness Measurements

Raman analysis of as synthesis BNNTs on the substrate was conducted from 20 different points that distributed over a substrate to find out coverage (which corresponds to yield). Experimentation details are provided in section 4.4.2. In addition to that 20 points will be added up together to increase the signal to noise ratio. Then BNNT film thickness (corresponding to aspect ratio) were determined from thickness fringes by using Fabry-Perot resonance.

3.2.5 Planning and analysis of Experiments: Response surface methodology

Parametric investigation of the effect of CVD process parameters on the grown BN nanostructures requires a set of experiments described in 3.2.2. The planning and analysis of these experiments were performed within the context of Response Surface Methodology. Response surfaces are used to approximate numerical or physical data by an expression that is usually low order polynomial. Three critical steps of the methodology as noted in Yördem et al. are as follows. [117]

3.2.5.1 Design of Experiments

Parameter or factor settings at which the experiments were conducted were pre-set. The selection represents three so-called “factors” which are

i) Reaction temperature (f1): Reaction maximum temperatures were adjusted according to the general catalytic reaction of BN formation which is shown in chapter 4.2. Temperatures were chosen according to the boiling point of metallic magnesium. Because after the reaction between MgO and B to from B_2O_2

intermediate phase, metallic magnesium act as a catalyst which evaporates and condenses on the substrate surface to form catalytic droplets. For this reason, one temperature below magnesium melting point (1000 ^{o}C), one temperature at Mg melting point (1100 ^{o}C) and one temperature over Mg melting point (1200 ^{o}C) were chosen.

ii) Heating rate (f2): Heating rate was defined as the time required to reach maximum reaction temperatures. This parameter was chosen to determine the effect of reaction time and have a better understanding of the kinetics of BNNT formation. Since, higher heating rates will cause spontaneous nucleation and leaves less time for nanotube growth, which may affect the morphologies of the resulting nanotubes. Three heating rates were assigned for BNNT growth; high (15 ^{o}C/min), medium (10 ^{o}C/min) and low (5 ^{o}C/min)

iii) Reactive gas flow rate (f3): Reactive gas (NH_3) flow rate is another factor that affects the growth of the BNNTs. Since, GVT approach is based on the increase in the vapor pressure of the growth species in the inner tube, higher NH_3 flow rate is expected to increase the diffusion of the NH_3 inside the inner tube, which in turn affect vapor trapping and nucleation of BNNTs. Therefore, three NH_3 flow rates were chosen: 200 sccm, 150 sccm, and 100 sccm.

The experimentation scheme applied was a 3-level full factorial design. Each factor is examined at three different levels and represented in the coded domain as a minimum (-1), mean (0) and maximum (+1). Experimentation scheme and factor levels resulted in 27 total experiment points defining the design space (figure 3.3).

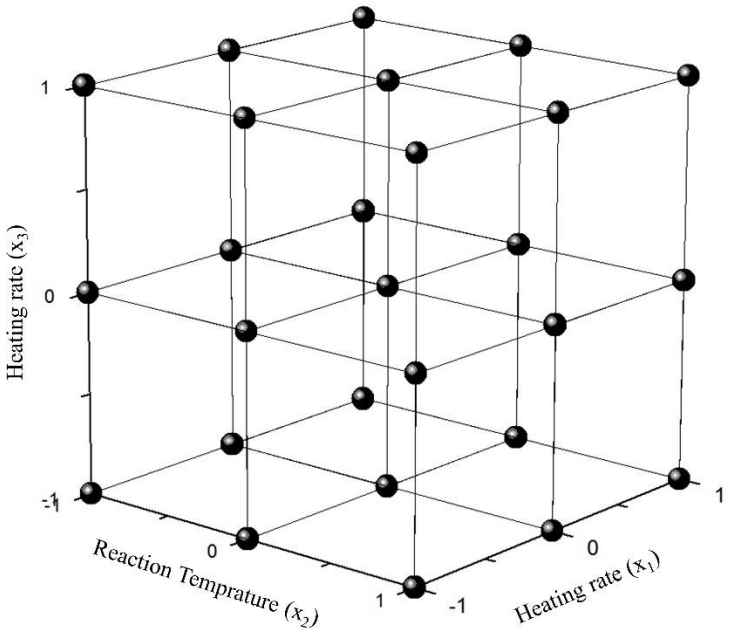

Figure 3. 3: Experimental matrix

The experimental results were directly used in the creation of "**responses**" such as

i) BNNT surface coverage (R1)

ii) BNNT film thickness (R2)

iii) BNNT aspect ratio (R3) (average BNNT diameter (nm)/ BN layer thickness (um)

*See Table 4.1.`

3.2.5.2 Regression Analysis

Surrogate mathematical models representing the responses in terms of process factors by corresponding b approximates are determined by least square fitting of experimental data. Depending on the degree of mathematical model (namely, polynomial) response (Y) is represented as;

$Y = \mathbf{b_0} + \mathbf{b_1} f_1^2 + \mathbf{b_2} f_2^2 + \mathbf{b_3} f_3^2 + \mathbf{b_4} f_1 f_2 + \mathbf{b_5} f_1 f_3 + \mathbf{b_6} f_2 f_3 + \mathbf{b_7} f_1 + \mathbf{b_8} f_2 + \mathbf{b_9} f_3$ (Quadratic Model)

$Y = \mathbf{b_0} + \mathbf{b_7} f_1 + \mathbf{b_8} f_2 + \mathbf{b_9} f_3$ (first order Model)

The fundamentals for least squares fitting procedure can be found in a number of sources.[118] The regression analysis was performed using a statistical software Design Expert 8.0. These surrogate models can be used to show the individual effects (by b1, b2, b3 approximates) as well as combined effects (by b4, b5, b6 approximates) of process factors to the investigated response.

3.3 Experimental procedure of new $KFeO_2$ catalyst system for BNNT synthesis at low temperatures

3.3.1 Potassium ferrite ($KFeO_2$) synthesis

$KFeO_2$ was synthesized via organic precursor method. To obtain single phase $KFeO_2$, a specific amount of cation salts and an excess amount of organic carrier were used. $Fe(NO_3)_3.9H_2O$ (>99 Alfa aesar) and KNO_3 was used as cation salts and citric acid (CA) (Alfa aesar) as carrier material. The desired amount of each cation salt and an excess amount of CA were dissolved in distilled water separately then mixed. To homogenize the resulting mixture, the solution was stirred at 200 rpm for 30 minutes. Then, the homogenized solution was heated on the magnetic stirrer to the complete dryness. The resulting powder was collected and calcined at 700 ^oC for 2 hours. After

two hours sample was vacuum quenched immediately in the desiccator without allowing to cool slowly in the oven. Final olive green $KFeO_2$ powder was collected and stored in the glovebox.

3.3.2 BNNT production

BNNTs production was carried out by growth vapor trap TCVD method. Schematic of the setup can be seen in Figure 3.4. In this setup, close end inner quartz tube (2 cm in diameter and 50 cm in length) was placed inside the horizontal furnace against the gas flow to avoid trap growth vapor carried away from the substrate. Therefore, reactive growth vapor which was formed during the reaction between precursors reached enough vapor pressure for nucleation on the substrate.

Experimental steps were summarized below.

- The inner tube was prepared inside the glovebox to avoid $KFeO_2$ decomposition with moisture.
- Amorphous boron powder and $KFeO_2$ (2:1 mole ratio) were mixed in a mortar and placed inside the ceramic reaction boat (only half of it filled with powder).
- The top of the reaction boat was covered with the ceramic substrate, which was prepared by cutting the bottom of another empty reaction boat.
- Then, covered reaction boat was placed near the closed end side of the inner quartz tube and sealed with silicone rubber stopper.
- After that, inner tube was removed from the glovebox and placed inside the horizontal furnace.
- Before the experiment was run, argon was introduced to the system to remove oxygen, and inner tube was opened under argon.
- Then, the system was heated under 200 ml/min NH_3 flow to 800 ^oC in one hour and kept for 2 hours.

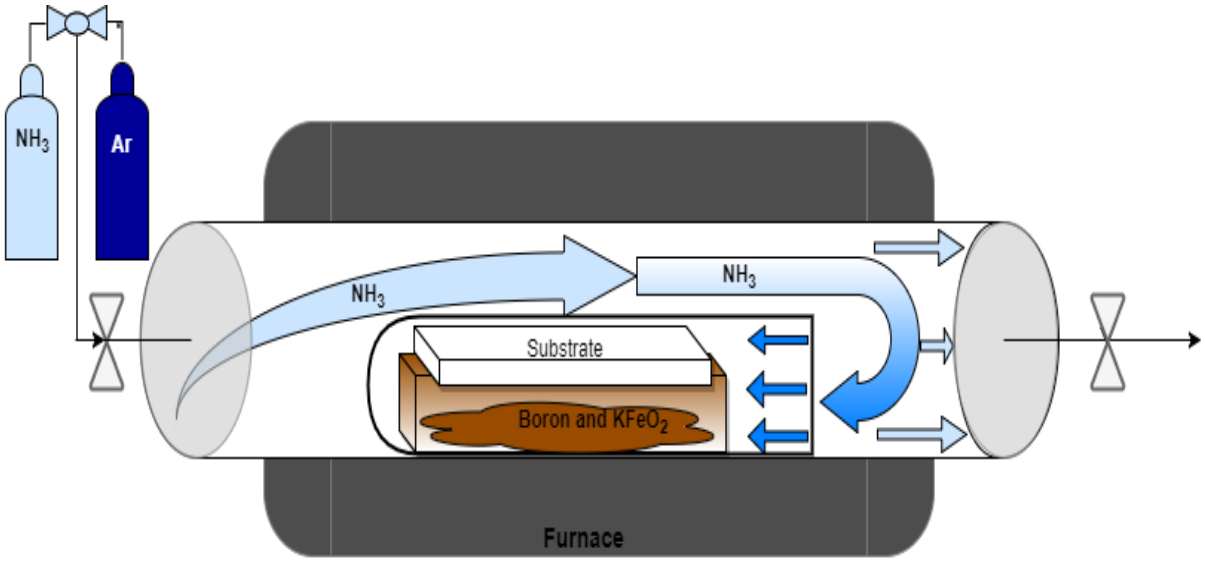

Figure 3. 4: Vapor trap TCVD system setup

3.4 Experimental procedure of other alkali metal ferrite catalyst system for BNNT synthesis

3.4.1 Synthesis of alkali metal ferrites ($CsFeO_2$, $NaFeO_2$ and $LiFeO_2$)

Other Alkali metal ferrites (Cs, Na, and Li) were synthesized according to the organic precursor method, same way as $KFeO_2$. Nitride salt of alkali metals ($CsNO_3$ (>99 Alfa aesar), $NaNO_3$ (>99 Alfa aesar), $LiNO_3$ (>99 Alfa aesar)) and $Fe(NO_3)_3.9H_2O$ (>99 Alfa aesar) were chosen due to their high solubility in water. CA was used as an organic carrier. For synthesis of alkali metal ferrites, alkali metal to iron mole ratio should be one to one. Therefore the exact amount of desired alkali metal salt and iron salt were dissolved in distilled water separately (Table 3.1). Then, an excess amount of CA solution was prepared and cation solutions were added on to it. After 30 minutes of homogenization at 200 rpm with the shaker, the solution was evaporated around 200 ^oC on a hot plate to obtain dry powder mixture. Afterwards, powders were calcined at 700^oC for 2 hours in a box furnace and vacuum quenched in a desiccator. Resulting alkali metal ferrites were stored in the glovebox for further usage.

Table 3. 1: Amount of precursor for alkali metal ferrite synthesis

$Fe(NO_3)_3.9H_2O$ (g)	**$CsNO_3$ (g)**	**Citric Acid**	**$CsFeO_2$ (g)**
5.48	2.64	Excess	3
$Fe(NO_3)_3.9H_2O$ (g)	**KNO_3 (g)**	**Citric Acid**	**$KFeO_2$ (g)**
9.54	2.38	Excess	3
$Fe(NO_3)_3.9H_2O$ (g)	**$NaNO_3$ (g)**	**Citric Acid**	**$NaFeO_2$ (g)**
10.93	2.30	Excess	3
$Fe(NO_3)_3.9H_2O$ (g)	**$LiNO_3$ (g)**	**Citric Acid**	**$LiFeO_2$ (g)**
12.78	2.18	Excess	3

3.4.2 Alkali metal ferrites catalyst for BNNT production

The Same production method in 3.3.2 was used for BNNT synthesis by other alkali metal ferrites. For precursor powder, boron powder/alkali metal ratio was determined according to the exact stoichiometry for B_2O_2 intermediate phase formation. Therefore, boron to oxygen in the desired alkali metal ferrite mole ratio was arranged 1 to 1. For each BNNT production, resulting sample on the crucible walls were characterized by Raman spectroscopy and SEM.

3.5 Characterization techniques

3.5.1 XRD for as synthesized alkali metal ferrites

For phase analysis and crystal structure determination, X-Ray diffractometer was used at room temperature (BRUKER D8 ADVANCE X-RAY DIFFRACTOMETER, Karlsruhe, Germany), Koç University (KUYTAM). CuKα radiation generated by 40kV of voltage and 40 mA of current were employed. Measurement parameters were chosen from (2θ) 15° to 70° with a step size of 0.02° and a step time of 0.2 seconds.

3.5.2 UV-Vis spectroscopy

Optical absorption edges of BNNTs were calculated using a Shimadzu 3150 UV–Vis Spectrophotometer (Shimadzu Corporation, Kyoto, Japan).

3.5.3 FT-IR spectroscopy

The FTIR spectra of the alkali metal ferrites were recorded over the range of 4000-550 cm^{-1} on a Thermo Scientific Nicolet iS10 spectrometer with ATR apparatus. The total numbers of scans were 32 with a spectral resolution of 4 cm^{-1}.

3.5.4 Raman Spectroscopy

Raman spectroscopy was performed using a Renishaw in Via Reflex Raman Microscope and Spectrometer at room temperature with a 50x objective. Raman spectral analyses using visible excitation at 532 nm were done with a Nd-YAG laser power of 10 mW with data acquisition time of 10 s. The spectral range was selected as 100 cm^{-1} and 3000 cm^{-1}. Wire 3.1 software was used to fit adjusted peaks. For all the spectra, a linear baseline correction was applied.

3.5.5 SEM and EDX Analysis

Microstructural imaging and elemental analysis by energy dispersive X-Ray spectroscopy (EDXS, Röntec, Berlin, Germany) were conducted with the help of a scanning electron microscope (FEG-SEM Leo Supra 35, Oberkochen, Germany).

ImageJ program was used to calculate average diameter of as synthesized BNNTs.

3.5.6 TEM analysis

Microstructural analysis was carried out in a probe Cs-corrected JEOL ARM200 ColdFEG (JEOL, Tokyo, Japan). Both parallel illumination (High Resolution-HRTEM) and probe modes (Scanning-STEM) were employed. Elemental analysis of the nanotubes were conducted via an electron energy loss spectroscopy (EELS-Gatan GIF

Quantum ER spectrometer). Chemistry of the tips of nanotubes were determined with Energy Dispersive X-ray Spectroscopy (EDS, JEOL Centurio Dry SD100GV SDD detector). Both EDS and EELS were employed in STEM mode with a probe size of 6C, using a 40μm condenser lens aperture. For EELS analysis, spectrometer aperture was left at 5mm and camera length was used as 6cm. The dispersion was set at 0.25 eV in order to observe both B-K and N-K edges that are positioned at 188 and 401 eV, respectively. Background removal was performed by powerlaw.

CHAPTER 4

4 CONVENTIONAL MgO/Fe_2O_3 CATALYST SYSTEM for BNNT PRODUCTION and OPTIMIZATION

4.1 Summary

Effects of CVD process parameters on the growth quality and aspect ratio of synthesized BNNTs with conventional catalyst were experimentally investigated. Response surface methodology (RSM) was utilized to design the experiments at the settings of reaction temperature (f_1), heating rate (f_2) and reactive gas flow rate (f_3). Three main responses such as substrate coverage, film thickness, and BNNT aspect ratio were considered. The investigations were carried out in three variable process domains of several f_1, f_2 and f_3 are varied at a fixed initial material amount and waiting time at T_R. The mean aspect ratio and substrate surface coverage were modeled by linear/polynomial response surfaces as functions of above mentioned process variables. Characterization efforts for determining the response values at experiment points included SEM analysis (followed by image processing) for nanotube diameter and RAMAN analysis for grown BNNT thickness measurements and substrate surface coverage.

4.2 BNNT production with conventional catalyst system

In this chapter, BNNT synthesis was conducted by GVT TCVD approach (see section 2.3.2). Conventional catalyst system (MgO and Fe_2O_3) is the most used catalyst for BNNT production with CVD. However, for every different system and experimental conditions, BNNT morphology was changing even when the same catalyst was used, since small perturbations on the system such as precursor particle size, efficient vapor trap etc. affect the final product. As explained before, precursor powders were placed inside the one end closed inner quartz tube, which allows trapping reactive growth

vapor those formed at high temperatures. Moreover, the closed end side of the inner tube was placed against the gas flow, by this way direct gas flow was avoided and reactive vapor did not leave the system before it reached the critical vapor pressure for nucleation.

Vapor liquid solid mechanism was offered for growth mechanism of BNNTs. While the temperature was rising, boron powder was oxidized to B_2O_2 reactive phase by reaction with MgO and Fe_2O_3. Then, reduced metals start to evaporate and condense on the substrate or walls of the combustion boat when its vapor pressure high enough. Then, B_2O_2 vapor reacts with NH_3 to form BN and as formed BN species start to dissolve in partially condensed catalyst droplets. After supersaturation, BN starts to precipitate and nanotube formation occurs. Depending on the interaction between the substrate and the partially condensed catalytic droplets, base growth (strong interaction) or tip growth (weak interaction) is favorable. For our system, MgO was coated to the substrate surface as a catalyst. Moreover, temperatures used in this study is just enough to form Mg vapor, which condenses on the substrate, it is proposed that MgO be the effective catalyst and B_2O_2 source together with Fe_2O_3. In the literature, MgO is determined to be a very efficient B_2O_2 creator compared to the other catalysts, but it has slower activity [23, 110, 119]. Addition of FeO increases the catalytic activity and reduce the formation of $Mg_2B_2O_5$, which deactivate the catalyst irreversibly [120]. In this study, Fe_2O_3 is replaced with FeO as an iron and oxygen source for B_2O_2 reactive phase formation. Chemical reactions, which were believed to occur during BNNT synthesis, were shown as below;

$$2MgO(s) + 2B(s) \rightarrow B_2O_2(g) + 2Mg(g)$$

$$Fe_2O_3(s) + 3B(s) \rightarrow B_2O_2(g) + 2Fe\ (s)$$

$$B_2O_2(g) + 2NH_3(g) \rightarrow 2BN(nanotube) + 2H_20(g) + H_2(g)$$

As grown BNNT field on the substrate was shown in low magnification SEM micrograph (Figure 4.1). Growth parameters are 1200 ^{o}C with 10 ^{o}C/min at 200 sccm.

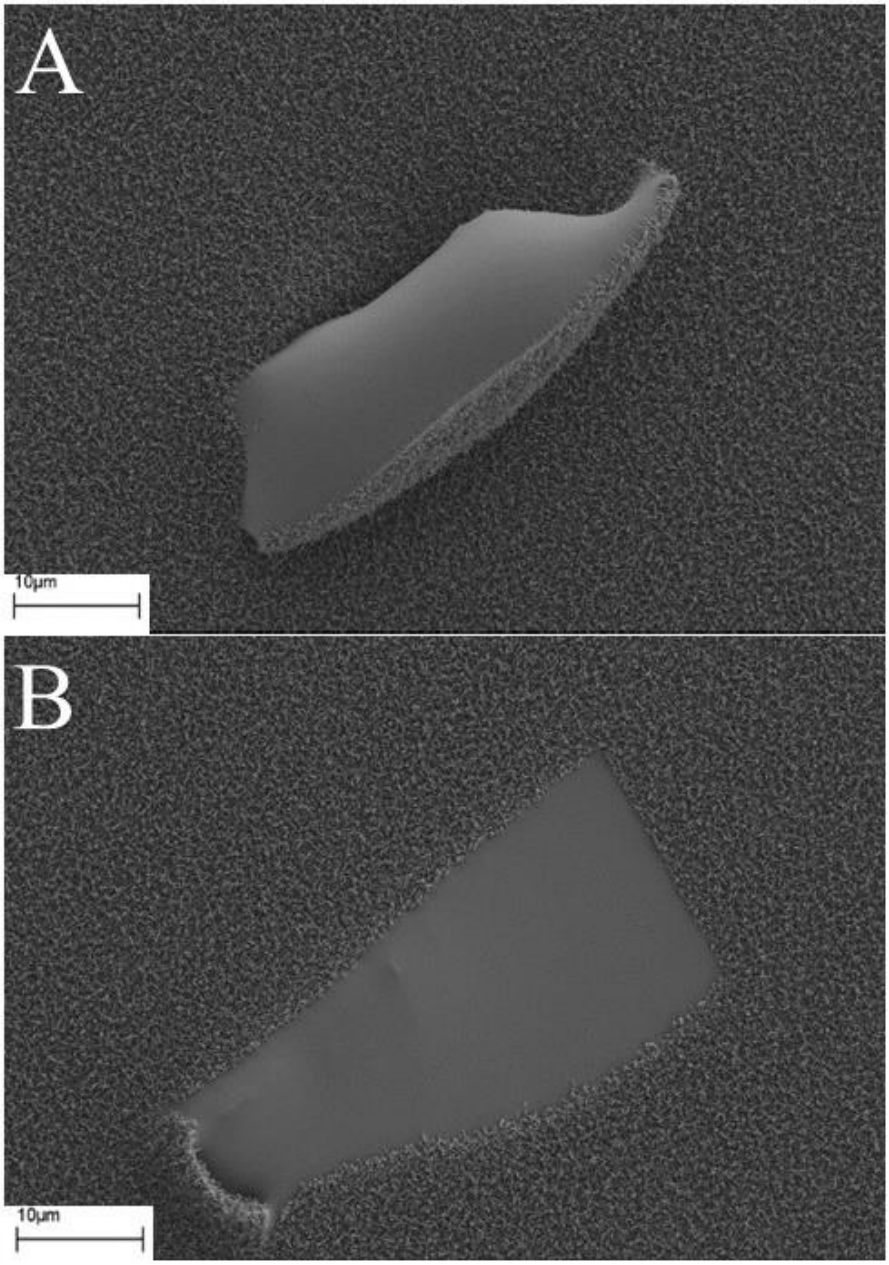

Figure 4. 1: BNNT field growth on Si substrate

4.3 Preliminary Results for BNNT production with Conventional Catalyst System

Before conducting systematic experiments for optimization studies, catalyst/boron ratio and BNNT growth time were determined by preliminary experiments. Predetermined parameters were applied in all experiments for optimization.

- **BNNT growth time**
- **Precursor Ratios**

4.3.1 BNNT growth time

The time required for BNNT growth at maximum temperature was determined. Two sets of experiment were conducted for 1hour reaction time at maximum temperature and 30 minutes reaction time at maximum temperature. Results show that increasing reaction time lead to longer nanotubes (figure 4.2A). However, thickness calculations were not practical for longer nanotubes, for this reason, 30 minutes reaction time (length around 2 μm) were chosen (Figure 4.2B). Since all experiments were conducted with the same parameters, aspect ratio calculations just compared with each other. Therefore, short BNNT growth time does not effect overall observations.

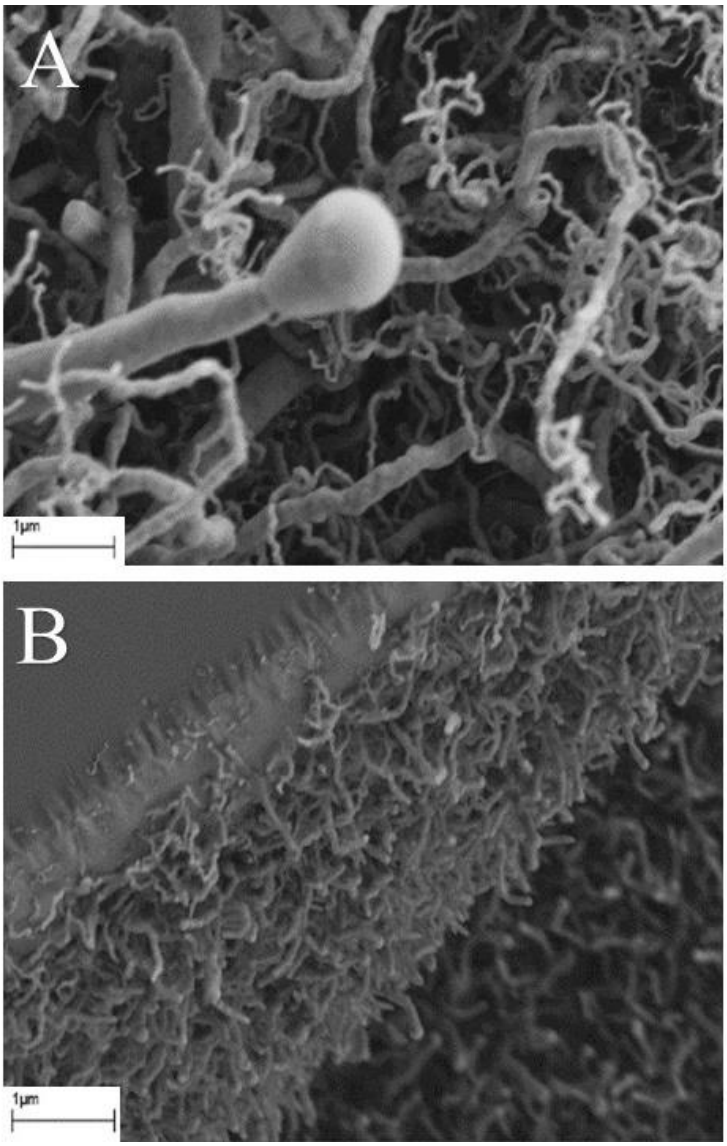

Figure 4. 2: A) 1 hour reaction time B) 30 minutes reaction time

4.3.2 Precursor Ratios

BNNT production with TCVD with the B/MgO/Fe_2O_3 precursors requires forming B_2O_2 reactive phase. Boron powder and catalytic materials with two different mole ratios (4:1:1 and 2:1:1) were prepared for required stoichiometry to form B_2O_2 phase from B and oxygen. To determine the difference between the two stoichiometric ratios, experiments with same parameters were conducted at 1100 ^oC with 10 ^oC/min under 200 sccm NH_3 flow. SEM micrographs of resulting samples with different precursor ratios were shown in figure 4.3

Precursor ratio 4:1:1 (B: MgO: Fe_2O_3) gives a better distribution of smaller diameter tubes compared to 2:1:1. Probably lower metal content of 4:1:1 ratio results in the smaller catalytic droplet and more controllable B_2O_2 formation which possibly prevents spontaneous nucleation of BN. [25] However, 2:1:1 cause different morphologies, fiber-like structures with very large diameters (Figure 4.3B).

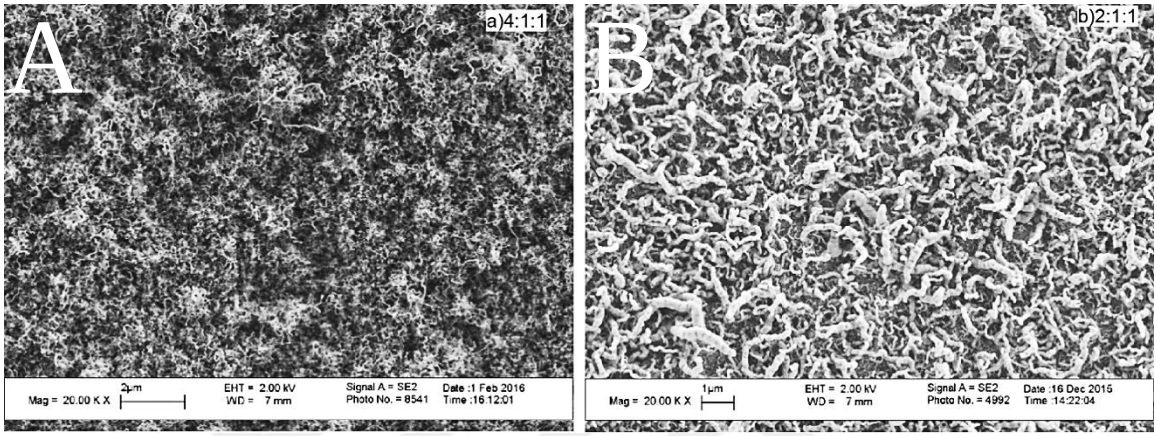

Figure 4. 3: BNNTs with different precursor ratios a) 4:1:1 b) 2:1:1

4.3.3 Characterization of Preliminary BNNT production

4.3.3.1 UV-Vis Spectroscopy Analysis and Bandgap

BNNTs are insulated materials with a wide bandgap. Moreover, their bandgap is independent of the tube diameter and morphology. BNNTs synthesized with our setup have curvy entangled morphologies with diameters changing from 30 nm to 100 nm. In order to compare them with the other BNNTs with very crystalline straight tubes which give band gap between 5.5 and 6 eV, one set of experiments were used to the determined band gap of as synthesized BNNTs by using UV-VIS adsorption spectroscopy. Substrates were sonicated in ethanol, and these solutions were used in the UV-Vis spectroscopy (Figure 4.4). The calculated band gap of BNNTs which were synthesized at 200 sccm NH_3 flow with 10 ^oC/min heating rate and different temperatures 1000 ^oC, 1100 ^oC and 1200 ^oC, were almost the same (5.8 eV). Results

also demonstrate that measured values for curly entangled BNNTs are in very well agreement with the literature values for long straight highly crystalline BNNTs.

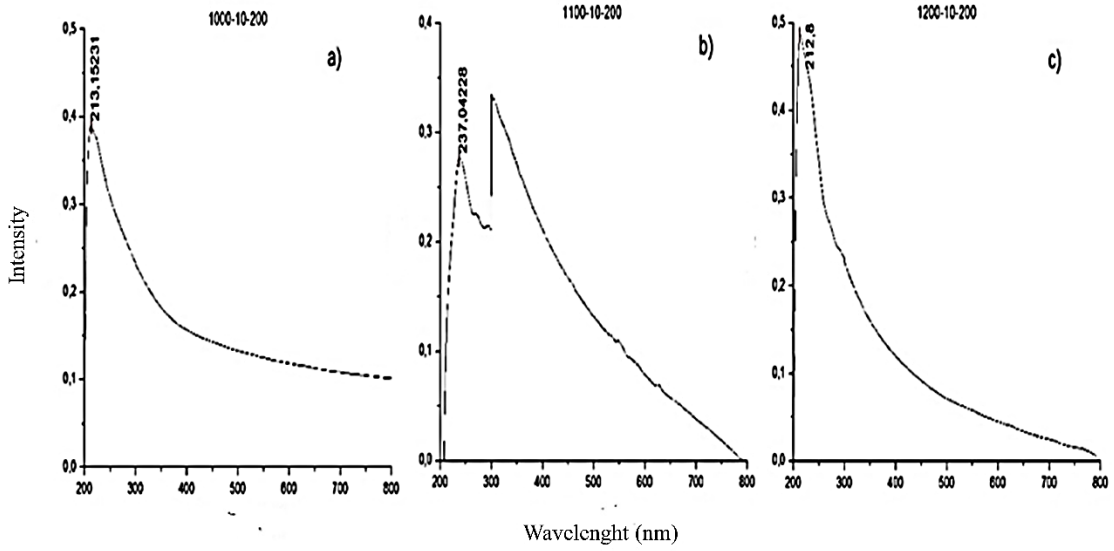

Figure 4. 4: UV absorption spectrum of BNNTs prepared at different temperatures.

4.3.3.2 TEM and EELS analysis

TEM analysis was conducted to investigate atomic structure of the as synthesized BNNTs at different temperatures. Moreover, EELS analysis were conducted in order to determine the chemical composition of the BNNTs, since EELS is one of the very few techniques that can identify light elements like B and N. Two methods were used to prepare TEM samples. The first method was scratching off the substrate then ground in a mortar with ethanol. However, resulting nanotubes were not dispersed in conditions they agglomerated (Figure 4.5A). To overcome the agglomeration problem, sample preparation was handled with ultrasonicator. Substrates sonicated in ethanol for 90 minutes resulted in good dispersion, and well prepared TEM samples (figure 4.5B)

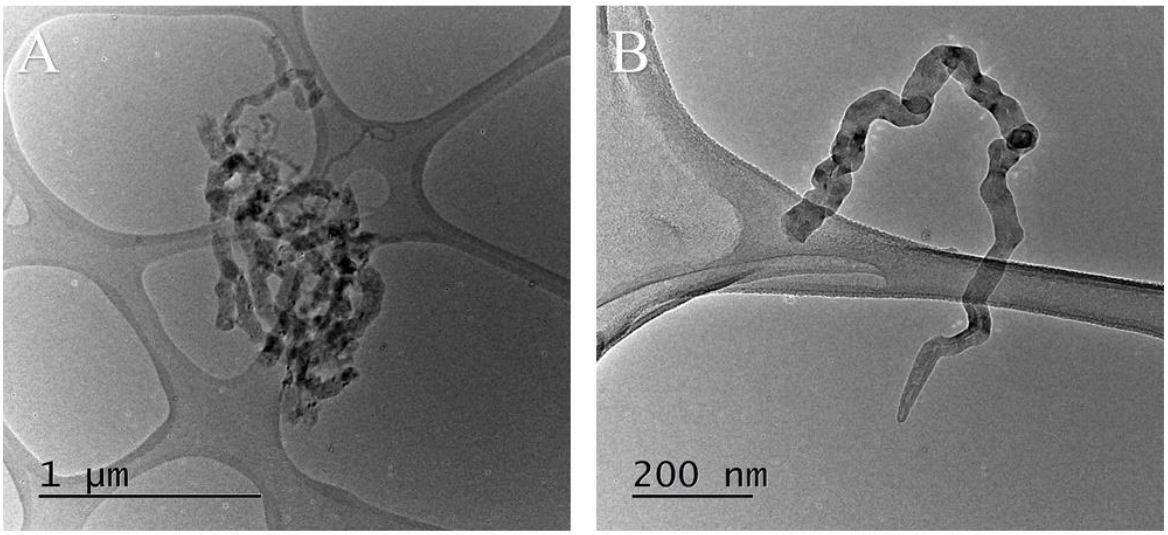

Figure 4. 5: A) TEM sample prepared by grinding (agglomeration) B) TEM sample prepared by Sonication (Growth conditions: 1100 ^{o}C, 10 ^{o}C/min, and 200 sccm NH_3)

The primary outcomes of TEM analysis can be summarized as following:

HRTEM: BNNTs were hollow, and had multiwalled structure. Interplanar spacing was determined as 0.323 nm, which is in good agreement with the literature (Figures 4.6B). Morphology of the BNNTs at 1100 ^{o}C and 1200 ^{o}C showed similar structures. Although diameters of the tubes are not uniform along the tube due to the curvatures, the diameters of the BNNTs are ranging between 30 nm to 80 nm, (figure 4.6C-D). There is also some observable amorphous coating on the sidewalls (Figure 4.6A). Most of the nanotubes are grown in entangled curly fashion and showed cup type bamboo like hollow morphologies [121]. Some catalytic particles were trapped in the structure, which probably results from the partial breaking of core catalytic droplet (Figure 4.6C). Curved nanotubes have close tips (Figure 4.6E), some of them were incorporated with metal particles and some of them without (Figure 4.6F) which suggest the mixed (base and tip) growth mode of the BNNTs. Results seem reasonable since Si substrates were coated with MgO, which already had a strong interaction with the substrate due to Al_2O_3 diffusion layer, leads to the base growth mode and additional Mg particles also evaporated from the precursor powder to form droplets, which has lesser interaction

with the substrate favors the tip growth mode. There are several other works, which reported same morphology with this work [27, 116].

Typical EELS spectrum of the sample grown at 1100 ^{o}C show two distinct structures at 188 eV and 401 eV, which belong to the B and N respectively (figure 4.7A-B). The first sharp peak in the Energy Loss Near Edge Structure (ELNES) of both B-K and N-K edges are due to transitions to π^* which is characteristic for the sp^2 bonding of h-BN.

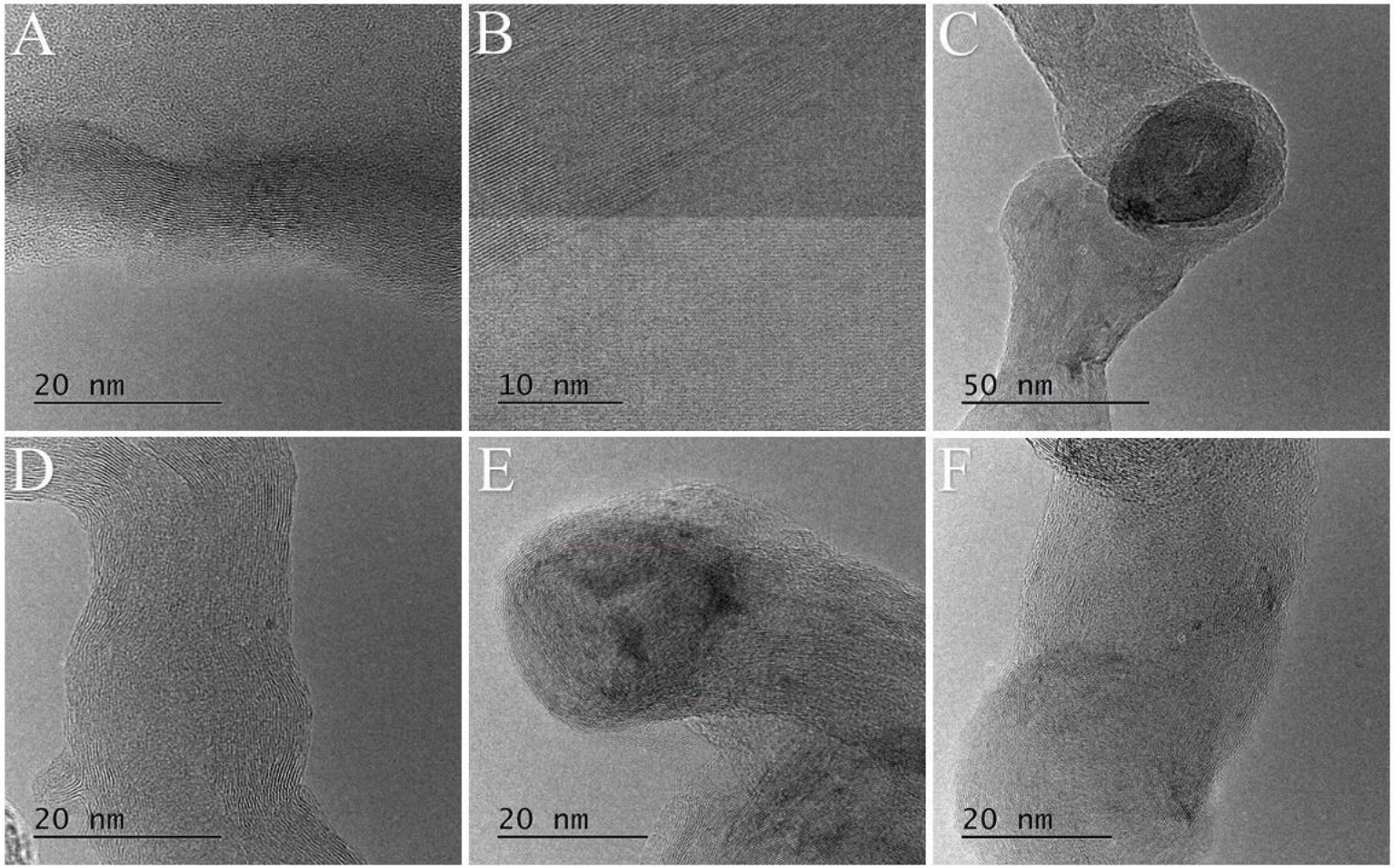

Figure 4. 6: 1100 ºC A) Amorphous coating on the walls B) Lattice spacing between walls C) Catalytic particle in the joint. 1200 ºC D) Curly structure (bending) E) Tips morphology F) Irregular cup type hollow bamboo like structure

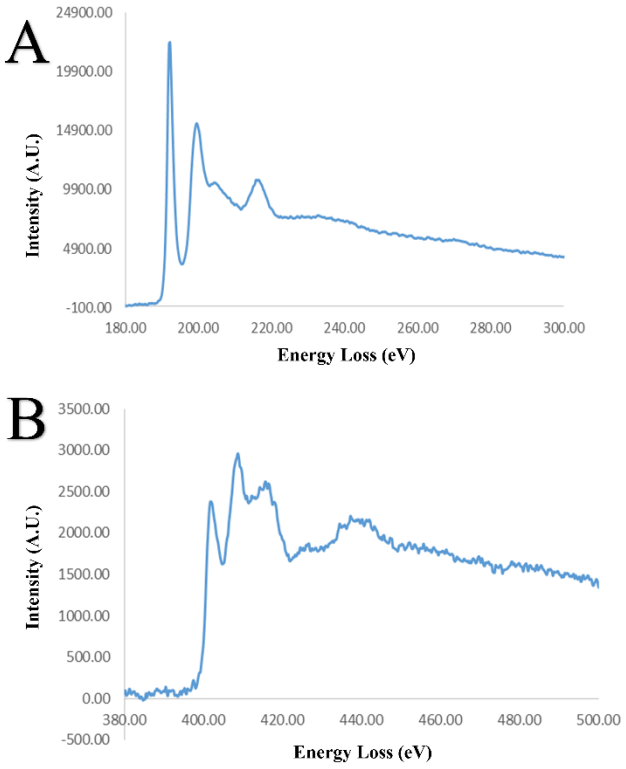

Figure 4. 7: A) B-K B) N-K Ionization edges collected from the nanotubes,

4.4 Results of BNNT Production with Conventional Catalyst System for Every Optimization Points

After preliminary experiments, parameters such as reaction time and precursor ratios were fixed. In addition, UV adsorption and TEM analysis proved that BN structures could be synthesized through the conducted procedure. Experimental results at all optimization points were presented in this chapter. Every set of experiments were separated according to the NH_3 flow rate.

4.4.1 SEM Analysis

Morphology of the BNNTs was investigated by SEM directly from substrates covered with BNNTs. Figures 4.8, 4.9, 4.10 correspond to SEM micrographs for BNNT grown on Si substrate surfaces at constant levels of gas flow rate. Reaction temperatures -1, 0,

1 correspond to 1000 ^{o}C, 1100 ^{o}C and 1200 ^{o}C respectively. Heating rate -1, 0, 1 correspond 5 ^{o}C/min, 10 ^{o}C/min and 15 ^{o}C/min respectively.

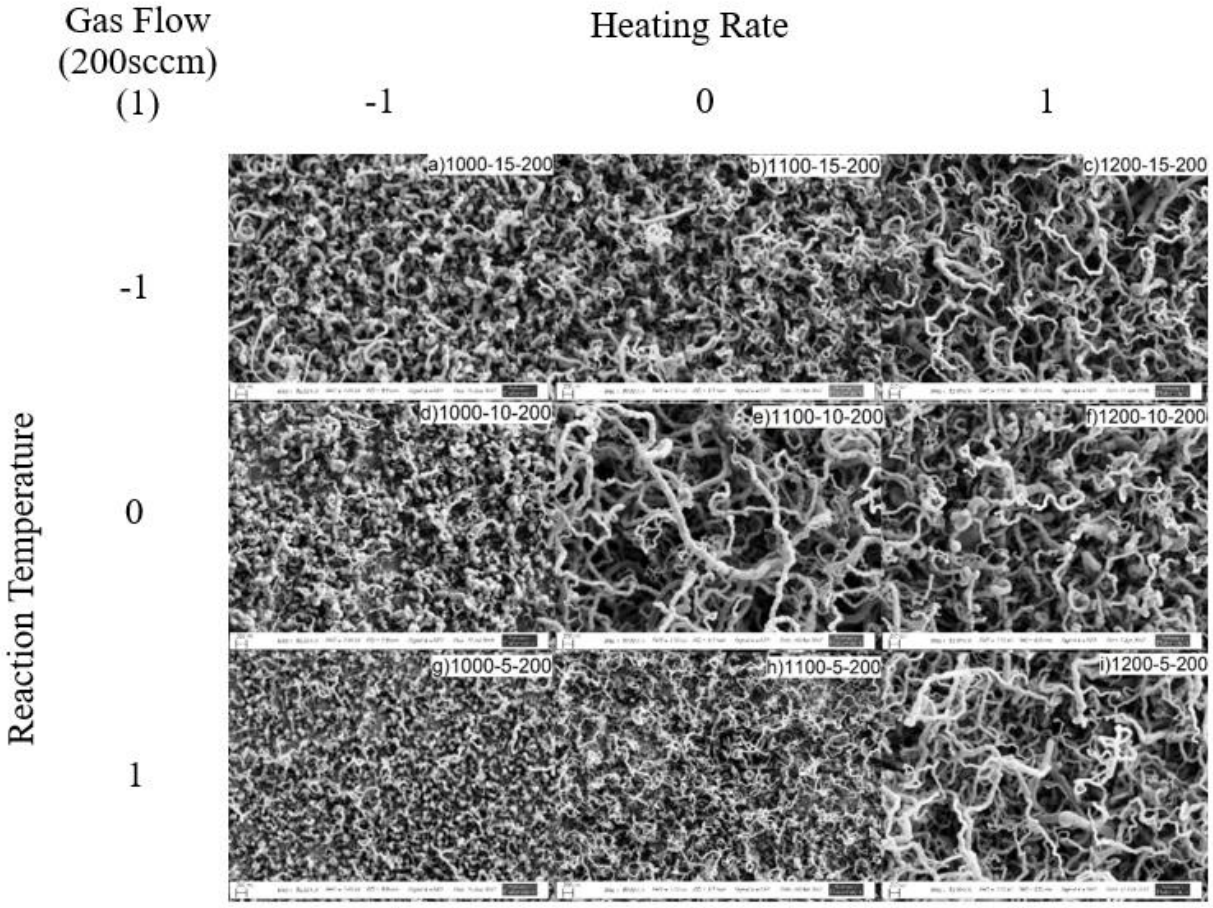

Figure 4. 8: SEM micrographs of as synthesized samples at 200 sccm NH_3 flow

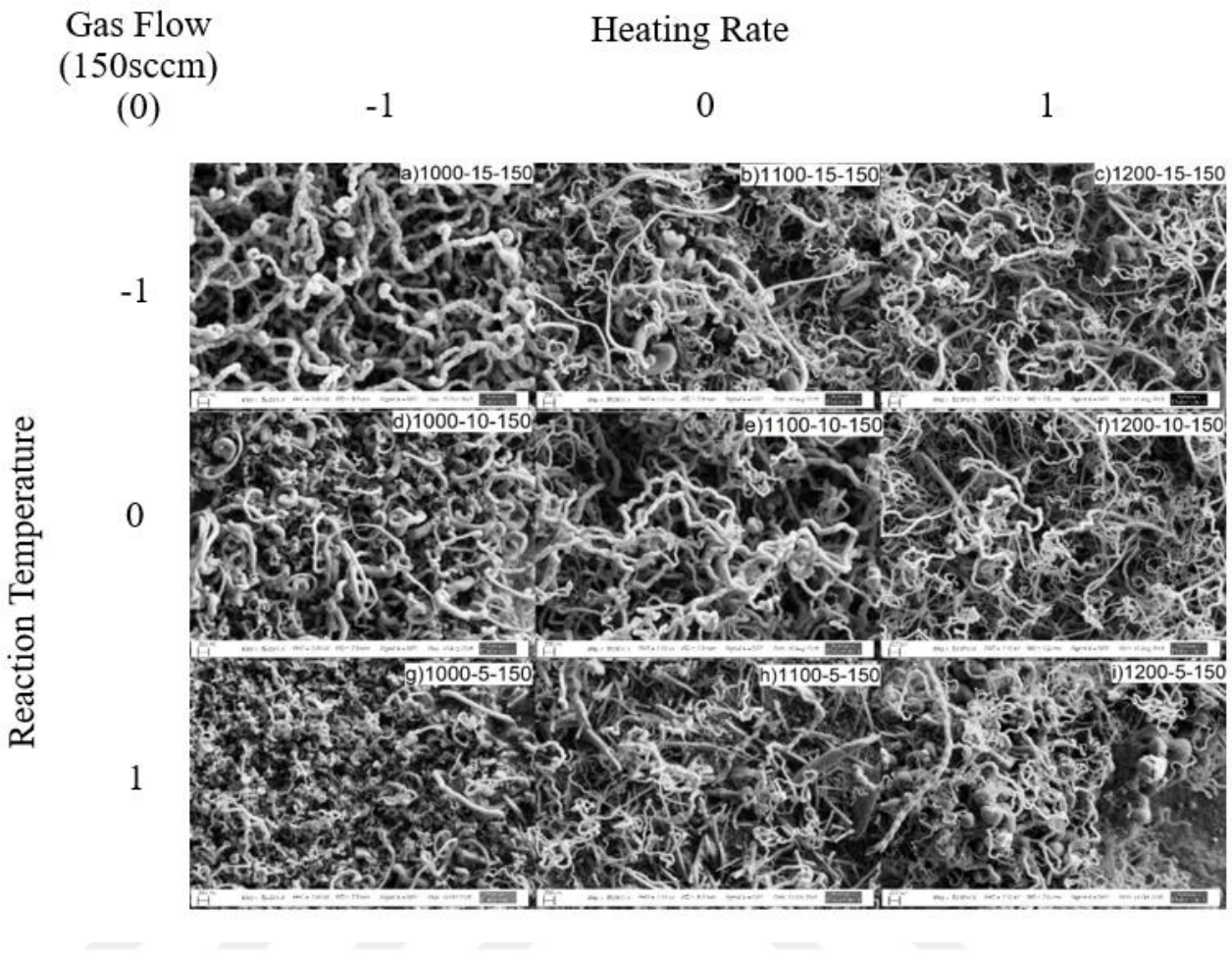

Figure 4. 9: SEM micrographs of as synthesized samples at 150 sccm NH3 flow

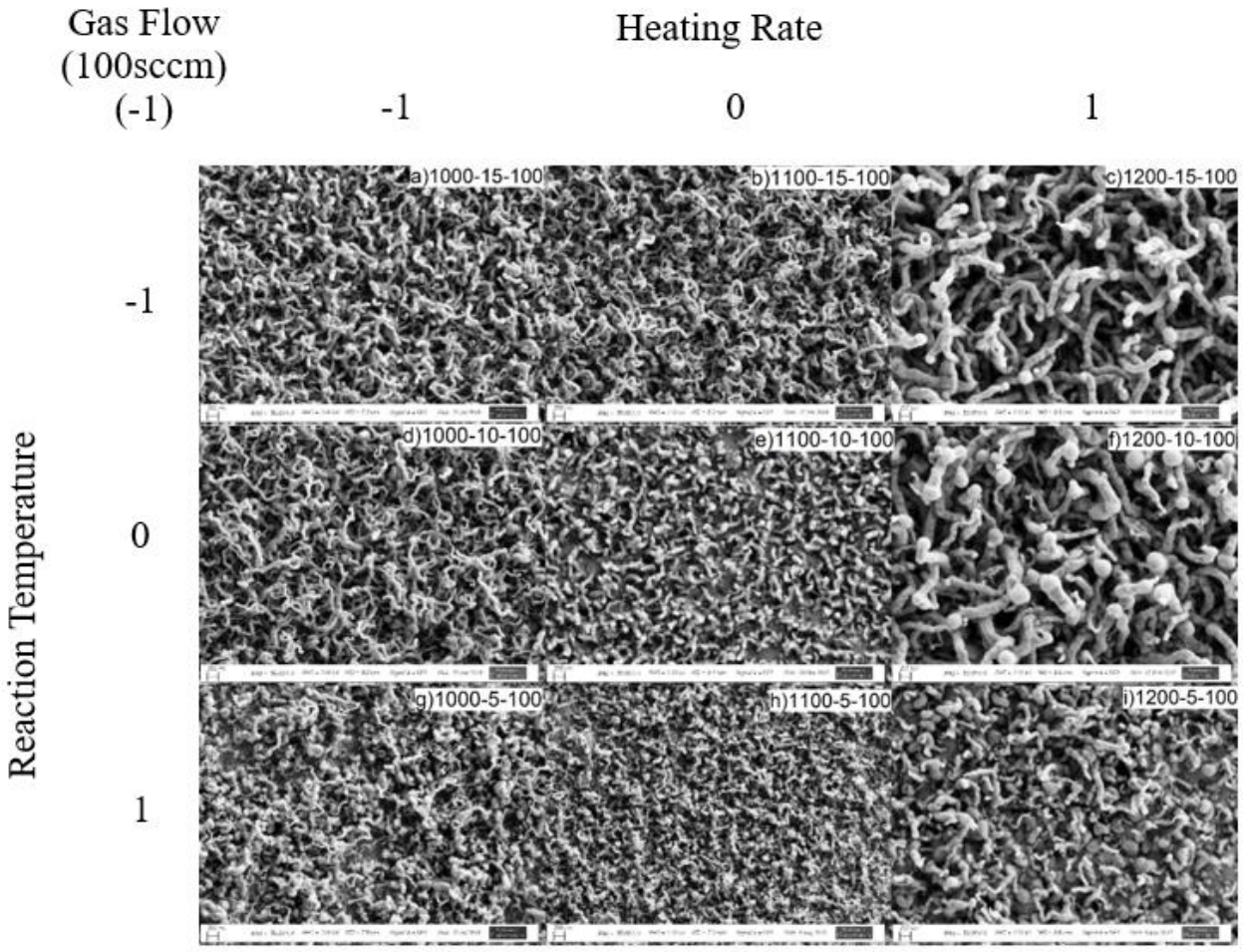

Figure 4. 10: SEM micrographs of as synthesized samples at 100 sccm NH_3 flow

Observations

When SEM micrographs were investigated in detail, at constant reactive gas flow rates, BNNT formation efficiency increases with increasing temperature from 1000 ^oC to 1200 ^oC. Likewise, when the reaction temperature kept constant, BNNT yield increased with increasing NH_3 flow rate.

Generally, bamboo-like morphologies were observed. However, at lower heating rates different morphologies such as onion like bases were detected.

Nanohorn like morphologies, getting thinner through the tip but thicker at the bottom were more frequently observed at low heating rates and low NH_3 flow.

All BNNT morphologies displayed curly entangled growth which supports the TEM analysis. Low metal oxide ratio caused curly entangled nanotubes with complex shapes [27, 116]. Distrubition of catalytic particals could be getting lower with the low catalytic oxide content in the precursor mixed which result in more place to nanotubes to grow in every direction causing curly BNNTs. Also, due to the uneven precipitation during the growth could result in stress buildup that cause nanotube the bend. [122].

4.4.2 Raman Spectroscopy Analysis

As-synthesized samples were characterized by Raman Spectroscopy. BN structures depict well-known strong tangential peak at 1365 cm^{-1}, which is attributed to E_{2g} Raman active mode of BN band. This mode originated from in plane counterphase vibration of the B-N bond due to the opposite movement of the B and N atoms on the same plane. Moreover, depending on the size of the BN structures E_{2g} mode shifted. However, in case of nanotube structures, this shift is more pronounced at smaller nanotubes, which have less than ten walls. On the other, hand full-width half-maximum value of the peak increase from bulk h-BN to BNNT.

Raman spectroscopy measurements were conducted on the BNNTs on Si-substrates. One measurement of the sample does not represent the whole samples due to the inhomogeneity of the BNNT coverage. Therefore, 20 different points on the substrates were analyzed by the Raman spectroscopy for every BNTNT growth in the experimental matrix.

Raman data collected from every experiment were processed by adding 20 spectra by each other for one sample and taking the average of all. As a result of this, signal to

noise ratio of the spectrums was increased, and one spectrum with improve intensity was analyzed.

4.4.2.1 Raman Surface Coverage Determination

Raman peak intensity was affected by the type of the molecule, laser source, and sample concentration. According to these effects, BNNT coverage on the surface of the substrate could be determined since same laser source and sample species were same, peak intensity only depends on the sample concentration. In figure 4.11, Raman spectrums of the two sample grown at the same temperature but different flow rates were shown. BNNTs grew at 1100 ^{o}C, 10 ^{o}C/min and 100 sccm flow rate show very small BN structures on the Si substrate, on the other hand at 1100 ^{o}C, 10 ^{o}C/min, and 200 sccm NH_3 flow, very long BNNTs can be observed from SEM micrograph. When we compare the peak intensity at 1365 cm^{-1}, 200 sccm gives higher intensity than 100 sccm and the intensity of Si-substrate peak at 556 cm^{-1} gets lower with higher coverage. Because at high coverages, the laser spot cannot reach the Si-substrate easily and the substrate peak starts to fade away. In the light of this point, the ratio between BN peak intensity and the Si-substrate intensity gives coverage ratio (arbitrarily) since the whole surface of the substrate was scanned by taking measurements of 20 different points. The coverage ratio of the sample is related to the yield of the production, when the ratio is high, BNNT yield was also high. Coverage results were presented in Table 4.1.

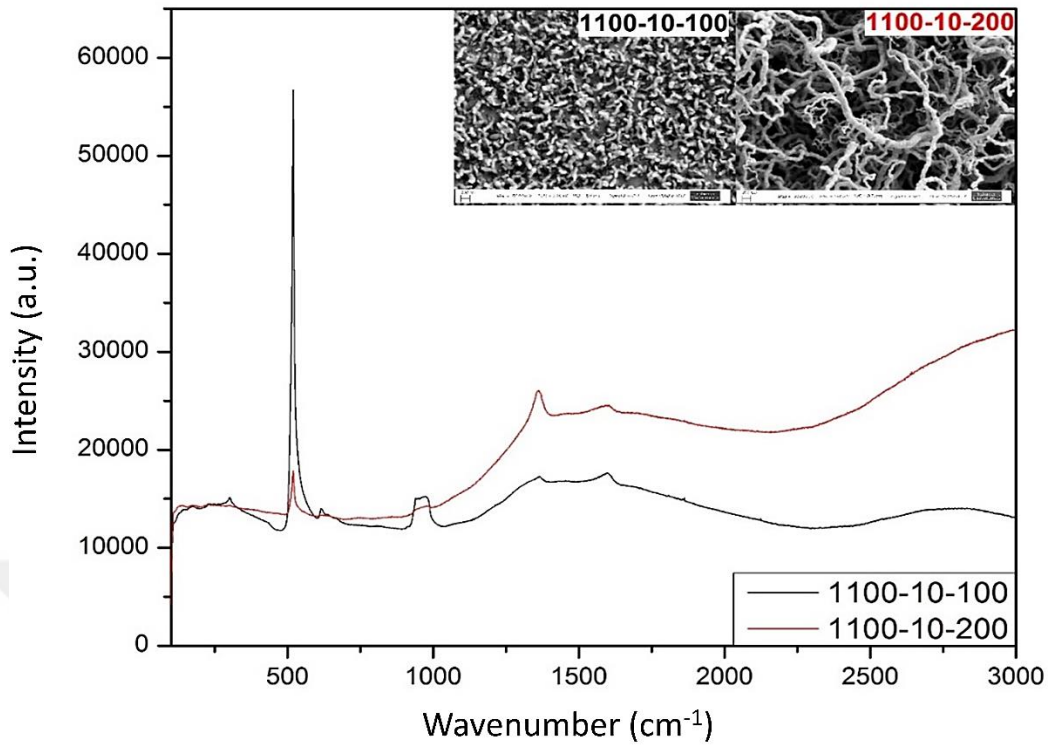

Figure 4. 11: BNNT peak intensity-coverage relation at different flow rates.

4.4.2.2 Raman Film Thickness Determination

Curly and entangled structure of the as synthesized samples make its length measurements challenging with microscopy techniques. Moreover, individual measurements did not represent the whole sample. Therefore, Raman spectroscopy was used to determine the BNNT film thickness on the Si-substrate, since it gives a better representation of the real structure. In this method, although exact length of the nanotubes could not be identified, entire thickness created by curled tubes can be determined. Short nanotube results in thin film thickness, longer nanotubes reveals thicker BNNT films. Therefore, errors in the length to diameter ratio (aspect ratio) determination were minimized. However, the actual length of individual nanotubes was not determined by this method, curly nature of the nanotubes reveals lower BNNT film thickness than actual length. Nevertheless, this problem was overcome by the

combinative usage of coverage (BN/Si peak ratio) with film thickness. Thus, fully-grown BNNTs reveal lower thickness due to the more entangled nature could be selected efficiently.

Determination of metal oxide film thickness with the optical systems was frequently used in the literature. Transmitted lights from two parallel surfaces (film surface and substrate surface) create interference fringes due to the phase differences. Frequency difference between these interference fringes directly related to the film thickness of the substrate called Fabry-Perot resonances. Equation is given below;

$$d = \frac{m}{2n\,(\nu_2 - \nu_1)}$$

In this equation, d (film thickness) can be found by the ratio of the number of minimum (m) between interferences to refractive index of the coating (n) and wavenumber differences between lowest and highest interferences $(\nu_2 - \nu_1)$. In this equation refractive index of the metal oxide coatings before the BNNT growth were neglected due to the very low thickness of the metal oxide layers (~30 nm).

Raman spectra of the BNNT films over the substrate reveal three interferences. BNNT film thickness was determined by fitting of the interferences. To increase the accuracy of the results, an average of the 20 measurements which taken from different places of the substrates were used. Representative interference fringes and the fitted result was shown in figure 4.12. Calculated film thicknesses for all samples were given in table 4.1.

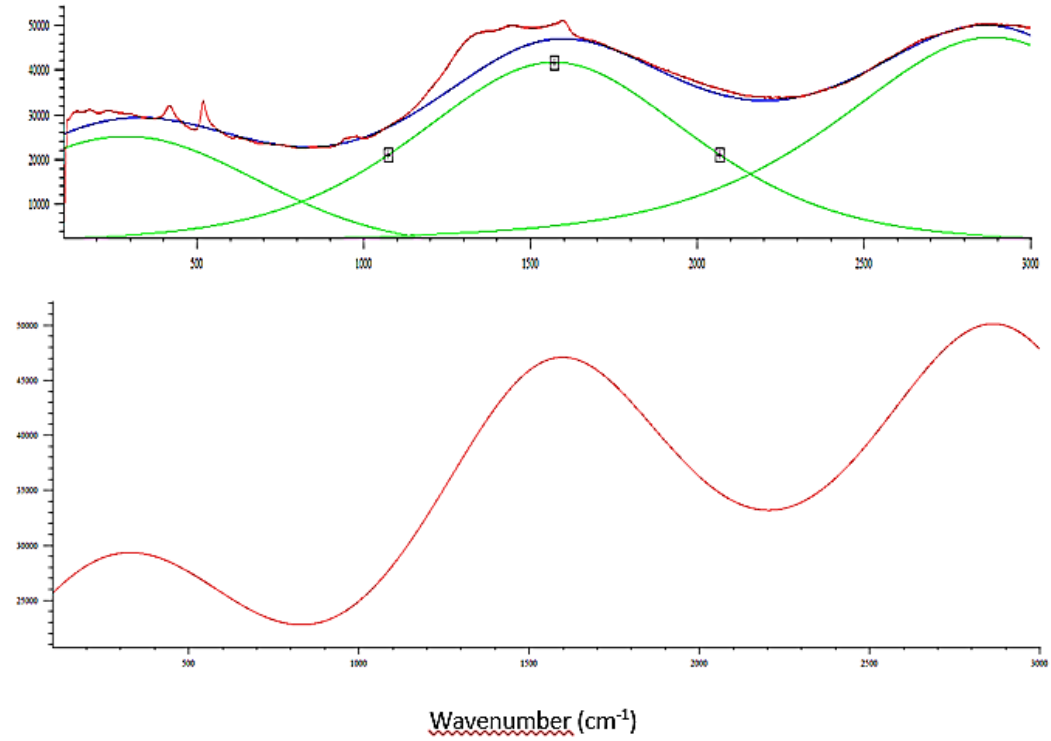

Figure 4. 12: Representative fit of the Raman spectrum for 1200-5-150 sample and resulting interference

4.5 Discussion: BNNT Production Optimization for Conventional Catalyst System

All responses collected from 27 points in the experimental matrix were shown in Table 4.1.

Table 4. 1: Responses collected from all samples from SEM and Raman analysis

Process Factor Levels (Un-coded domain)			Process Factor Levels (Coded domain)			Responses				
[A]Reaction Temperature (˚C)	[B] Reaction Rate (˚C/min)	[C] NH3 Flow Rate (sccm)	A	B	C	AverageDiameter (nm)	Std Dev	[R1] Coverage	[R2] Thickness (µm)	[R3] Aspect Ratio (µm/ µm)
1000	5	100	-1	-1	-1	38.44	18.64	0.66	2.03	52.80
1000	5	150	-1	-1	0	41.98	18.58	0.28	1.78	42.41
1000	5	200	-1	-1	1	36.10	13.39	0.18	1.93	53.46
1000	10	100	-1	0	-1	47.61	11.79	0.22	1.98	41.58
1000	10	150	-1	0	0	55.66	27.38	0.69	1.88	33.78
1000	10	200	-1	0	1	43.15	19.23	0.13	1.72	39.86
1000	15	100	-1	1	-1	42.78	12.42	0.21	1.96	45.82
1000	15	150	-1	1	0	72.88	27.00	0.48	1.95	26.75
1000	15	200	-1	1	1	47.19	18.46	0.08	1.53	32.42
1100	5	100	0	-1	-1	38.11	12.35	0.95	2.04	53.53
1100	5	150	0	-1	0	35.00	14.05	0.69	2.00	57.14
1100	5	200	0	-1	1	40.00	6.81	0.50	2.03	50.75
1100	10	100	0	0	-1	55.16	15.04	0.30	2.06	37.35
1100	10	150	0	0	0	56.02	28.63	1.50	2.07	36.95
1100	10	200	0	0	1	52.36	28.70	1.45	2.11	40.30
1100	15	100	0	1	-1	38.95	11.03	0.64	2.10	53.92
1100	15	150	0	1	0	50.06	22.77	1.18	1.98	39.56
1100	15	200	0	1	1	44.43	18.99	0.62	2.06	46.37
1200	5	100	1	-1	-1	59.82	19.60	1.17	2.16	36.11
1200	5	150	1	-1	0	46.09	17.63	1.47	2.14	46.43
1200	5	200	1	-1	1	49.88	21.33	1.83	2.16	43.31
1200	10	100	1	0	-1	102.36	56.82	1.79	2.19	21.39
1200	10	150	1	0	0	48.47	21.95	1.55	2.09	43.12
1200	10	200	1	0	1	53.14	19.60	1.71	2.15	40.46
1200	15	100	1	1	-1	94.52	33.52	1.71	2.15	22.75
1200	15	150	1	1	0	53.25	22.79	1.56	2.10	39.43
1200	15	200	1	1	1	52.91	20.84	1.75	2.16	40.82

The values of b approximate resulted from the regression analysis are reported in table 4.2.

Table 4. 2: Determined b approximates from regression analysis

	B0	F1	F2	F3	F1F2	F1F3	F2F3	F1^2	F2^2	F3^2
Surface Coverage (Y1)	0.937	+0.645								
Film Thickness (Y2)	2.019	+0.141		-0.045		+0.063				
Aspect Ratio (Y3)	41.977	-1.946	-4.895			+4.900		-7.166	+6.343	

4.5.1 Effect of process parameters on surface coverage (y1)

Contour diagram for surface coverage changing according to the level of heating rate and reaction temperature, predicted vs. actual plots and corresponding ANOVA analysis results are depicted in figure 4.13, respectively. ANOVA results indicated that the linear surrogate model is significant ($p< 0.1$).

Statistical analysis suggested that the surface coverage (as defined in section 4.4.2.1) is solely dependent on the reaction temperature and is independent of other factors. Temperature dependence of the coverage can be explained by the yield of the BNNT production, which suggests that efficient formation of B_2O_2 reactive phase only increase with increasing temperature due to the reaction between MgO and B probably activated at elevated temperature. In addition, another factor could be the magnesium evaporation temperature, which is at 1098 ^oC. It seems that besides catalytic coating, Mg in the

precursor powder was necessary to form catalytic droplets to enhance BNNT formation over the substrate.

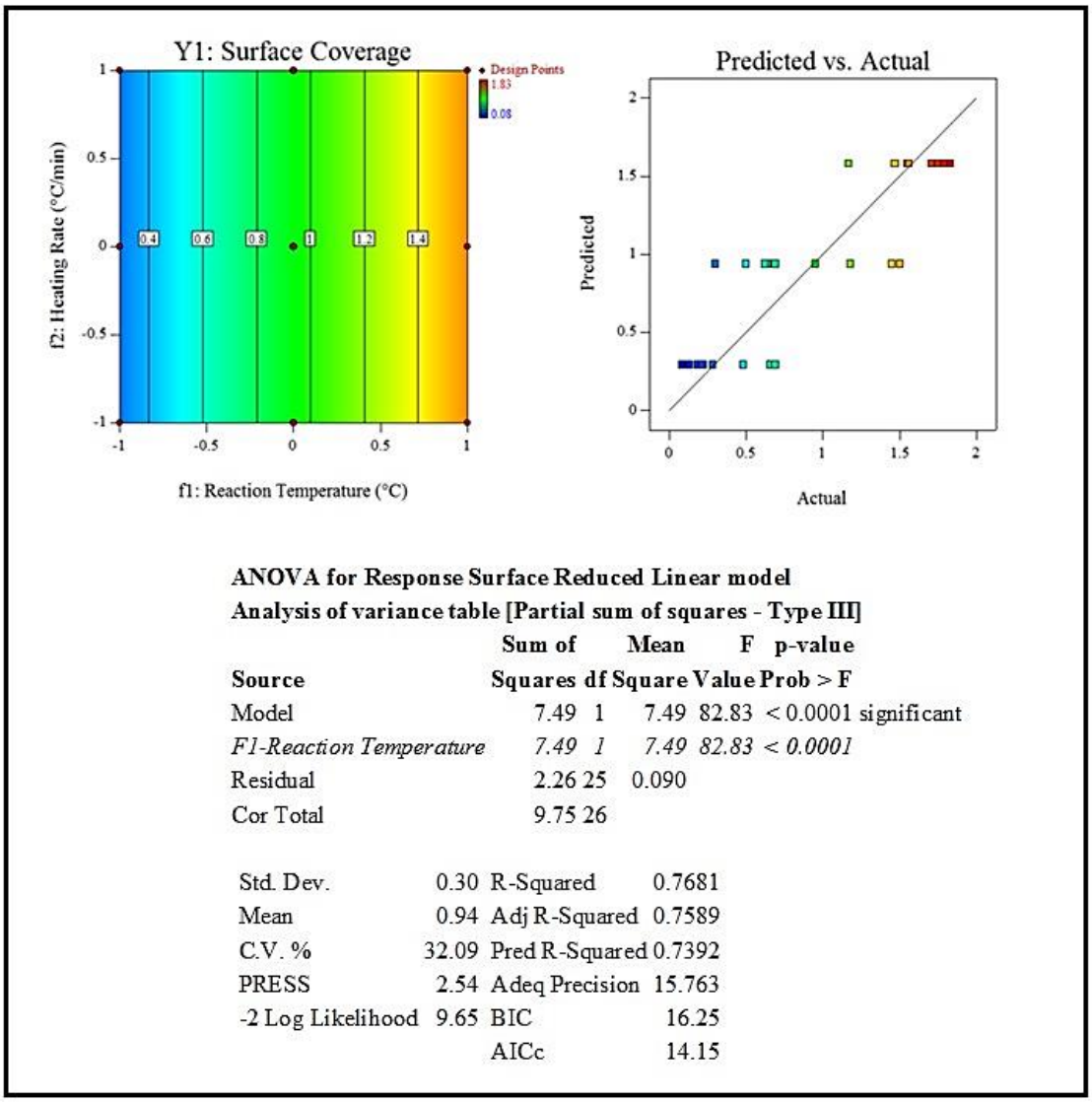

ANOVA for Response Surface Reduced Linear model
Analysis of variance table [Partial sum of squares - Type III]

Source	Sum of Squares	df	Mean Square	F Value	p-value Prob > F	
Model	7.49	1	7.49	82.83	< 0.0001	significant
F1-Reaction Temperature	*7.49*	*1*	*7.49*	*82.83*	*< 0.0001*	
Residual	2.26	25	0.090			
Cor Total	9.75	26				

Std. Dev.	0.30	R-Squared	0.7681
Mean	0.94	Adj R-Squared	0.7589
C.V. %	32.09	Pred R-Squared	0.7392
PRESS	2.54	Adeq Precision	15.763
-2 Log Likelihood	9.65	BIC	16.25
		AICc	14.15

Figure 4. 13: Contour diagram for surface coverage changing according to level of heating rate and reaction temperature, predicted vs. actual plots and corresponding ANOVA analysis results

4.5.2 Effect of process parameter on film Thickness (y2)

Contour diagram for film thickness changing according to levels of flow rate and reaction temperature, predicted vs. actual plots and corresponding ANOVA analysis results are depicted in Figure 4.14. Statistical analysis suggested that reaction temperature (f1) and flow rate(f3) and their combinative effect (f1*f3) plays a significant role on the film thickness. Non-linear contour profile depicted on figure 4.14

is due to combinative effect of f1 and f3. Predicted vs. actual plots suggests that collected data is grouped in three clusters which shows the presence of a dominant factor in data which is reaction temperature (f1) in this case. Also experimentally determined data was scattered mostly for minimum f1 suggesting that model is mostly effective for f1=0,1 cases. However the model is significant ($p< 0.1$). This problem is reflected in a lower $R^2= 0.7455$ for predicted values. So the exact effect of f3 may not be monitored well enough which then leaves f1 as the sole effective factor in that response.

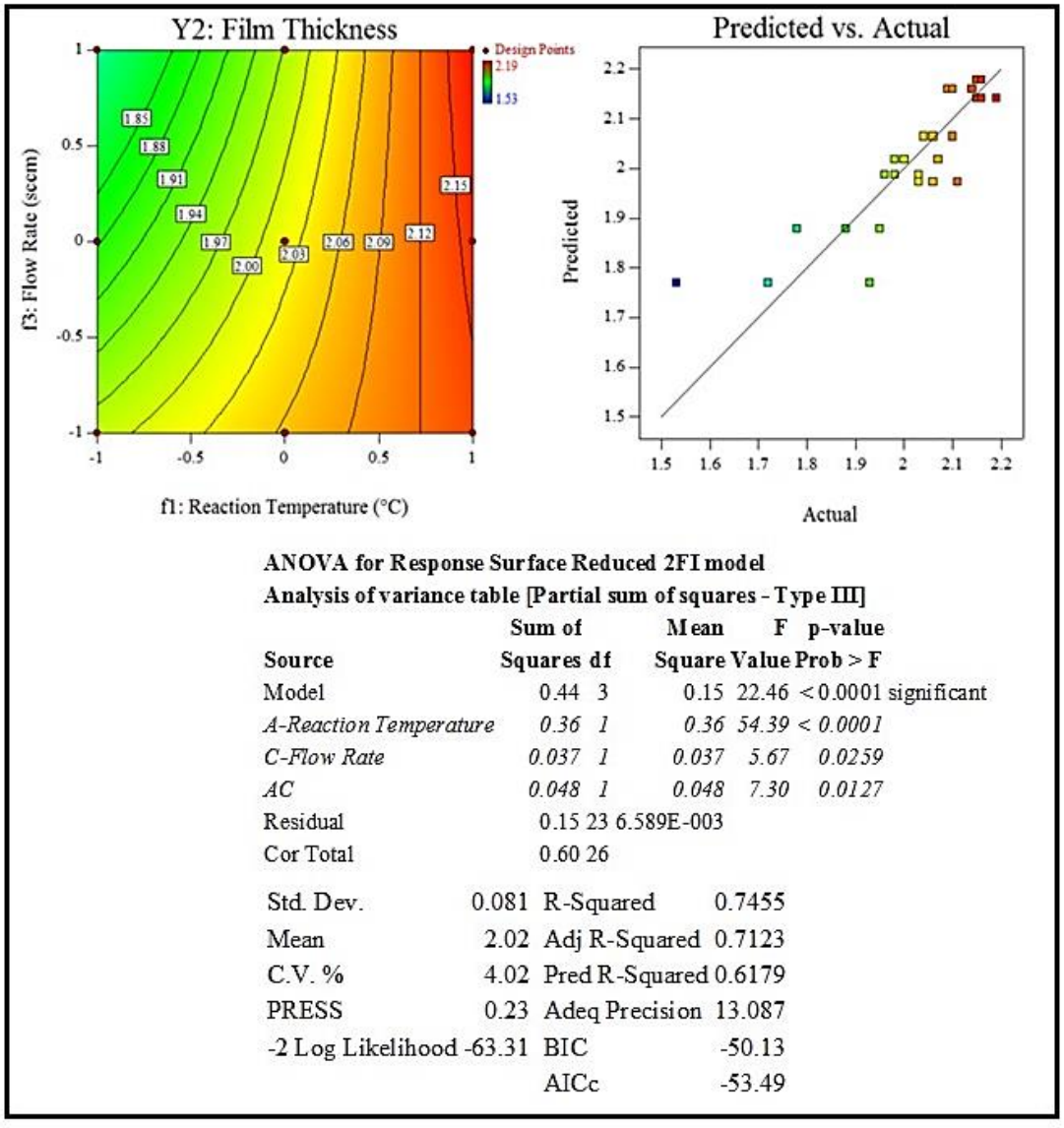

ANOVA for Response Surface Reduced 2FI model
Analysis of variance table [Partial sum of squares - Type III]

Source	Sum of Squares	df	Mean Square	F Value	p-value Prob > F	
Model	0.44	3	0.15	22.46	< 0.0001	significant
A-Reaction Temperature	*0.36*	*1*	*0.36*	*54.39*	*< 0.0001*	
C-Flow Rate	*0.037*	*1*	*0.037*	*5.67*	*0.0259*	
AC	*0.048*	*1*	*0.048*	*7.30*	*0.0127*	
Residual	0.15	23	6.589E-003			
Cor Total	0.60	26				

Std. Dev.	0.081	R-Squared	0.7455
Mean	2.02	Adj R-Squared	0.7123
C.V. %	4.02	Pred R-Squared	0.6179
PRESS	0.23	Adeq Precision	13.087
-2 Log Likelihood	-63.31	BIC	-50.13
		AICc	-53.49

Figure 4. 14: Contour diagram for film thickness changing according to levels of flow rate and reaction temperature, predicted vs. actual plots and corresponding ANOVA analysis results

4.5.3 Effect of process parameter to BNNT aspect ratio (y3)

Previous responses were focused on the process efficiencies which is aimed to be maximum. Aspect ratio on the other hand focuses to the dimensions of nano-strcutures formed on substrate surfaces after pre-determined and fixed process conditions. However, by definition the aspect ratio is determined by Film thickness (y2)/nanotube diameter. Since nanotube structures were curly and quite long for some cases, BNNT diameters observed under SEM were divided to film thickness values from RAMAN analysis and that procedure is the subject of another thesis work. Discussion here was limited with effect of reaction temperature (f1) and if its maximization (as suggested by y2) necessarily increases the aspect ratio as well.

By comparing figures 4.14 and 4.15 one can approximate how diameter of BNNTs changes with the known effect of film thickness. Figure 4.15 suggests that y3 is not maximized at any levels of f1 (corresponding to a green region). and ANOVA analysis suggests that heating rate (f2, p=0.0038) is the most effective factor. Although the vertical growth of BNNTs was dominated by reaction tempearature (thermal effect), the horizontal growth is mostly effected by heating rate (f2) which is time dependent (kinetic effect). On the other hand, f1 has a significant interaction with f3 (flow rate) (p=0.014) suggestion which signals the existance of an activation energy required for reactive gas/BNNT reaction.

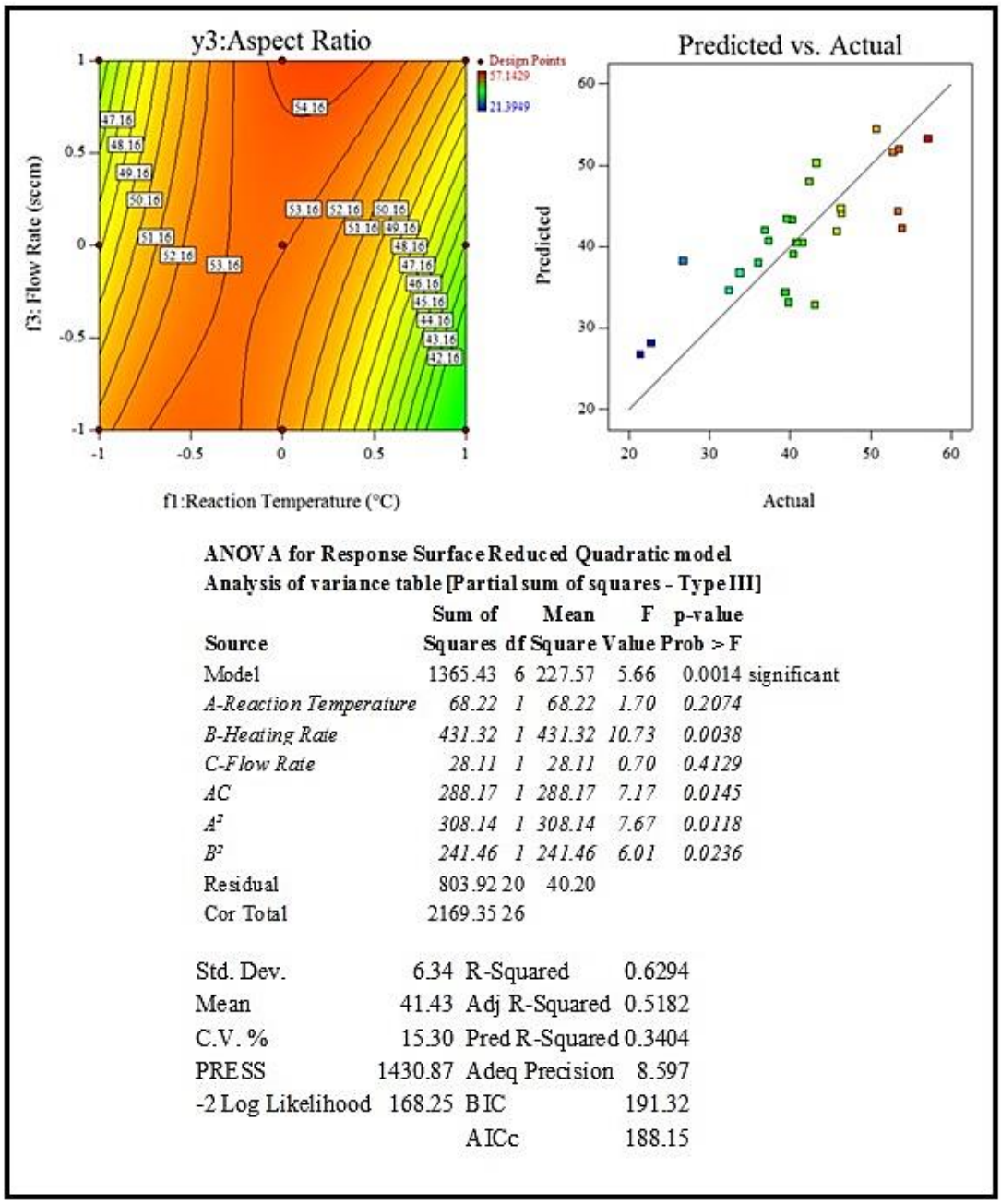

ANOVA for Response Surface Reduced Quadratic model
Analysis of variance table [Partial sum of squares - Type III]

Source	Sum of Squares	df	Mean Square	F Value	p-value Prob > F	
Model	1365.43	6	227.57	5.66	0.0014	significant
A-Reaction Temperature	*68.22*	*1*	*68.22*	*1.70*	*0.2074*	
B-Heating Rate	*431.32*	*1*	*431.32*	*10.73*	*0.0038*	
C-Flow Rate	*28.11*	*1*	*28.11*	*0.70*	*0.4129*	
AC	*288.17*	*1*	*288.17*	*7.17*	*0.0145*	
A^2	*308.14*	*1*	*308.14*	*7.67*	*0.0118*	
B^2	*241.46*	*1*	*241.46*	*6.01*	*0.0236*	
Residual	803.92	20	40.20			
Cor Total	2169.35	26				

Std. Dev.	6.34	R-Squared	0.6294
Mean	41.43	Adj R-Squared	0.5182
C.V. %	15.30	Pred R-Squared	0.3404
PRESS	1430.87	Adeq Precision	8.597
-2 Log Likelihood	168.25	BIC	191.32
		AICc	188.15

Figure 4. 15: Contour diagram for aspect ratio changing according to levels of flow rate and reaction temperature, predicted vs. actual plots and corresponding ANOVA analysis results

4.6 Conclusion of Conventional MgO/Fe_2O_3 Catalyst System for BNNT Production and Optimization

BNNTs were synthesis with TCVD method GVT approach with MgO/Fe_2O_3 conventional catalysis system at 1000 ^oC to 1200 ^oC similar to the literature. Because

without MgO catalyst vapor, BNNT growth on the substrates was not achieved. Preliminary studies were showed that precursor ratio amorphous boron powder/MgO/Fe_2O_3 should be 4/1/1 respectively for homogeneity of the BNNT coating on the substrate and reaction time at maximum temperature was stabilized at 30 minutes. UV-vis studies of the extracted nanotubes showed that BNNTs synthesized at different temperatures 1000 ^oC, 1100 ^oC and 1200 ^oC, have almost the same (5.8 eV) band gap, independent of morphology and diameter. TEM analysis can be shown that BNNTs were hollow, and have a multiwalled structure with the diameters of the BNNTs are changing from 30 nm to 80 nm. Most of the nanotubes are grown in entangled curly fashion and showed cup type bamboo like hollow morphologies. Curved nanotubes have close tips, some of them were incorporated with metal particles and some of them without which suggest the mixed (base and tip) growth mode of the BNNTs. Optimization experiments were carried out to find three primary response substrate coverage, film thickness and BNNT aspect ratio to determine effects of CVD process parameters (reaction temperature (f_1), heating rate (f_2) and reactive gas flow rate (f_3)) on the growth quality. SEM analysis (followed by image processing) for nanotube diameter and RAMAN analysis for grown BNNT thickness measurements and substrate surface coverage were used. SEM micrographs were investigated in detail, at constant reactive gas flow rates, BNNT formation efficiency increase with increasing temperature from 1000 ^oC to 1200 ^oC. Likewise, when the reaction temperature kept constant, BNNT yield increased with increasing NH_3 flow rate. Generally, bamboo-like morphologies were observed. However, at lower heating rates different morphologies such as onion like bases were detected. Nanohorn like morphologies which getting thinner through the tip but thicker at the bottom were more frequently observed at low heating rates and low NH_3 flow. Optimization responses concluded that BNNT

synthesis with conventional catalysis system mostly depended on the temperature of the synthesis. Although high aspect ratios can be achieved low temperatures (1000 ^{o}C) below Mg boiling point, BNNT coverage (yield) and the film thickness were low. High coverage, high film thickness and good aspect ratio can be reached at high temperature 1200 ^{o}C (over Mg boiling point), high NH_3 flow rate (200 ^{o}C) and low heating rate 5 ^{o}C/min.

CHAPTER 5

5 NEW $KFeO_2$ CATALYST SYSTEM for BNNT SYNTHESIS at LOW TEMPERATURES

5.1 Summary

In this chapter, alternative catalytic parent material ($KFeO_2$) was presented for BNNT synthesis instead of conventional catalytic system (MgO/FeO) used in the literature frequently and chapter 4. This chapter shows the synthesis and use of a novel alkali based catalyst that is to be used in BNNT synthesis by thermal CVD. The catalyst works at temperatures as low as 750^{o}C that is far below previously reported temperature ranges in the current state of the art (1100 ^{o}C -1300 ^{o}C). Phase analysis of newly introduced catalyst is conducted via XRD. The structural characterization was carried out by Raman Spectroscopy. The microstructure was investigated by SEM and TEM analysis by focusing on size and wall structure of BNNTs, which show that highly crystalline, long and straight MWBNNTs can be produced on the ceramic substrate at low temperatures by using $KFeO_2$ as the parent material. The growth mechanism and the chemical composition was revealed by TEM-EDS and EELS measurements.

5.2 Objectives of Research

BNNT production with CVD has not been as smooth as expected, unlike CNTs. Because crystallization of BN requires very high temperatures (1100 ^{o}C-1700 ^{o}C) which reduced to the possibility of materials and setup parts that can be used in the synthesis.[17] High temperatures cause side reactions to form metal borides, which in turn cause loss of the catalyst efficiency. In addition to this, low solubility of BN in traditional metal catalyst caused poor wetting conditions and limited to usage of metal catalysts for the

pyrolytic growth of BNNTs. Moreover, toxic nature of boron precursor gases (such as borazine) for pyrolytic growth is another limiting factor. Therefore controlled growth of the BNNTs is very challenging due to the high reaction temperatures and slow catalytic activity of the working metal oxide catalyst systems. [23, 27] Only one or two effective catalysts have been revealed for BNNT synthesis although catalytic activity was slow (in section 2.4). Large-scale production of BNNT with CVD was only achieved via BOCVD method by only one group. However, the specific design of the induction furnace and expensive system parts restricted its extensive usage by other research groups. On the other hand, BNNTs can be synthesis on the catalytic material coated substrates by TCVD method using traditional horizontal furnace like in chapter 4 and in the literature. However, highly crystalline BNNTs can only be achieved at high temperatures, good substrate coating, efficient oxygen formation from catalytic materials and proper mixing of the precursors. Because small local perturbation of the system drastically change the crystallinity and shape of the BNNTs.[17] On the other hand, high temperatures (e.a. 1200- 1500) cause the substrate deformation and loss stability which also influence purity and crystallinity of the resulting BNNT coated system. Problems in BNNT synthesis were summarized below.

- Always high temperature for BNNT production
- The choice of catalyst during the synthesis of BNNTs
- The choice of suitable technique for large scale production
- Long reaction times
- Challenging to obtain high purity BNNT
- Cost

We have already known there are only handful of catalytic materials which are used in BNNT synthesis in TCVD method and they can only be effective over 1000 ^{o}C. In fact, good crystallinity and high substrate coverage require much higher temperatures over 1200 ^{o}C (see Chapter 4.6). The objective of this research is mainly present a new catalytic material system that can allow BNNT formation below 1000 ^{o}C in TCVD system. By this way, the growth of the nanotubes could be controllable, and amount of side reactions during synthesis could be prevented. Also, usage of the traditional horizontal furnace without induction furnace, elimination of substrate coating and low temperatures reduce time and cost of the process. In addition, the growth of the nanotubes in the reaction powder caused a lot of impurities (Boron complexes, BN structures, boron oxide), for this reason, using a substrate is crucial for obtaining pure nanotubes. To achieve growth of the BNNT on the substrate, the catalytic material should have high vapor pressure during the growth. We also want that the catalytic material should be cheap and non-toxic.

However, by reducing temperature, we did not want to lose quality and crystallinity of the nanotubes. Templated synthesis and hydrothermal synthesis at low temperatures caused amorphous BNNT formation, impurities, B-N-C hybrid nanotube formation and problems due to the template removal. Therefore, finding a catalytic material, which has high vapor pressure and allowed crystallization of BNNTs at low temperatures, is crucial to use in TCVD process.

Alkali metals are thought to be good candidates due to their high vapor pressures and nontoxic natures compared to the other metals (such as Cadmium). In addition, some examples showed BN particles could be produced by using alkali metals. The patent in 1963 mention that production of BN by using alkali metal oxide and alkali metal borides with silicon and aluminum between 200 ^{o}C and 1200 ^{o}C.[123] In 2000, Terauchi et

al. synthesized BNNT and BN cones by using powder h-BN and Li vapor.[124] They reported that formation of BNNTs was not possible without lithium vapor however reason behind was not clarified. In addition, it was reported that Li compounds have promotion effect on crystallization of graphite-like BN. By using lithium salts, formation and ordering of structure of graphite-like BN were enhanced.[125, 126] Finally in 2013, Li_2O was used to produced BNNTs at BOCVD method.[29]According to the studies in literature, alkali metals that have high vapor pressures, also have promotion effect of BN crystallization. Nevertheless, only Lithium compounds were used in BN synthesis due to the stable nature of its oxide form compared to the other alkali metal oxides (Na_2O, K_2O) which are not stable. However, Li has no advantages according to the vapor pressure compared to the conventional Mg catalyst. Stable nature of the Li_2O make its reduction very hard, and evaporation of metallic Li is 1350 ^oC higher than magnesium. Therefore, using other alkali metal oxide in a way that they can be stable during BNNT synthesis is vital to reduced BNNT synthesis temperature below 1000 ^oC.

5.2.1 Potassium as a candidate

Best possible candidate for low temperature synthesis as an alkali metals are sodium and potassium instead of lithium due their higher vapor pressures. Even if potassium ionic radii (K^+: 138 pm) is much higher than ionic radii of the Li (Li^+:76 pm) which is very close to the conventional catalyst Mg (Mg^{2+}: 72 pm), its low melting point makes potassium more desirable than other alkali metals. Cesium, on the other hand, has highest vapor pressure than all, but it is very high radii limited its usage (Figure 5.1). In addition to that, when we compare Ellingham diagram of alkali metal oxides, K_2O can be reduced more efficiently than Na or Li oxide, which would make K_2O effective B_2O_2 producer by enhancing the formation B_2O_2 intermediate phase by reaction of K_2O and B.[127]

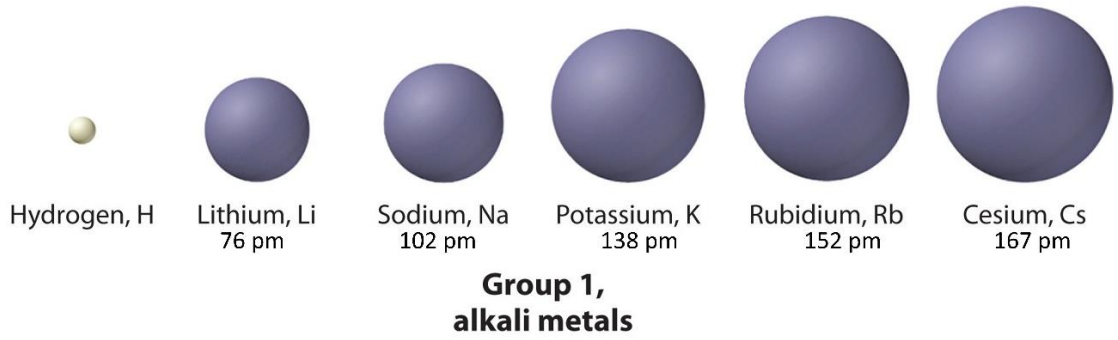

Figure 5. 1: Radius of the Alkali Metals

However, potassium is not stable in air, reacts vigorously with water. In addition, its oxide form is also highly reactive, and direct usage of potassium oxide (K_2O) is restricted by the unstable nature of the compound, which prevents most of the potential application of K_2O as a catalyst.

From this point of view, parent material which contains potassium in the structure can be used as a K/K_2O source. During the reaction, this material should release K/K_2O to the reaction environment with temperature. By this way, direct usage of reactive K_2O could be avoided. Best possible candidate for K source is $KFeO_2$, which contains 50 % potassium, and 50 % iron as mole ratio in its structure. It can release K and K_2O at high temperatures and reducing atmospheres [128-130].

When potassium is used as a promoter in the iron catalyst, $KFeO_2$ forms at the surface of the catalyst. There are some critical catalytic applications that $KFeO_2$ is involved such as an active catalyst in styrene production, Fischer-Tropsch hydrocarbon synthesis, water gas shift reactions and ammonia synthesis for a good catalytic performance. On the other hand, some reports mention that K promoted iron oxide catalyst loses its catalytic activity by simple loss of potassium.[129] We can use the property that is a disadvantage in iron oxide catalyst as an advantage for BNNT synthesis. Therefore, by using $KFeO_2$ during TCVD growth of BNNTs, we can have K_2O and iron oxide catalyst system instead of conventional catalyst double MgO, FeO.

5.2.2 $KFeO_2$

Compare to the highly reactive K_2O, $KFeO_2$ can be considered easier to handle. However, $KFeO_2$ is still unstable in atmospheric conditions due to its hygroscopic nature. It decomposes into KOH and hydrated Fe_3O_4, which in turn irreversibly deactivate catalyst when it contacts with moisture dominated air[130, 131]. Therefore, the catalyst was handled very carefully during synthesis and catalytic treatment. $KFeO_2$ was synthesized via organic precursor method at 700 ^oC and vacuum quenched in a desiccator. After cooling, synthesized $KFeO_2$ was kept in the glovebox. Only quick XRD measurement was done to identify the final product (Figure 5.2). The diffraction pattern of $KFeO_2$ revealed that monophasic crystal structure of the synthesized product. All peaks are very well matched with the pure orthorhombic structure with the Pbca space group described in the structural database (File no: 04-013-8446, a= 5.59 b= 11.22 and c=15.93 A). There was no sign of decomposition with the moisture. Actually, decomposition of the $KFeO_2$ can be observed with the color change. Since the color of the $KFeO_2$ was olive green when it decomposes with the moisture in the air, iron oxide is formed and the color changes to the red.

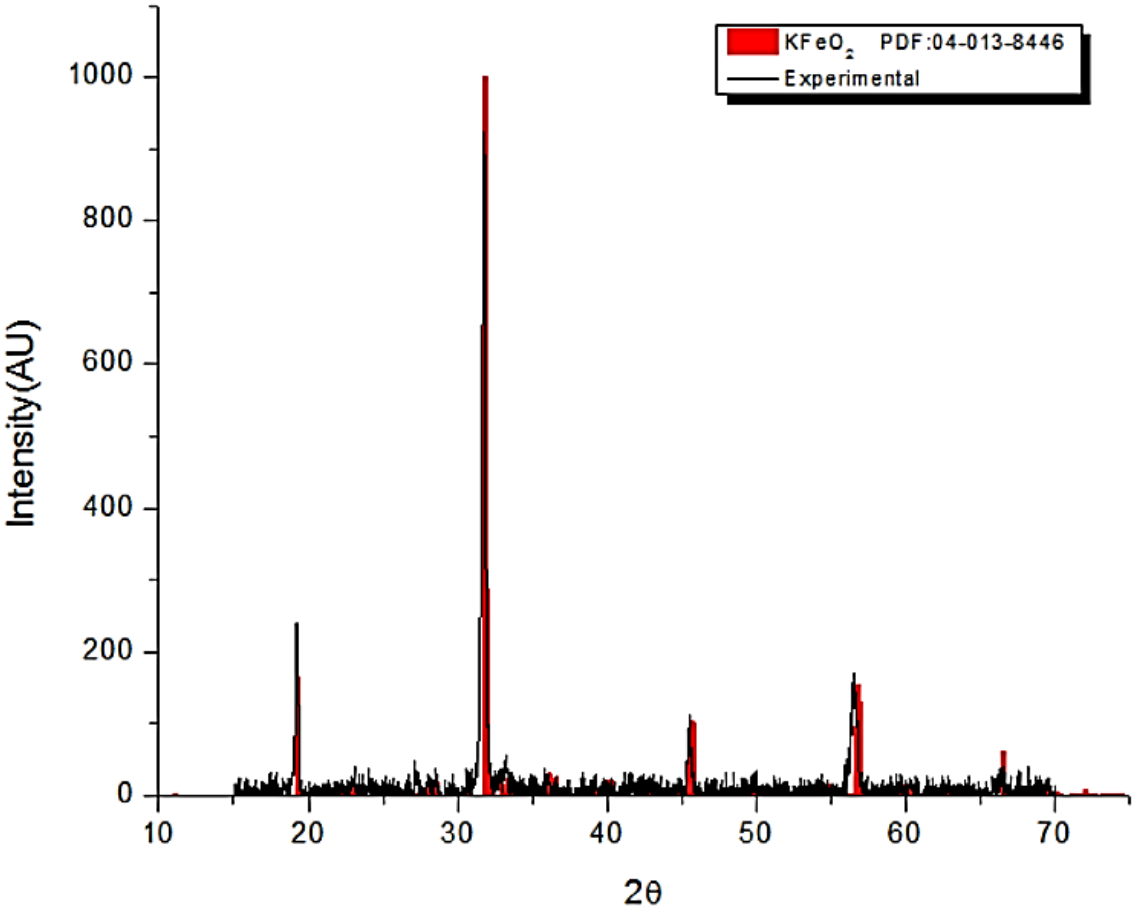

Figure 5. 2: XRD of as synthesized $KFeO_2$

5.3 BNNT production with $KFeO_2$ parent Material

BNNTs were synthesized through TCVD method GVT approach, very similar to the one previously reported procedure (see figure 3.4).[25] Solid boron powder and $KFeO_2$ were mixed (2:1 mole ratio), placed in a ceramic combustion boat, and then top of the combustion boat was covered by a ceramic substrate and positioned in the inner quartz tube in the glovebox. Then setup was placed horizontally into the furnace that was heated up under ammonia flow to 800°C and kept for 2 hours (see section 3.4.2 for details). When the system was cooled down, combustion boat was removed, and white coating of BNNTs on the wall of the crucible and on the ceramic substrate were observed (Figure 5.3).

Reaction temperature to form BNNT was determined around and over potassium boiling point related to the desorption of potassium from $KFeO_2$ phase with temperature and reducing atmosphere. Predicted reactions to synthesized BN are listed below.

$$2K_2O(s) + 2B(s) \rightarrow B_2O_2(g) + 4K(g)$$

$$2FeO(s) + 2B(s) \rightarrow B_2O_2(g) + 2Fe\ (s)$$

$$B_2O_2(g) + 2NH_3(g) \rightarrow 2BN(nanotube) + 2H_20(g) + H_2(g)$$

The White coating can be collected by sonication after removing powder from the crucible. Sonicated samples were centrifuged, and agglomeration occurred. The agglomerated product can be observed in Figure 5.4 without any purification with acids. The more straightforward method was extraction with carbon tape from the substrate. Since nanotubes were purer and not break apart due to the long sonication times.

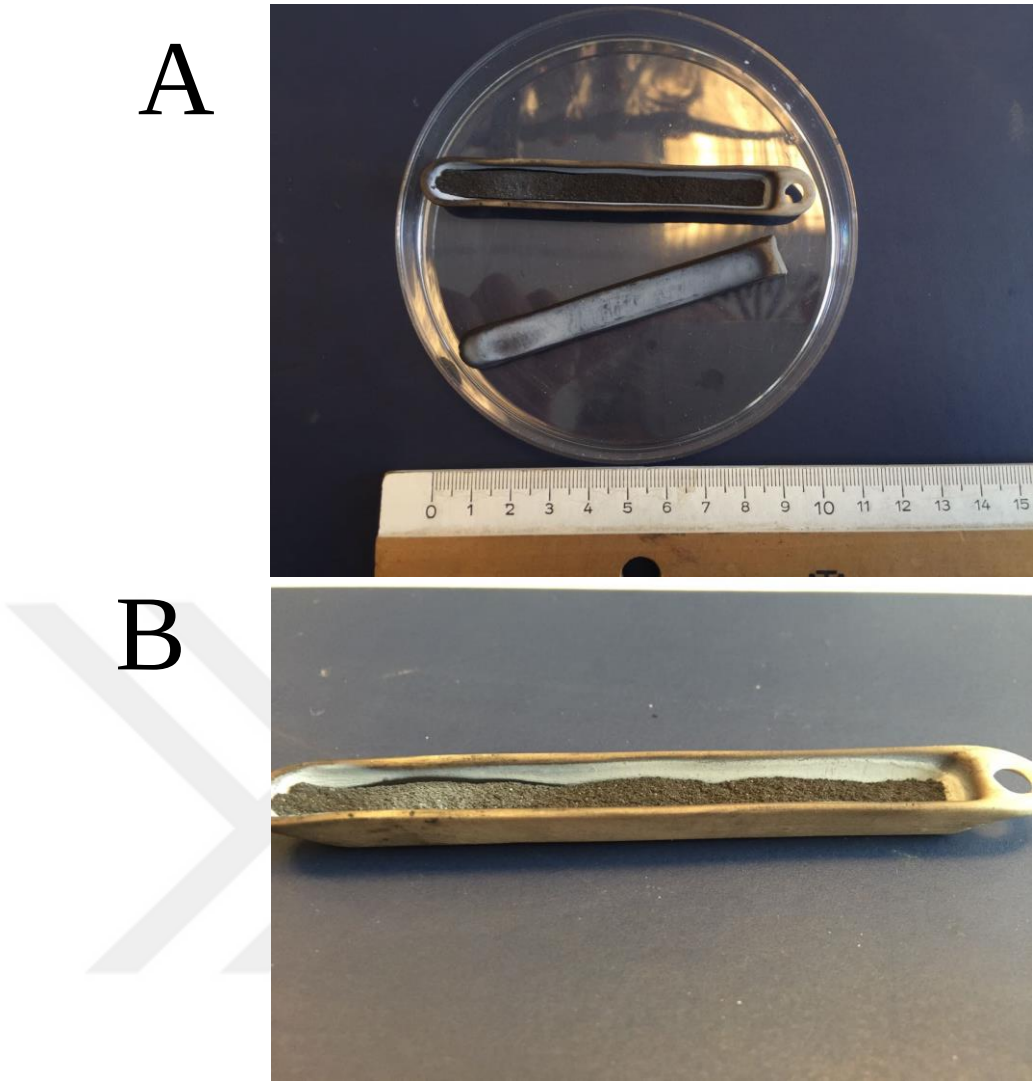

Figure 5. 3: As synthesized BNNTs on the substrates A) Ceramic substrate (bottom of the empty crucible, which was cut before and placed on the top of the combustion boat) B) walls of combustion boat

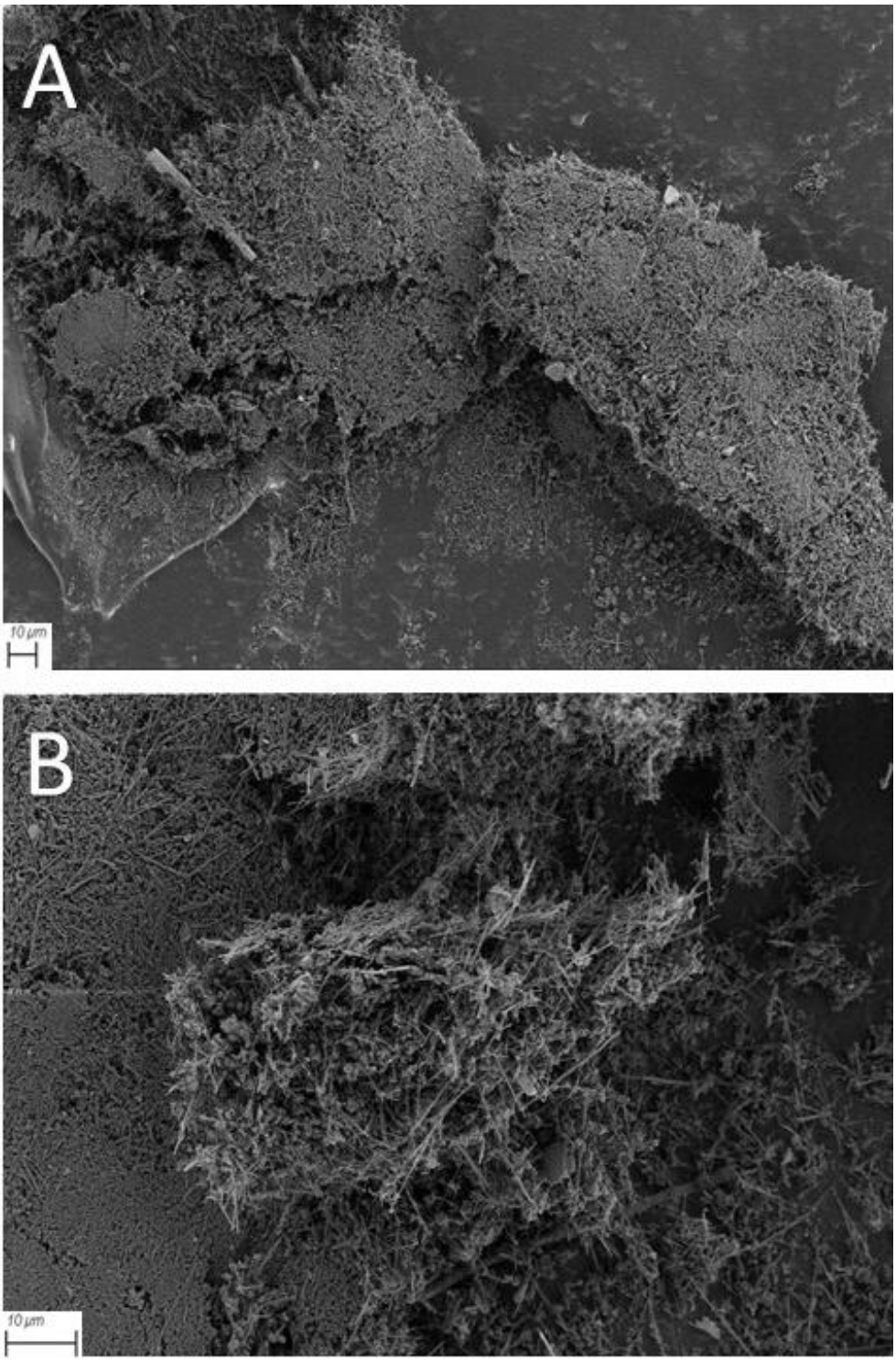

Figure 5. 4: Product after sonication and centrifucation (agglomerated product)

5.3.1 Results

5.3.1.1 SEM Analysis

Morphology of the as-grown BNNTs was investigated with SEM. Large area SEM image of the wall showed a very high coverage of BNNTs over the surface due to condensation of evaporated potassium on the wall of the combustion boat and ceramic substrate (Figure 5.5A). SEM micrographs reveal that morphology of the BNNTs strongly depends on reaction parameters and catalyst materials (precursor) used in the process. For example, same experimental setup was used for the conventional catalyst in chapter 4 and $KFeO_2$ synthesis in this study; only precursor materials are different. With conventional catalyst, as synthesized BNNTs were entangled and curly, mostly bamboo like morphology was observed. On the other hand, with $KFeO_2$, straight and well crystalline BNNTs were formed. Ma et al. reported that insufficient production of oxygen leads to the less B-O intermediate phases in the growth vapor which favors segmented bamboo like morphology by closing tube layers to reduce the surface energy.[17] Therefore, we can conclude that $KFeO_2$ in the precursor lead to the higher concentration of B-O intermediate phases despite the low temperature, which result in straight tubular BNNTs. High magnification micrograph of BNNTs in figure 5.5B showed that straight morphology of the nanotubes with diameters are very similar to the BNNTs growth at 1200 ^{o}C in chapter 4, around 80 nm, although much lower temperature (800 ^{o}C) was used. Usually, the diameter of the nanotubes is very dependent on the synthesis temperature when the temperature is increased; the diameter is also increased [27]. However, the result showed that nanotube diameter was also affected by the precursor materials used in the synthesis. As synthesized BNNTs on the crucible wall and the ceramic substrate can be simply taken by carbon tape (Figure 5.5C). The high aspect ratio of the tubes can be observed from the images. Average

lengths of the BNNTs are higher than 20 μm (Figure 5.5 and C) and hollow channel in the center of the tubes is the indication of the nice tubular morphology of the structure (Figure 5.5D).

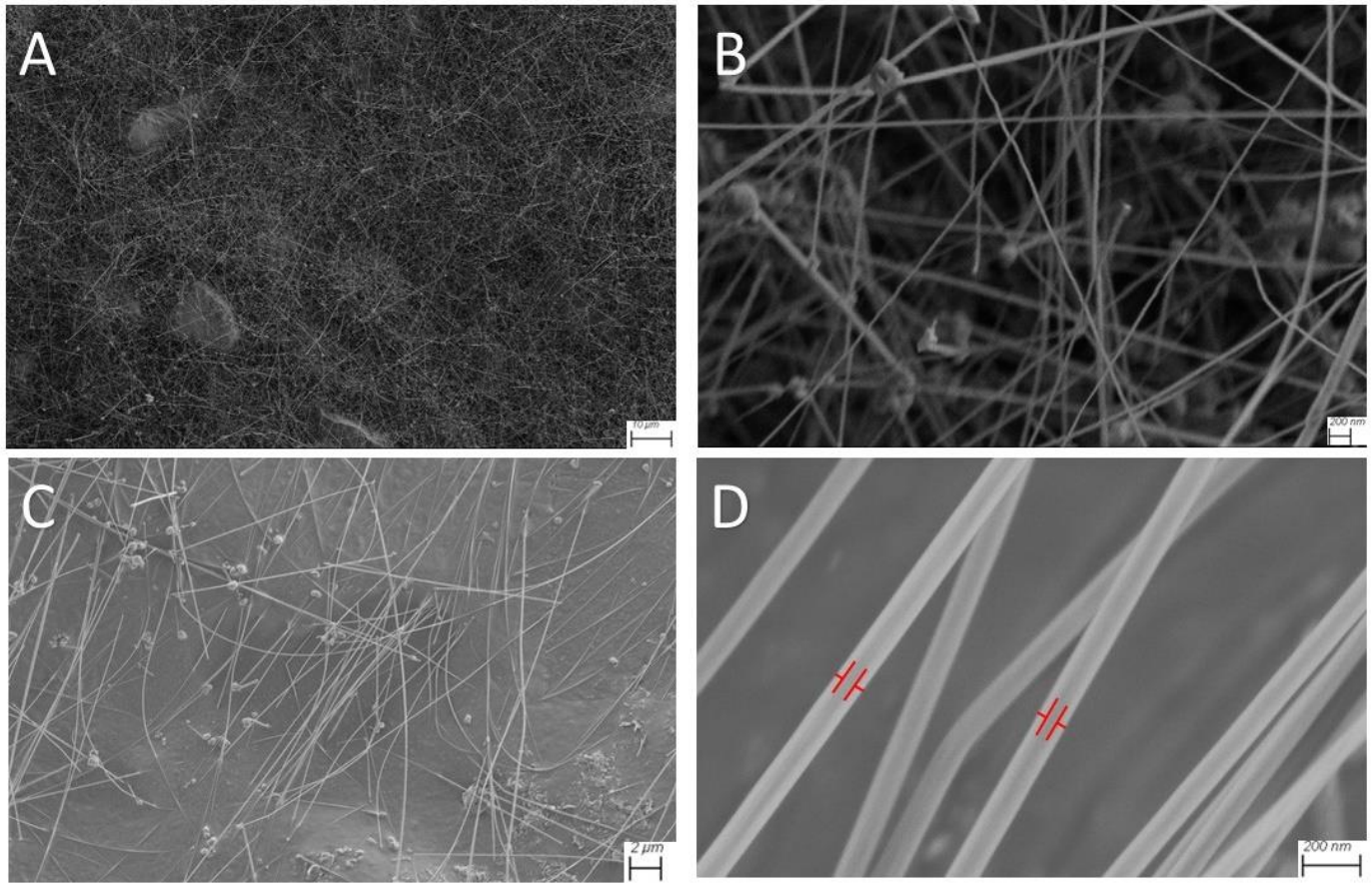

Figure 5. 5: A) Large area SEM micrograph of BNNTs on the ceramic substrate B) High magnification SEM micrograph of BNNTs on ceramic substrate C) Extracted nanotubes by carbon tape D) High magnification SEM micrograph of BNNTs, hollowed center pointed out by red indicators.

5.3.1.2 Raman Analysis

As grown nanotubes on the substrate depicted an intense peak at 1368 cm^{-1} with Raman spectral excitation at 532 nm with a Nd-YAG laser (Renishaw) which correspond to well-known Raman active E_{2G} mode belongs to the in plane counter phase B-N vibrational mode (Figure 5.6A). The high intensity of the well crystalline BNNTs surpass the low background signals originating from the ceramic substrate due to the thick coverage of the BNNT film on the surface. Full width at half maximum (FWHM) value (19 cm^{-1}) is relatively large compared to the bulk h-BN reported in the literature that indication of small crystal size.[132] The broadening of the peak is more pronounced at smaller crystal size in the single wall or couple walls structure compare to the large multiwall BNNTs in this work Figure (5.6B).[133, 134]

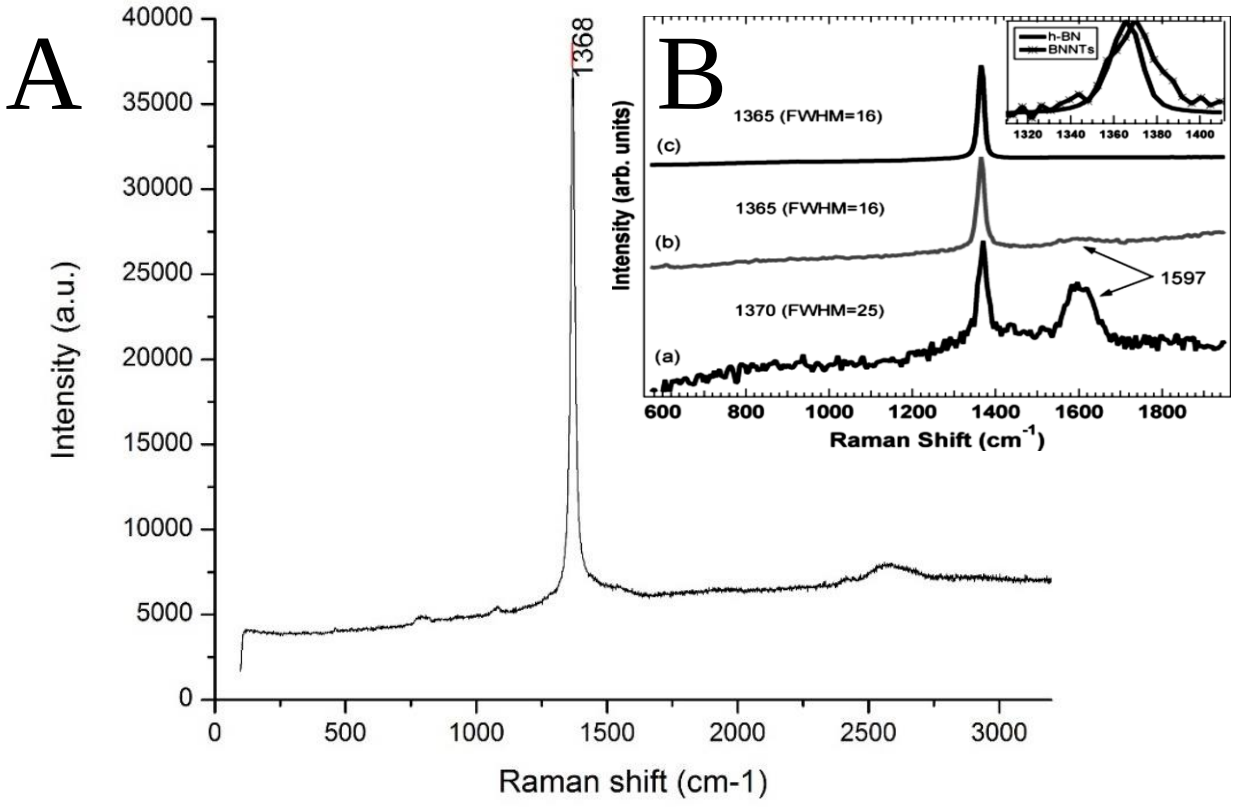

Figure 5. 6: A) Raman spectrum of crucible wall covered with BNNTs B) Raman spectra excited at 229 nm on (a) a BNNT-rich area in a standard TEM carbon grid (b) a particle of h-BN on the same grid (Figure 2b), and (c) highly crystalline powder h-BN (adapted from reference 134).

5.3.1.3 TEM Analysis

Sample preparation for TEM analysis was carried out by scratching the white sample on the walls of the crucible onto the copper grid. Transmission electron microscopy (TEM) analysis was used to determine microstructure, chemistry and the quality of the tubes. In Figure 5.7A-B, the long, straight and tubular structure of the synthesized product was similar to the ones observed by high magnification SEM (Figure 5.5D). Periodic dark contrast observed along the walls of the nanotubes are attributed to the well-defined tube structure due to the high quality of the BNNT synthesized with presented method (Figure 5.7C).[135, 136] It is attributed to either a thin BN-ribbon wrapped around the circular nanotube[135] (especially when the dark regions are alternating on both sides of the nanotubes) or to the local mixed circular and polygonal tube morphologies within multiple walls.[136, 137] Higher contrast on walls than lighter inner side can be observed from Figure 5.7D. [138] High-resolution TEM (HR-TEM) images show that sidewalls of the tubes are highly crystalline (Figure 5.7E). No amorphous structure was observed on the walls (Figure 5.7F). FFT of the recorded HRTEM image resembles a near zigzag conformation with a chiral angle of ~15 degrees, determined from the angle between 100 diffraction spots and the tube axis (Figure 5.8).

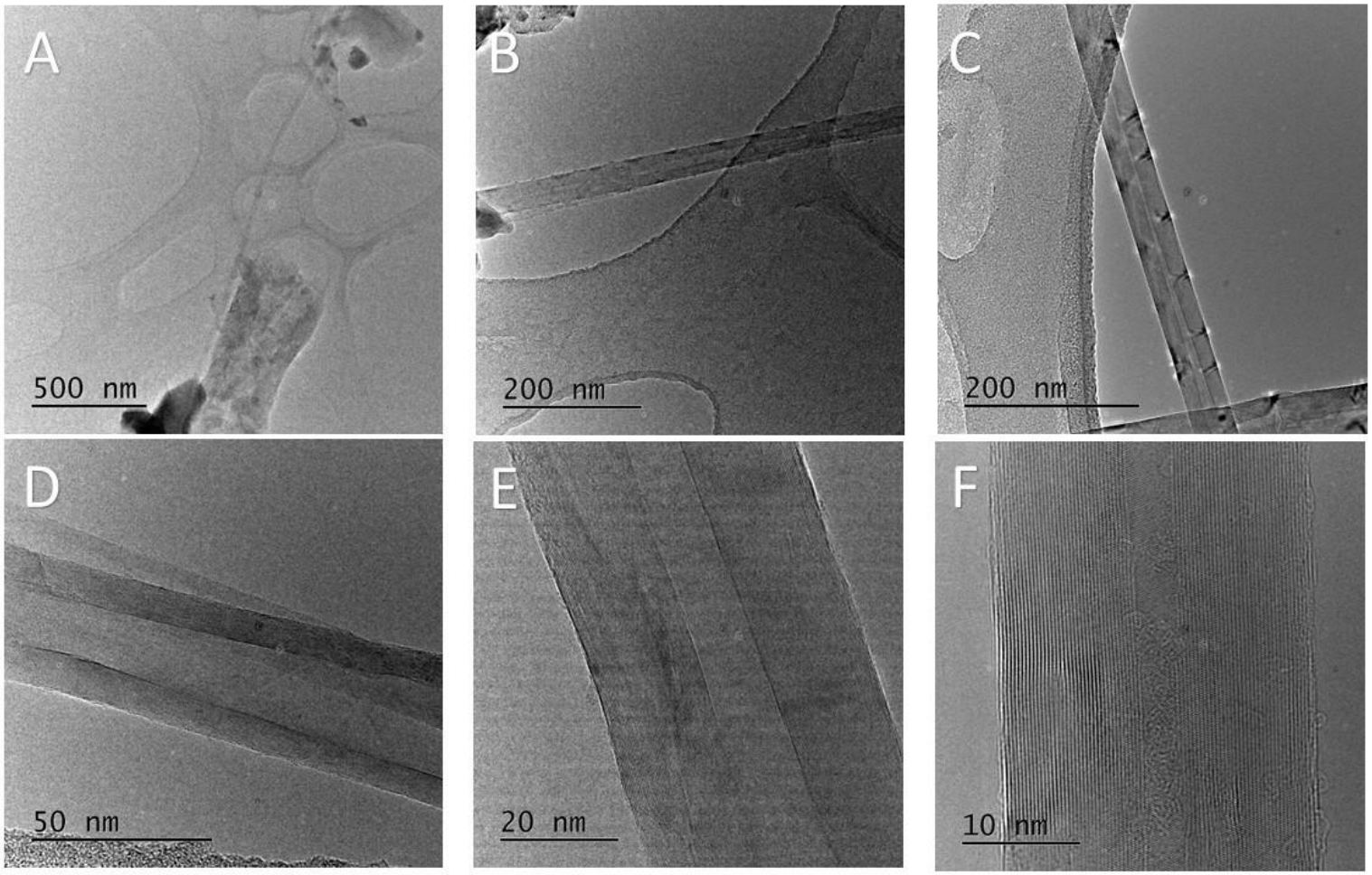

Figure 5. 7: A-B) TEM micrographs of the long straight tubes C) TEM micrograph of BNNTs, dark areas indicate the presence of facets. D) TEM micrograph of wall and center contrast differences E) Hollow center in the tubes F) HRTEM image of well crystalline wall structure of BNNT

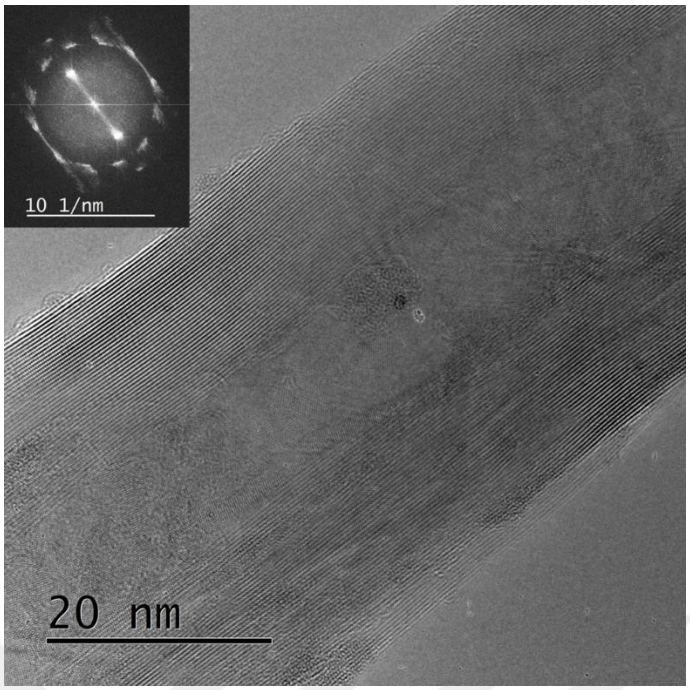

Figure 5. 8: The HR-TEM image of a typical BNNT. Inset shows the FFT of the same image

Enlarge image of the center of the tube (red area in Figure 5.9A) demonstrated hexagonal networks (arrangement) of the atoms in nanotube structure (Figure 5.9B). Inside of the tubes are empty, i.e., no sign of filling with catalytic particles or impurity.

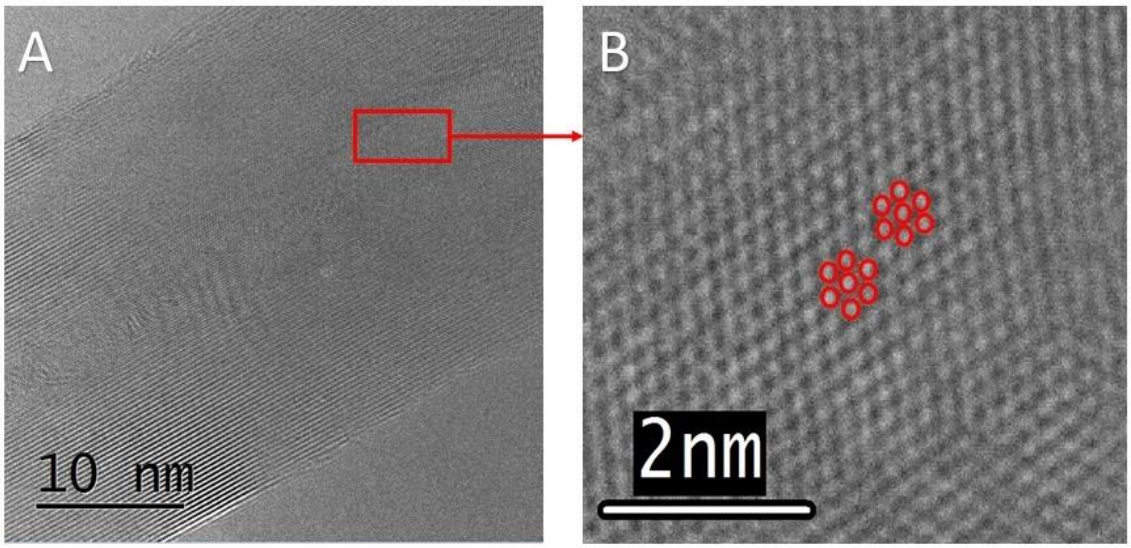

Figure 5. 9: A) HRTEM image of well crystalline wall structure of BNNT B) enlarge image of red rectangular at the center of the tube in A

High magnification image displayed well-ordered parallel walls with interlayer distance 0.323 nm in average which is similar to the characteristic distance of bulk h-BN (002) plane (Figure 5.10A-B). [44]

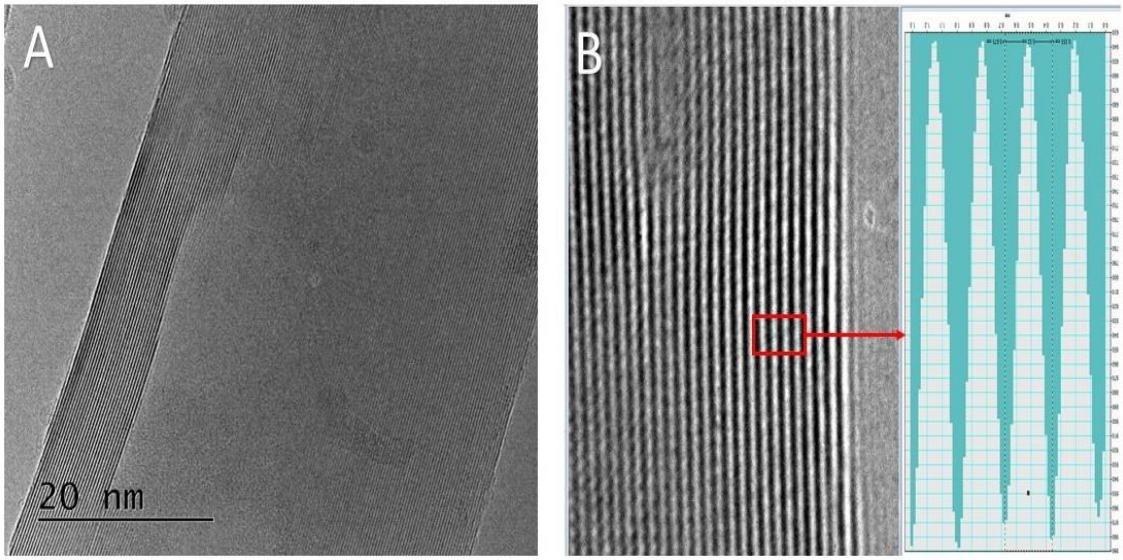

Figure 5. 10: A) Ordered fringes in the wall and B) interlayer distance measurement

Finally, electron energy loss spectrum (EELS) of the produced nanotubes show two ionization edges at 188 eV and 401 eV belongs to the B and N K-edges respectively (Figure 5.11).

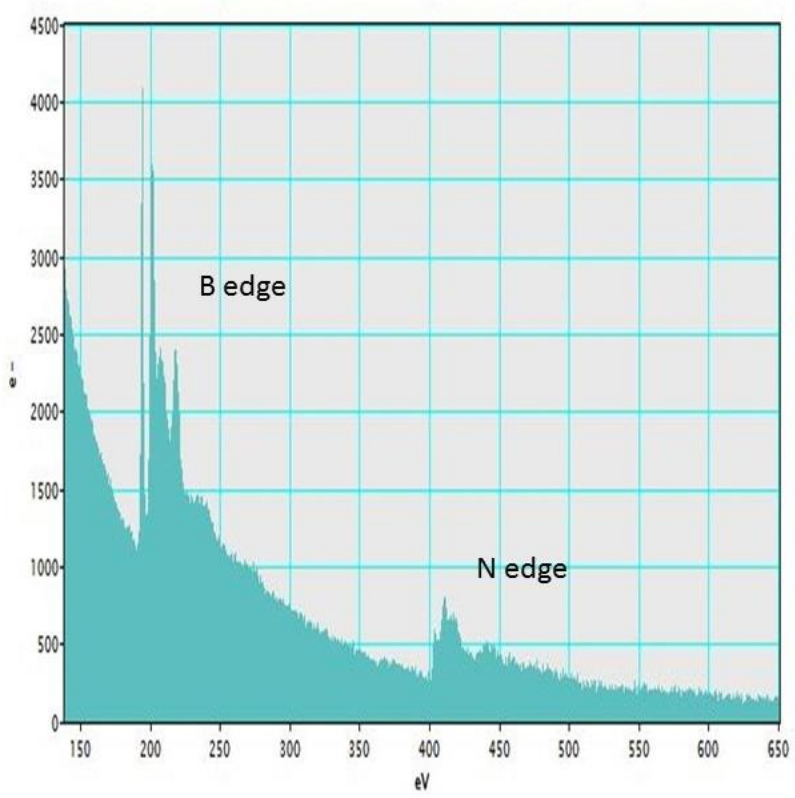

Figure 5. 11: EELS spectrum of BNNT synthesized at 800 °C.

5.4 Discussion

Microcrystalline structure and elemental analysis from TEM examination demonstrated that crystalline and good quality MW-BNNTs could be synthesized at 800°C by using $KFeO_2$ as a catalyst in presented study.

Given the success of $KFeO_2$ in TCVD, the effect of potassium as a new catalyst for the BNNT production should further be investigated in order to have a better understanding of the role of the catalyst in the growth process which presumably followed vapor-liquid-solid (VLS) mechanism similar to the most of the CVD studies.[22, 24, 25, 139]

5.4.1 VLS mechanism

In this mechanism, vaporized catalyst condenses on the substrate surface when its vapor pressure is sufficient enough. Then reactive gas species diffuse into the partially

condense catalyst aggregates until it is supersaturated with the solute. After that point, precipitation occurs and nanotube growth starts. Figure 5. 12A represent tip growth mode when the wetting of the catalyst droplet on the substrate is low. Figure 5.12B represent base growth mode at high wetting conditions when the interaction between the partially melted catalytic particle and the substrate is higher.

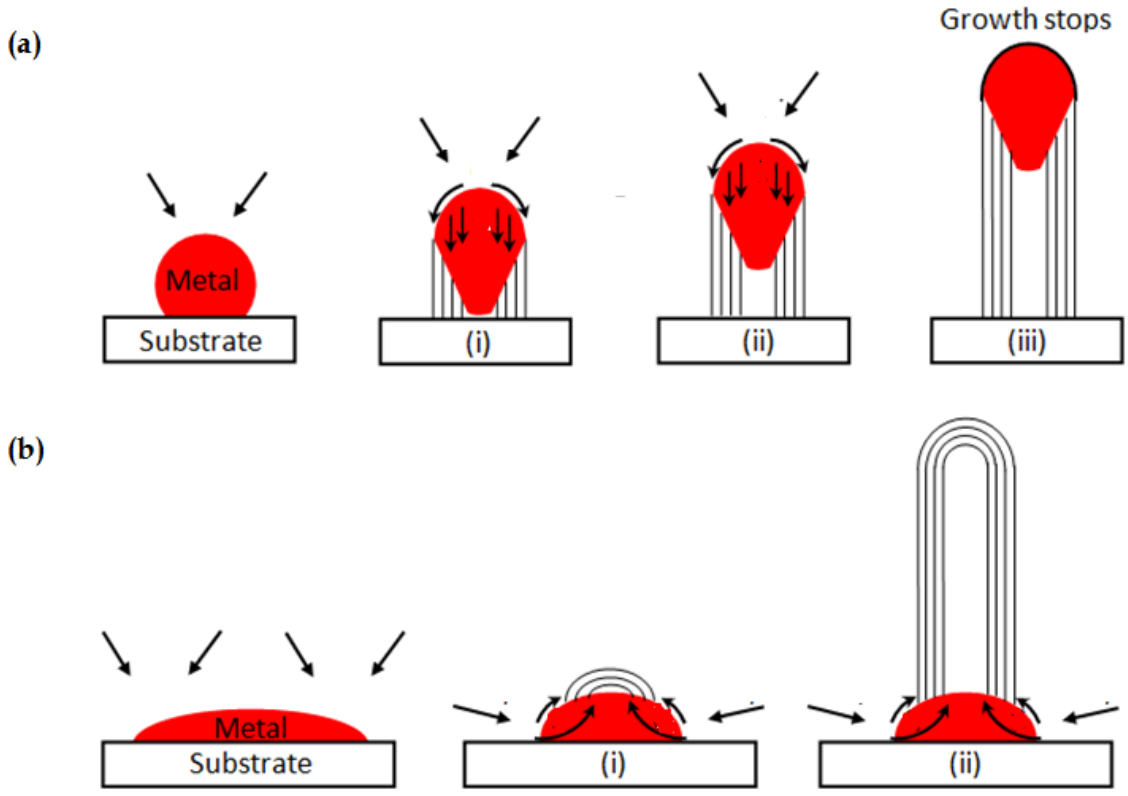

Figure 5. 12: A) Tip growth and B) Base growth modes in VLS mechanism

In this work, potassium species (K and K_2O) are anticipated to act as an active catalyst during the reaction. At 800 ^oC, desorbed potassium from the $KFeO_2$ is in the vapor state, and potassium vapor is trapped in the inner quartz tube. This vapor condenses on the porous surface of the combustion boat and the ceramic substrate when it reaches sufficient vapor pressure. Then, the BN species, formed by the reaction of B_2O_2 intermediate phase and NH_3, are dissolved in the potassium droplets, precipitate and grow into BN nanotubes after supersaturation (see Figure 5.13 for schematics).

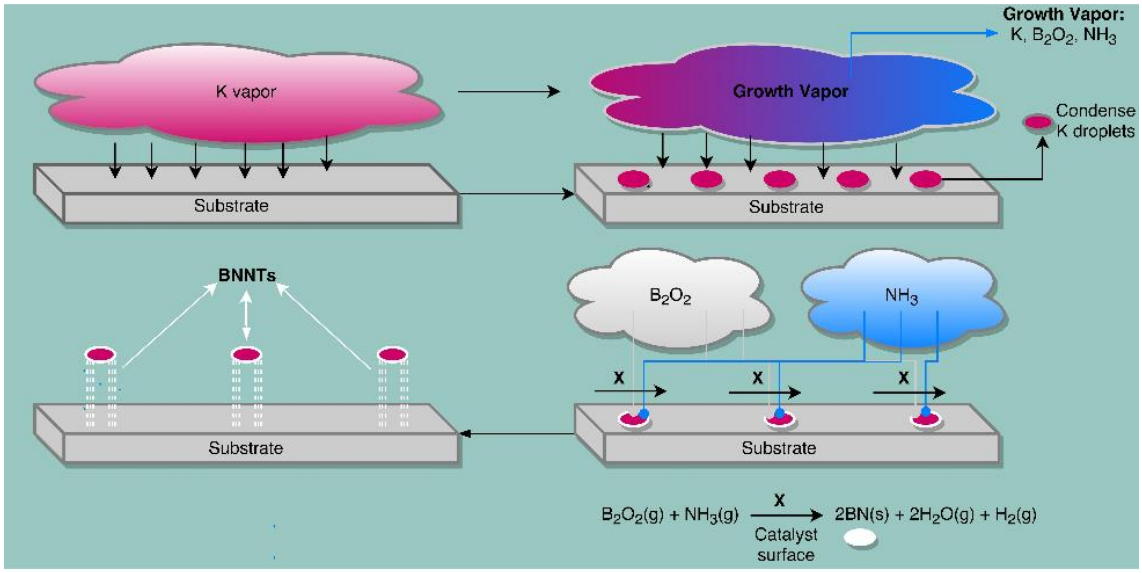

Figure 5. 13: Schematics of possible VLS mechanism in this study

5.4.2 Role of potassium: effect of temperature on BNNT growth

B_2O_2 in the growth vapor, which is considered as an effective intermediate phase to form BN, is arguably created by the reaction between boron and K_2O/ iron oxide species which are the decomposition by-products of $KFeO_2$ at high temperatures.[130] Therefore, to test the projected concept about the role of potassium as an active catalyst, three additional temperatures 700°C, 750°C (below and around potassium boiling point) and 1000°C (over potassium boiling point) were also chosen for BNNT synthesis with $KFeO_2$. At 700 °C, there was not significant BNNT growth on the combustion boat walls and the substrate. On the other hand, at 750 °C slightly lower than potassium's boiling point (Figure 5.14A), BNNT growth on the walls was achieved but not as efficient as at 800°C (Figure 5.14B). The anticipated limiting factor is potassium partial pressure in the growth vapor. Lack of potassium partial pressure results in two interrelated consequences. i) insufficient potassium catalyst condensation on the combustion boat walls and the ceramic substrate, ii) inefficient production of B_2O_2

intermediate in the growth vapor due to the low temperatures and low K_2O concentration. In this study, we anticipated BN formation proceeds from B_2O_2 intermediate phase, as in the case of MgO and Li_2O catalyst in the literature. Ellingham diagrams support this interpretation, suggesting that higher oxygen transfer tendency of the K_2O.[127] However, it is also possible that potassium boride compounds are formed. If these phases participate as an intermediate of BN formation, one can expect BNNTs in the powder due to the low partial pressure of potassium boride phases at 800 ^oC. Since we only observed BNNTs on the walls and the substrate, the gas phases B_2O_2 and K, were attributed as responsible phases for the BNNT formation. At 1000 ^oC, the yield of the nanotubes was higher than 800 ^oC as a result of higher potassium desorption and/or effective B_2O_2 creation at that temperature (Figure 5.14C). However, high potassium desorption from the $KFeO_2$ generated potassium flux which reduces the glass formation temperature of the silica-based combustion boat as such formed glass covered the top (surface) of the nanotubes. Therefore, we conclude that $KFeO_2$ catalyzed synthesis temperature higher than 800 ^oC may be restricted to the combustion boat composition (Figure 5.16).

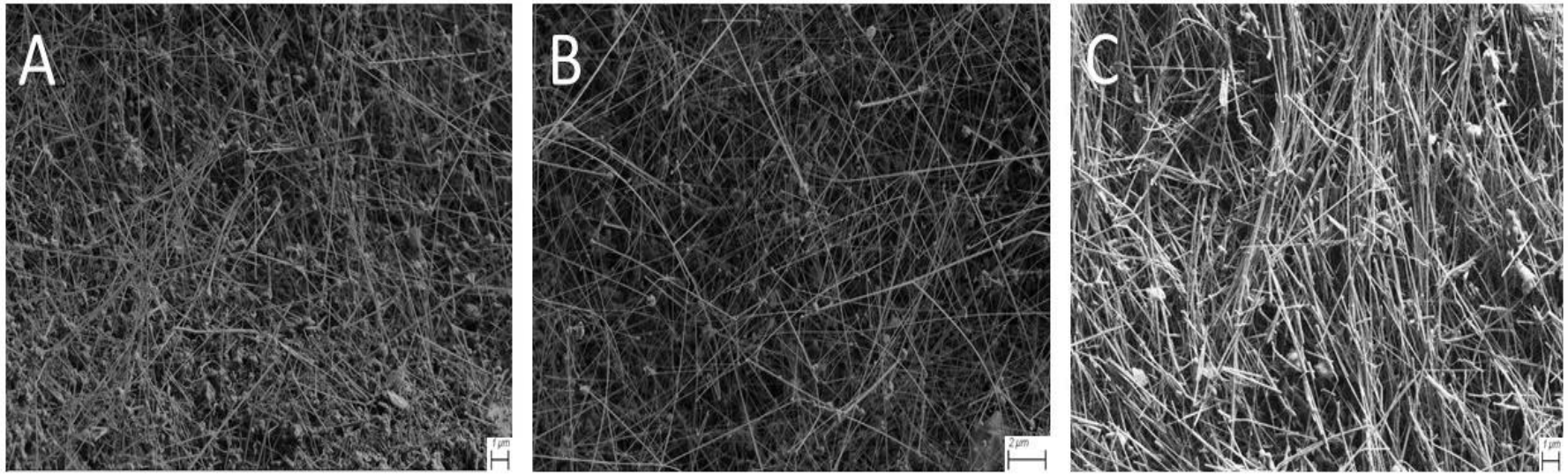

Figure 5. 14: SEM micrograph of BNNT coverage on the walls A) 750 ºC B) 800 ºC C) 1000 ºC

Morphologies of the as-received BNNTs of different temperatures were also compared by SEM. Produced BNNTs on the wall have an average diameter around 60± 22 nm (Figure 5.14A), 81± 38 nm (Figure 5.14B) and 80± 39 nm (Figure 5.14C) for 750 ^{o}C, 800 ^{o}C, and 1000 ^{o}C, respectively. Results show that before boiling point of potassium, small catalytic aggregates were formed due to the low partial pressure of potassium in the mixed growth vapors leading to smaller diameter tubes. On the other hand, beyond potassium boiling temperature, the higher partial pressure of the catalyst leads to the formation of catalytic metal atom aggregates into the larger cluster those results in BNNT growth in larger diameters. After 800 ^{o}C, size of the resulting BNNTs did not change due to the sufficient formation of catalytic metal vapors. Size of the catalytic aggregates may also depend on the porous surface. Ndlela et al. demonstrated that mass loss of $KFeO_2$ started after 700 ^{o}C in the existence of reducing gas and continued afterward (Figure 5.15A).[131] In addition, Kotarba et al. showed that potassium desorption from iron catalyst increases in the highly reducing atmosphere (H_2: N_2 (3:1)) due to the lower stability of potassium on the reduced iron surface (Figure 5.15B).[140] In the present case, there was always sufficient catalyst vapor after 800^{o}C due to the temperature and reducing atmosphere (NH_3) during BNNT formation.

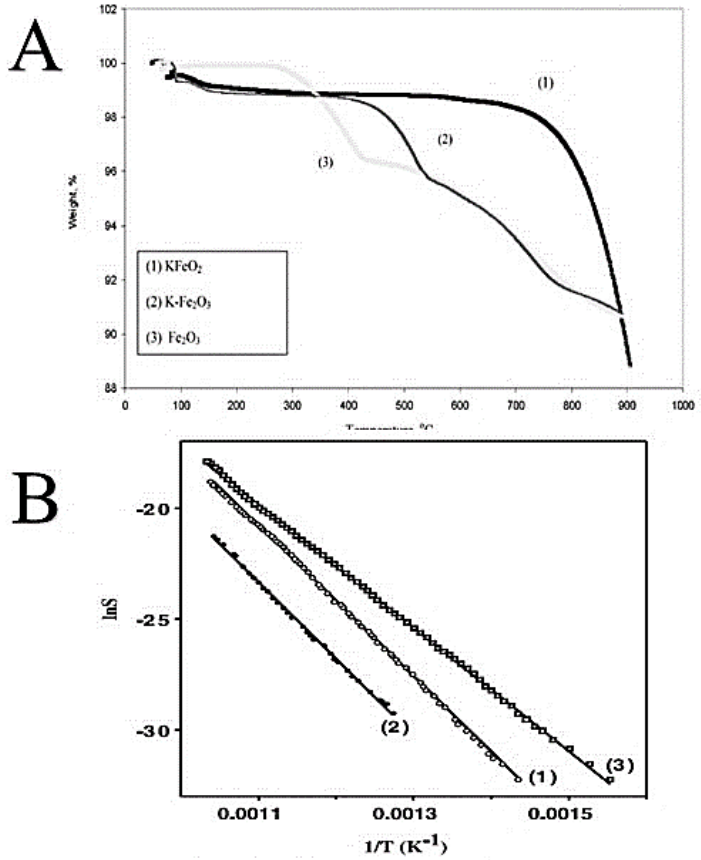

Figure 5. 15: A) KFeO2 mass loss at 5 torr hydrogen (adapted from reference 131) B) K desorption from iron catalyst at 10 bar H2: N2 (3:1) (adapted from reference 140)

5.4.3 Effect of porosity

To elaborate on the effect of combustion boat and substrate on the BNNT formation at 800 ^{o}C, sintered alumina combustion boat and a silicon wafer as substrate were also experimented. There weren't any BNNTs grown on the Si-wafer and the alumina walls. The reason why BNNT formation occurs in the porcelain combustion boat and substrate instead of sintered alumina and Si-wafer is attributed to the porous structure of the ceramic. Porous structure increase wetting of potassium on the surface and increase catalyst condensation inside the pores, which in turn enhances BNNT formation. Additionally, only combustion boat material did not initiate BNNT growth, since trials with Fe_2O_3 and nanoparticle MgO/Fe_2O_3 doubles used as a catalyst with boron powder

did not yield successful BNNT growth at 800 ^{o}C. Control experiments without $KFeO_2$ suggested that BNNT growth on the walls of the combustion boat and the substrate is not possible without potassium partial pressure in the growth vapor.

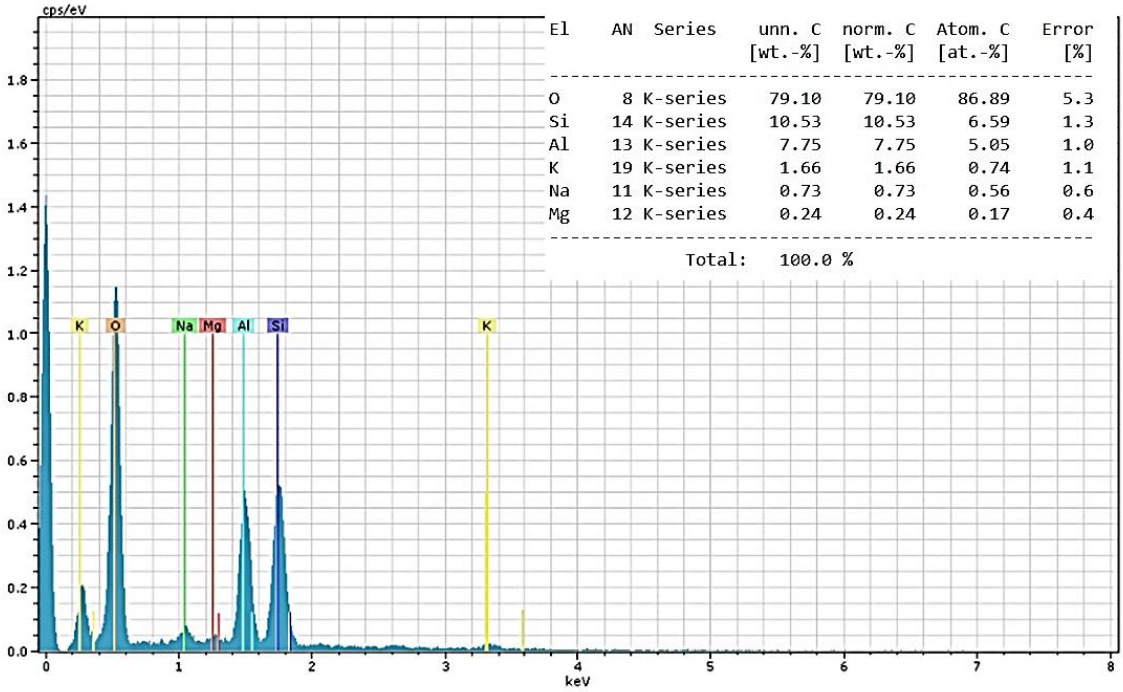

Figure 5. 16: EDS spectra of ceramic crucible

5.4.4 Growth Mode

As the nanotubes are examined in more detail, one can see that almost all nanotubes had a reasonably consistent morphology at the tips, which suggest the tip growth mechanism (Figure 5.17A). To elaborate further on the growth of the BNNTs, various tube tips were analyzed by energy dispersive X-Ray spectroscopy (EDS) attached to a TEM. Almost all the tips have particles, containing potassium of varying concentration. This also indicates the significance of potassium in the catalytic growth of BNNTs in this work. It is important to note that potassium at the tips can dissipate very quickly in time due to the reaction with moist air, which makes the detection challenging.

Measurements should be done quickly after synthesis. High Angle Annular Dark Field (HAADF) image displayed core shell structure: inside of the tip was at a stronger contrast than the outside due to the higher molecular weight of particles from surroundings (Figure 5.17B). The encapsulated particle was further investigated by energy dispersive X-ray spectroscopy (EDS). Elemental EDS maps of K, O, and N were shown in Figure 5.17 C-E. Potassium and oxygen species were aggregated in the core and surrounding mainly composed of nitrogen. Nitrogen encapsulated catalytic particle can be observed very clearly when all of the elements are put together which indicates that tip growth mechanism of the BNNTs produced in the presented study (Figure 5.17F). Aside from potassium, some of the tips contain also silicon, aluminum, and sodium, which are probably originated from a combustion boat and trace amount of iron. In addition, calcium was detected in some of the tips, however, neither combustion boat nor precursors contain calcium, therefore, we assume that Ca was originated due to dust from the environment.

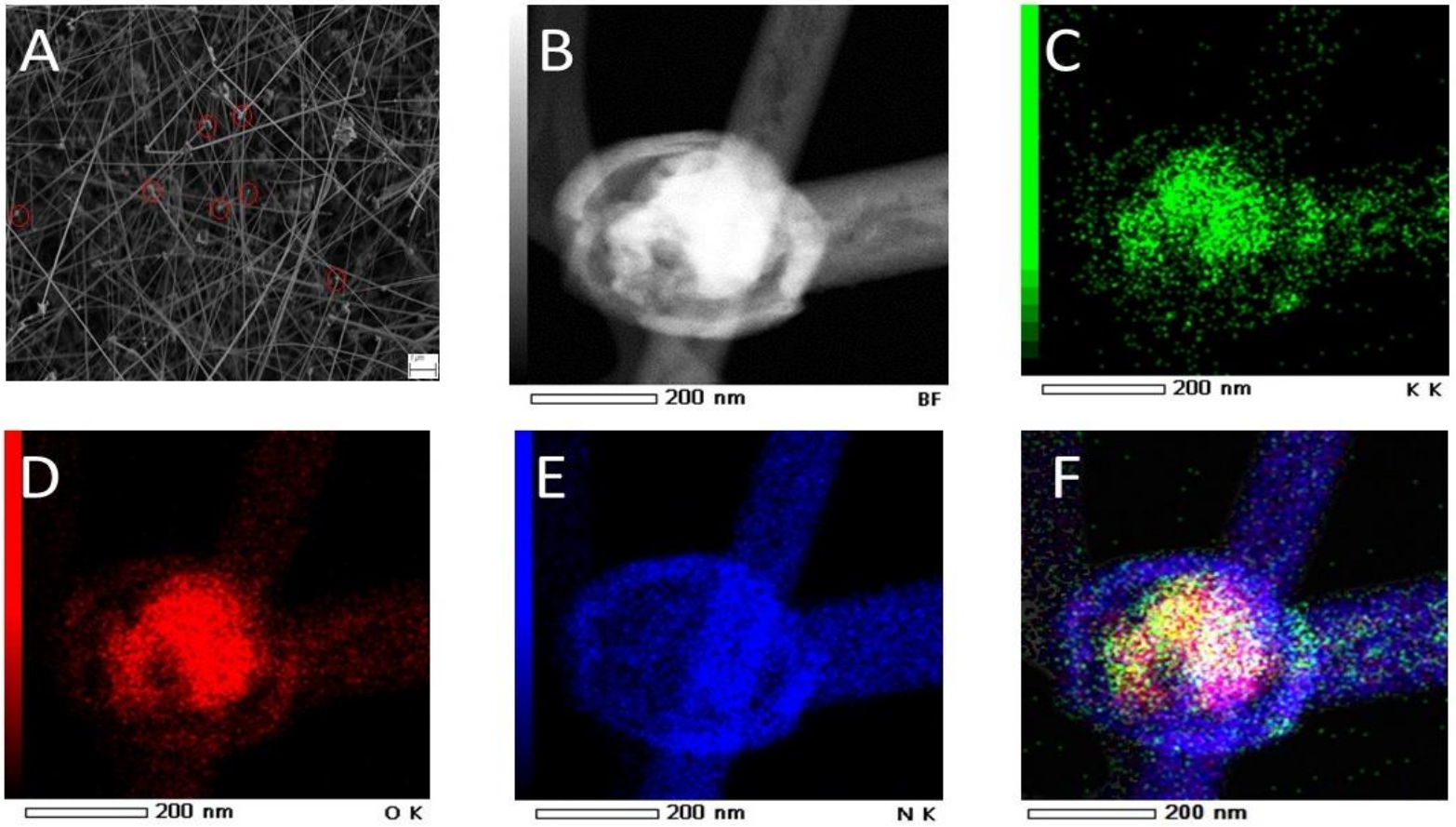

Figure 5. 17: A) SEM image of nanotube tips (red circles) B) HAADF micrograph of nanotube tip, EDS map of C) potassium D) oxygen E) nitrogen F) overlay image of three elements (Core shell structure)

5.5 Conclusion

In summary, we demonstrated that high quality, long and straight MWBNNTs can be produced on the ceramic substrate efficiently at low temperatures by using $KFeO_2$ as the parent material for catalyst in TCVD method. Although optimum temperature for our system was 800 ^oC, BNNTs can be grown after 750 ^oC. The success of the BNNT production via this approach is due to the combination of efficient potassium desorption from the $KFeO_2$ parent material, creation of reactive boron intermediates from potassium and iron oxide species, and nevertheless porous structure of the ceramic substrate. TEM results demonstrated encapsulated catalytic particles in the core of the tips. This behavior suggested that tip growth mechanism is dominant in the synthesized BNNTs. The output of this study is significant that high quality BNNTs could be produced on the porous substrates that are sensitive to high temperatures by using $KFeO_2$ with readily available tube furnace.

CHAPTER 6

6 ALKALI METAL FERRITES CATALYST SYSTEMS for BNNT SYNTHESIS

6.1 Summary

After successful experiments with $KFeO_2$, the effect of other alkali metal ferrites on the BNNT production at desired temperatures was investigated. Results were presented in this chapter. Due to the primary motivation for reducing BNNT growth temperatures by new catalysts, we first used Cesium ferrite ($CsFeO_2$) instead of $KFeO_2$ since it has the highest vapor pressure compared to the other alkali metals. However, trials with Cs did not result in any successful BNNT growth. The reason may be the low synthesis temperatures with Cs did not lead to BN crystallization, or maybe the large atomic radius of Cs prevents BN formation. Sodium ferrite ($NaFeO_2$) on the other hand, successfully lead to BNNT formation at temperatures where the metallic sodium boiling point was, same as $KFeO_2$. Li was already used as a precursor in BNNT synthesis in the form of Li_2O over 1350 ℃, BNNTs were only synthesized over 1100 ^oC due to the low vapor pressure of lithium compared to the alkali metals. Results presented in this chapter showed that BNNT formation temperatures and morphologies change depending on alkali metal type in the ferrite structures.

6.2 Objectives

The objective of this chapter is to understand the role of alkali metal type in the BNNT formation. In the previous chapter, $KFeO_2$ was used as a catalyst to reduce BNNT growth temperature. Suggested mechanism was based on the VLS method where potassium was crucial for nanotube growth. BNNT growth was only achieved on the substrate around or over the boiling point of alkali metal. To investigate projected

concept, other alkali metal ferrites ($CsFeO_2$, $NaFeO_2$, and $LiFeO_2$) were used in the BNNT growth process. Growth temperatures were chosen to be below and above the boiling point of the alkali metal used in their ferrite forms. Thus, the effect of alkali metal on the BN crystallization could be investigated. If different alkali metals induced the BNNT formation at their boiling temperatures, we can conclude that alkali metals have a promotion effect on BN crystallization. In this way, their catalytic effect on nanotube growth was proven according to the result of this chapter.

6.3 $CsFeO_2$ for BNNT synthesis

Cs is the first candidate after potassium within the alkali metals due to its high vapor pressure. The boiling point of the metallic cesium is 670 ^oC, which can easily evaporate and condense on the substrate to start to nucleation point for the reactive species. However, compared to the effective catalysts like Mg and Li in BNNT synthesis, its elemental properties differ prominently from them, such as its atomic radius almost three times higher. More electropositive than any alkali metal, it reacts vigorously with water. On the other hand, its oxide form finds itself in catalytic applications such as side chain alkylation of toluene, epoxidation of propylene-to-propylene oxide, partial oxidation of p-methoxy toluene due its basic properties.[141-143] Due to its high basicity Cs_2O is an effective side chain alkylation catalyst from toluene and methanol to styrene and ethylbenzene and in the oxidation of p-methoxy toluene to p-methoxy benzaldehyde process, it was showed moderate catalytic activity but higher selectivity compared to the less basic oxides such as Li_2O and MgO. Additionally, Cs have been widely studied in hydrogen production from ammonia as promoter in Ruthenium catalyst.[144-146] Despite the reversibility of the potassium promoted iron catalyst system for ammonia decomposition at relatively high temperatures, ruthenium catalyst gave the best decomposition rate at low temperatures and highly basic supports enhance the

recombinative desorption of nitrogen atoms. Promoters increase the effectiveness of the catalyst by interaction with the reactants and the support to electronically modifying active sites of the catalyst, which enable recombinative nitrogen desorption. Promoter efficiency increase with its basicity, therefore, Cs gives the best result with ruthenium at low temperatures for ammonia decomposition (below 400 ^{o}C). Considering the higher efficiency of the Cs for ammonia decomposition at low temperatures, and promotion effect of crystallization of alkali metals at BN formation like in $KFeO_2$ case, we believed that $CsFeO_2$ could be a good candidate apart from potassium. For this reason, $CsFeO_2$ was synthesized through the organic precursor method as explained in details in chapter 3.4. $CsFeO_2$ was used in dehydrogenation reactions and believed to be an active phase like $KFeO_2$.[147, 148] It is a hygroscopic compound, react with moist air readily faster than $KFeO_2$ for this reason after vacuum quench stored in the glovebox. X-Ray diffraction analysis of the as synthesized $CsFeO_2$ were presented in Figure 6.1.

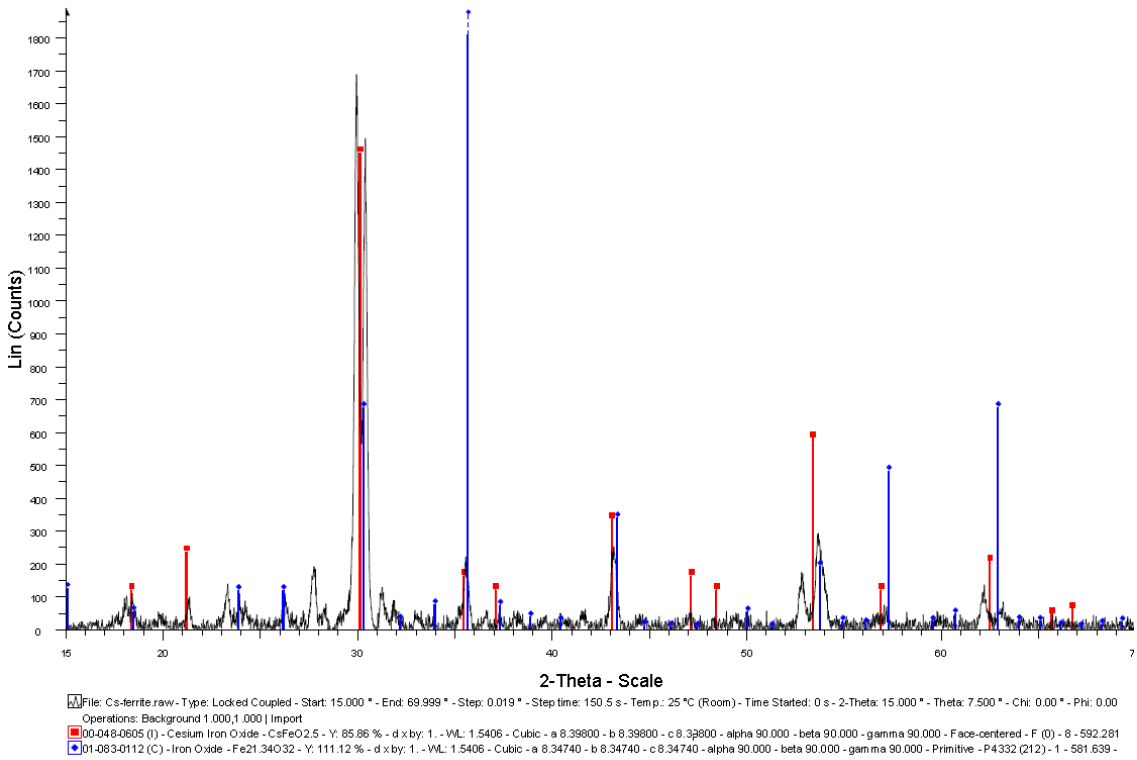

Figure 6. 1: X-Ray diffraction of $CsFeO_2$

Room temperature phase of $CsFeO_2$ is orthorhombic. However, x-ray analysis show that cesium ferrite has the high temperature FCC phase which could be the result of the quenching or different starting materials. Because for other alkali metal ferrites, researcher reported that different precursor effect final crytal structure of the product. [149] We have also detect cubic iron oxide phase in the structure.

BNNT growth with $CsFeO_2$ was conducted as explained in the chapter 3.3.2 same as $KFeO_2$. However, maximum temperatures were chosen according to the Cs boiling point. At 650 ^oC, which is below Cs's boiling point, there was no observable BN formation in the combustion boat. At 700 ^oC, over Cs boiling point, due to the Cs boiling, precursors were boiled over from combustion boat. Still, there was no sign of BN growth with $CsFeO_2$. According to the literature, $CsFeO_2$ is very unstable due to the large size of the Ce^+ in the crystal structure; there is a very high strain in the structure. Therefore polyferrite Cs-$\beta''Fe_2O_3$ is much favorable in the reductive environment.[147] Maybe for this reason, when we increase the temperature, metallic Cs boiled very severely and resulted in an overflow in the combustion boat. Also, unlike in potassium ferrite case, desorption from the structure was probably in the form of only metallic Cs, not in the Cs_2O. In the $KFeO_2$ case for BNNT growth, B_2O_2 intermediate phase is arguably produced from the reaction between potassium oxide/iron oxide and boron powder. One reason for the unsuccessful BNNT formation could be the lack of alkaline oxide in the growth vapor, which reacted with boron powder to form B_2O_2 and the other one is the simple the low temperatures, which prevent B_2O_2 creation from iron oxide and BN formation. Therefore, low temperature and the lack of reactive gas species for BN formation result in failed BNNT growth with the $CsFeO_2$ system.

6.4 $NaFeO_2$ for BNNT synthesis

Sodium is another alternative alkali metal apart from Cesium. However, its vapor pressure is lower than K and Cs, which cause higher temperatures for sodium desorption from the parent ferrite compound. On the other hand, sodium is very close the working catalyst systems Mg and Li in the periodic table, most of the properties are similar to each other, which make sodium is a good candidate as for achieving higher yields at relatively low temperatures around Na boiling point (883 ^oC). Like other alkali metals, sodium metal reacts vigorously with water. Its oxide form is also hygroscopic and unstable at the atmospheric conditions; moreover, it reacts with CO_2 in the air to form carbonate. However, its reactivity lower than potassium.

Sodium compounds were used in many catalytic processes, especially in organic synthesis.[150-152] One of the most common application is the base-catalyzed transesterification reactions for biodiesel production in the form of NaOH or sodium methoxide ($NaOCH_3$).[153] Na_2O on the other hand, is used in the dehydrogenation reactions such as ethylbenzene to styrene as an additive in Al_2O_3 like a $K_2O+Fe_2O_3$ commercial catalyst.[154] Also, Na based catalyst ($Na_2CO_3/\gamma\text{-}Al_2O_3$) was used as a catalyst for the conversion of biomass to bio-oil in pyrolysis, which reduces the oxygen content of the resulting oil and increases energy density.[155] According to the authors, higher activity was the result of the sodium species that form during the reaction. They found out that Na_2CO_3 decomposes after 500 ^oC with the Al_2O_3 support to Na_2O and CO_2. As explained in the previous examples, Na or Na_2O species are not directly used as a catalyst due to the unstable nature of the compound. Therefore, we used $NaFeO_2$ as a replacement for conventional MgO/FeO double, similar to $KFeO_2$ in chapter 5. $NaFeO_2$ is generally used in the literature as one of the cathode active material candidates for sodium-ion batteries due to its layered rock-salt crystal structure.[156, 157]

There was a limited number of studies those could use $NaFeO_2$ as a catalyst. It is mostly used in the NOx reduction processes.[158] Also, Na addition of the Pt/FeO_x catalyst increase catalytic efficiency of the hydrogenation of nitroarenes due to the formation of NaFeO2 surface layer which increase Pt dispersion and selective adsorption of nitro groups. [159]

In this study, $NaFeO_2$ was used as a parent material for BNNT growth, where sodium and sodium oxide desorption enable the BN crystallization. Crystal structure of the $NaFeO_2$ is essential for the battery application, but in our case, it is not important, we used as a catalyst (source of sodium), so we tried to decompose the structure to release sodium. Many studies about synthesis of $NaFeO_2$ were published with different starting materials at different temperatures, which result in different crystal structure with the nature of the precursors.[160-162] However we synthesized $NaFeO_2$ with organic precursor method like other ferrites in chapter 3.4. Phase analysis with the XRD in Figure 6.2 reveals that with our method, two distinguished phases of $NaFeO_2$ is formed at 700 ^oC. Rhombohedral α-$NaFeO_2$ with the R(O) space group (File database pdf 00-020-1115) in which sodium and iron ions occupied octahedral sites and orthorhombic β-$NaFeO_2$ with the space group Pn21a (File database pdf 04-007-8130) where iron and sodium placed tetrahedral sites exist together at 700 ^oC. The phase transition from α-$NaFeO_2$ to β-$NaFeO_2$ is reported over 760 ^oC. $NaFeO_2$ is more stable in the air than the K and Cs ferrites. However, it is still hygroscopic therefore, it is stored in the glovebox for further usage.

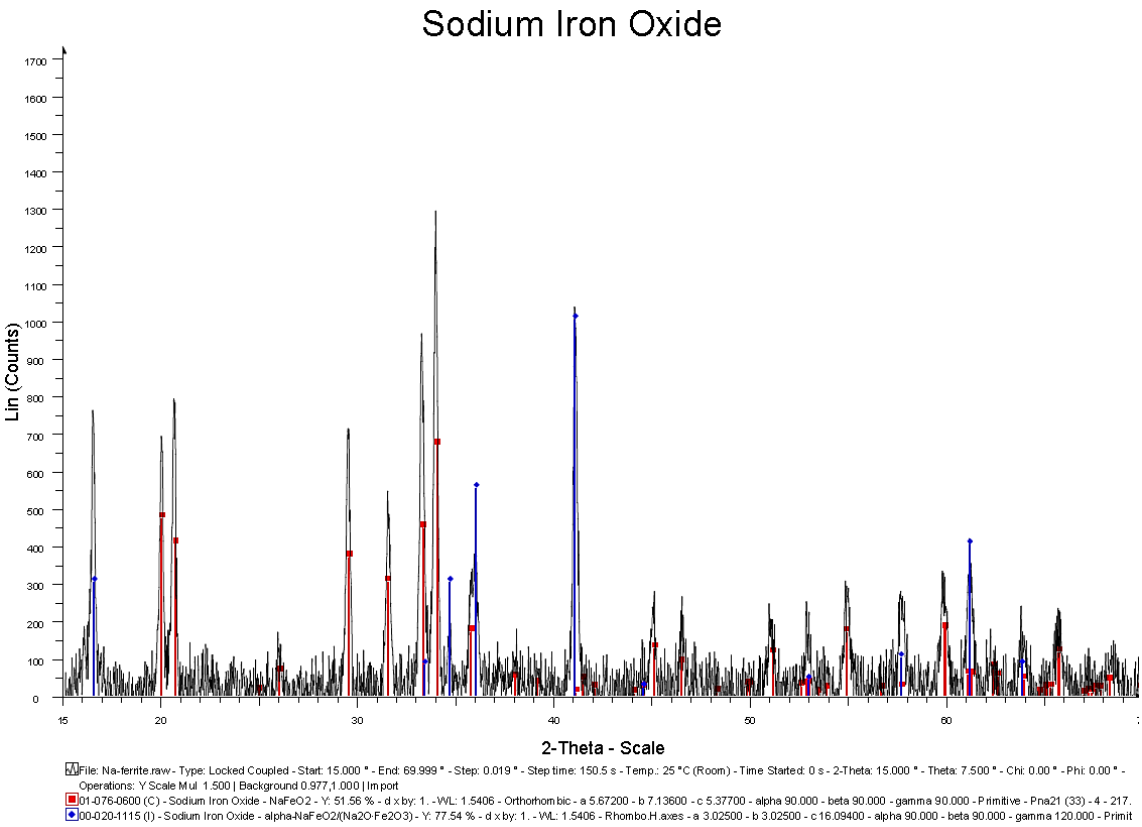

Figure 6. 2: Powder X-ray pattern of $NaFeO_2$ (β-$NaFeO_2$ (red), α-$NaFeO_2$ (blue))

6.4.1 BNNTs synthesis with $NaFeO_2$

BNNTs were synthesis with the TCVD with GVT approach like $KFeO_2$. Amorphous boron and as-synthesized $NaFeO_2$ were mixed in the ceramic combustion boat, placed in the inner quartz tube, and sealed inside the glovebox. After placing in the furnace tube was opened under argon then experiment was conducted according to the chapter 3.3.2. Two different synthesis temperatures were chosen according to the boiling point of sodium (below boiling point (800 ^oC) and above boiling point (900 ^oC). After the BNNT production, white coating of the combustion boat and the substrate were observed (Fig. 6.3).

Figure 6. 3. BNNT production at 900 ^{o}C with $NaFeO_2$

At 800 ^{o}C, there was very few visible white region around the precursor powders, however, at 900 ^{o}C, yield was much high and whole combustion boat and the substrate covered with white BN coating. Different from $KFeO_2$ synthesis, with $NaFeO_2$, BN growth was achieved on the Si-substrate and some observable white powder on the top of the precursor powders for those we could not observe with $KFeO_2$.

6.4.1.1 BNNTs on the walls

White coating on the wall of combustion boat were analyzed. At 800 ^{o}C, there wasn't any observable BNNT growth with $NaFeO_2$. Therefore, results presented here all belong to the BNNT growth at 900 ^{o}C. Samples were analyzed without any further treatment like sonication or chemical purification. SEM analysis directly investigated from the boat wall revealed dramatic differences in the morphology of the BNNTs, which form by using $NaFeO_2$, compared to the $KFeO_2$ (Figure 6.4). Large spatial coverage can be

observed at Fig. 6.4A, whole combustion boat was covered with the BN structures. Long nanotubes over 30 micron and short microstructures (over 500 nm in diameter) with 5-6 ηm length were observed together (Figure 6.4B). Long curly nanotubes with large diameters between 100 nm and 200 nm were mixed with straight thin nanotubes with diameters below 50 nm (Figure 6.4C). Mixed morphology of the BNNTs can be observed in more detaile at high magnification image (Figure 6.4D). Compared to the BNNTs synthesized with $KFeO_2$, which entirely form of straight nanotube morphology, with $NaFeO_2$ mixed morphology thick curly and thin straight nanotubes were observed together and yield was comparably higher with $NaFeO_2$.

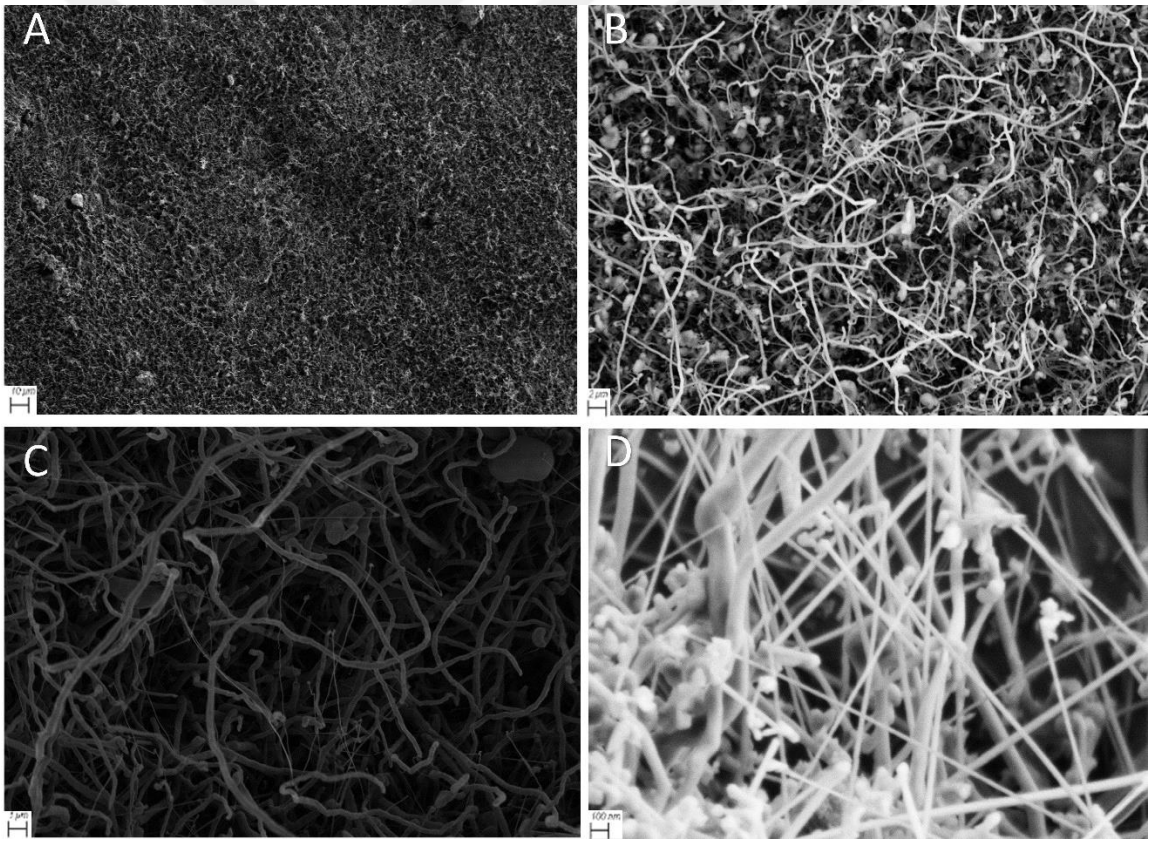

Figure 6. 4: SEM micrograph of BNNTs with $NaFeO_2$ at 900 ^oC. A) Large area coverage B) Mixed morphology of the tubes C) Long and curvy nanotubes

Sample preparation for TEM analysis was carried out by scratching the white sample on the walls of the crucible onto the copper grid. HRTEM images of the BNNTs with different morphologies were shown in figure 6.5. Figure 6.5A corresponds to HRTEM

image of the thin long and straight nanotube with diameter around 40 nm. Periodic black regions on both side of the wall characteristic for BN nanotubes, which can be seen more easily in figure 6.5B. Well crystalline wall structure can be observed with the absence of any defects. Interplanar spacing of 0.328 nm was measured with averaging ten consecutive layers on the walls, which is well correlated with the bulk h-BN interplanar distance, 0.33 nm (Figure 6.5C). Example of the thick curly tube was observed at Figure 6.5D which is also called curled BN fibers by some authors in the literature.[163] TEM analysis revealed that the BNNTs that are long, well-crystalline, straight ones are thinner in diameter and showed almost uniform wall thickness around 15 nm. Curly ones were bigger in diameter and polycrystalline.

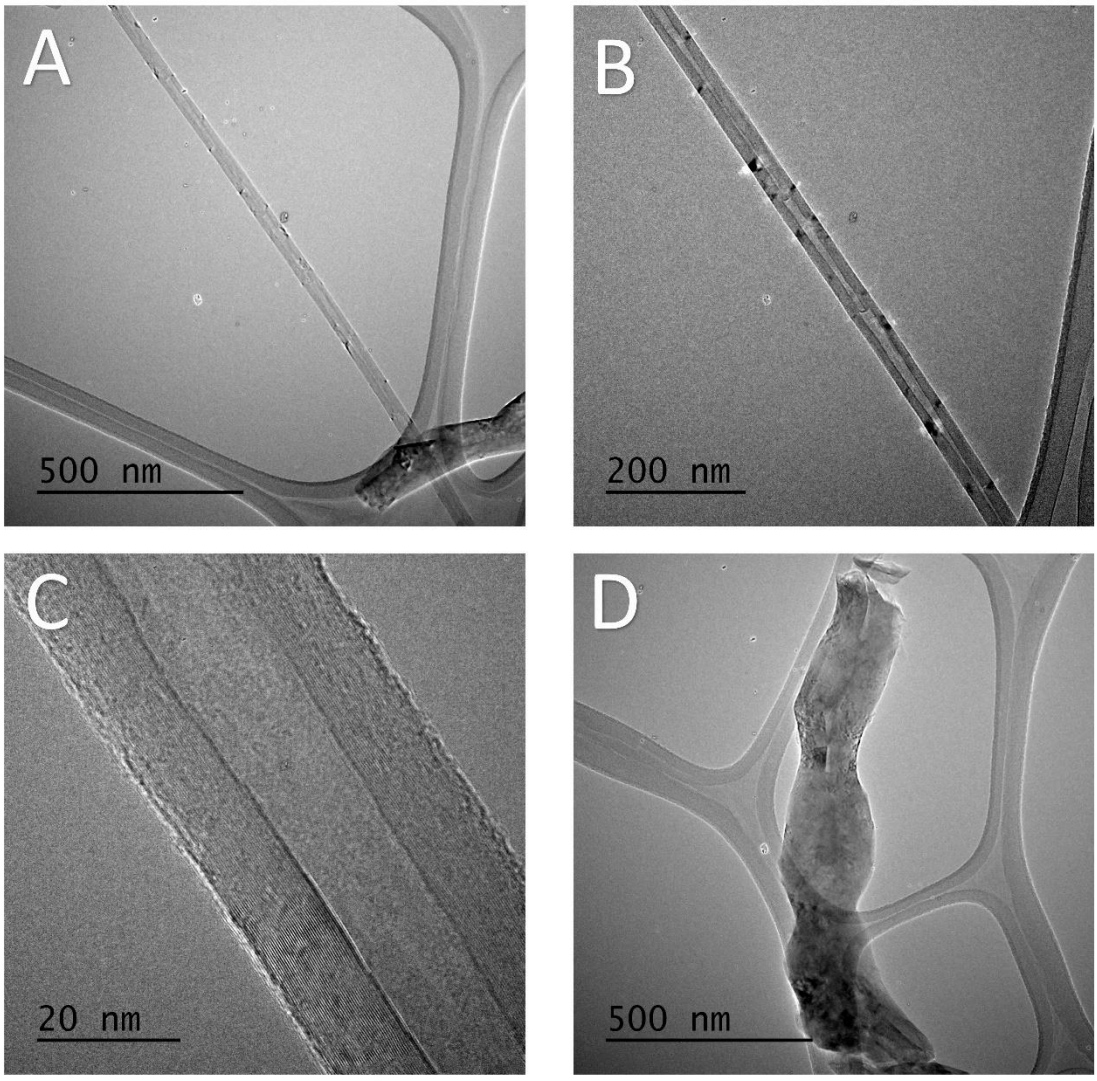

Figure 6. 5: TEM analysis of BNNT A) HRTEM image of thin straight individual tube B)Periodic dark regions across the tube walls C) Well crystalline tube walls D) HRTEM image of thick curly morphology

The chemical composition of the BNNTs was investigated by EELS measurements. Figure 6.6 showed corresponding EELS spectrum of the BNNTs with boron (Fig.6.6A) and nitrogen (Fig. 6.6B) edge showed separately. Boron K-edge at 188 eV and nitrogen K-edge at 401 eV can be observed very clearly. Sharp π* profile indicates hexagonal sp^2 bonding of BN without any carbon impurities at 285 eV. As-grown nanotubes were characterized also by Raman Spectroscopy. Typical Raman spectrum of the BNNTs was shown in figure 6.6C. The sharp peak at 1362 cm^{-1} corresponds to the high-frequency in-plane counterphase vibration of the B-N bond (E_{2g} mode). For bulk, highly crystalline h-BN particles this peak was reported to be at 1365 cm^{-1}.[134] Redshift of the

peak was observed in the spectra. However, our BNNTs are multiwalled, therefore, it should be very similar to the crystalline bulk h-BN. Downshift and broadening in the spectrum was explained by Arenal et al. with the local temperature increase by the laser (anharmonic effects), unrelated to the nanotube response.[134]

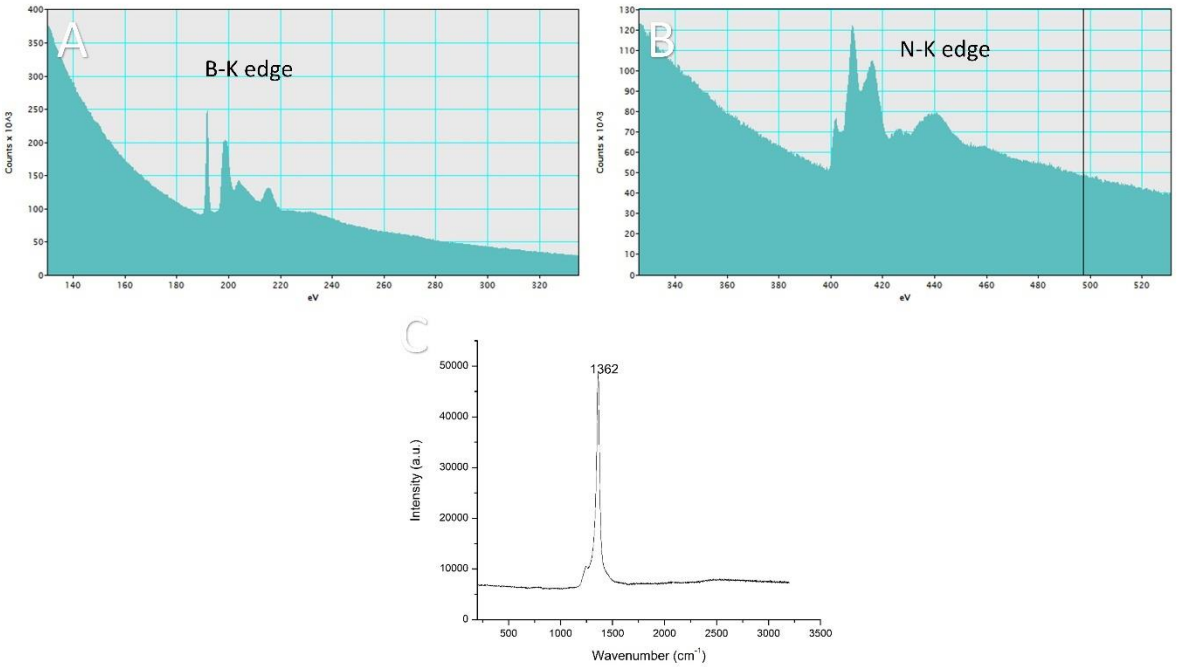

Figure 6. 6: Typical EEL spectrum of BN A) Boron K-edge B) Nitrogen K-edge C) Raman spectrum of BN

BNNT growth by $NaFeO_2$ at 900 ^oC was supported to the idea of alkali metal-based catalyst presented for $KFeO_2$. We were able to grow BNNTs at 800 ^oC with good coverage by $KFeO_2$. On the other hand, with $NaFeO_2$, there is only small amount of BNNTs on the top of the powders at 800 ^oC below Na's boiling point. However, when we increase the temperature at 900 ^oC, above Na boiling point, considerable amount of BNNTs were successfully grown by using $NaFeO_2$. Results suggest that low temperature growth of the BNNTs were not possible without alkali metal in the growth vapor.

There is also very drastic change in the morphology of the BNNTs growth with Na and K. With Na, mixed curly and straight nanotubes were grown together. Like K case in section 5, VLS mechanism was suggested for Na case, due to the vapor phase grew of nanotubes. There are two possible mechanisms for VLS growth, tip and base also called root growth as explained in section 5.4.1. In this mechanism, as a result of the reaction of boron with desorbed Na_2O and iron oxide species from $NaFeO_2$, intermediate phase B_2O_2 was formed. Growth vapor NH_3, B_2O_2 gas phase, and catalyst vapor lead to BN formations. When vapor pressure is high enough, catalyst species are condensed into partially melted particles and formed BN species dissolved into the catalytic metal droplets, which lead to the supersaturation and growth of the nanotubes. In our case, the temperature was low enough, only Na could evaporate and condense on the combustion boat and the substrate compared to Fe, which has a low vapor pressure at 900 ^oC. If catalytic particles are present on the tip of the nanotube, tip growth mechanism is favorable. However, we could not observe any particle in the tips unlike $KFeO_2$ case; we can assume that growth BNNTs with $NaFeO_2$ follow base (root) growth mechanism. In this mechanism, after nucleation, BN, B, and N species are incorporating the growth from the base of the nanotubes. Then, nanotube started to grow and lifted from nucleation site.

For curly structures, growth mechanism should also be VLS mechanism, since condensation of the catalytic particles is necessary to grow nanotubes on the wall of the combustion boat from their vapor species. However, curly nanotube growth could be a little different from regular VLS growth. High interactions between catalytic particles and the surface of the substrate may result in reactions that lead to higher wetting and large catalytic droplets. Larger droplets lead to lesser catalytic particle distribution that results in more place to grow for BNNTs in a curly fashion. Additionally, during

precipitation of growth species, fluctuations occur due to the large area of the catalytic droplets and nonuniform stress that arouse between particle tube interface during simultaneous BN crystal growth, which result in BNNT bending.[27, 163]

6.4.1.2 BN structures in the powder and Si substrates

Another huge difference between BNNT growths with $NaFeO_2$ apart from $KFeO_2$ is the growth of BN structures at the powder and Si-substrate. White coverage on the Si-substrate was investigated with SEM (Figure 6.7). Extensive coverage of the substrate can be observed in Figure 6.7A. Long structures over 100 ηm and diameter up to 5ηm were shown in figure 6.7B, and some the structures were broken. Nevertheless, most of the wafer was mostly covered with short structures (around 5 to10 ηm Fig.6.7C). Most of the tube-like structures, which we call microtubes by now, are empty (Fig. 6.7D).

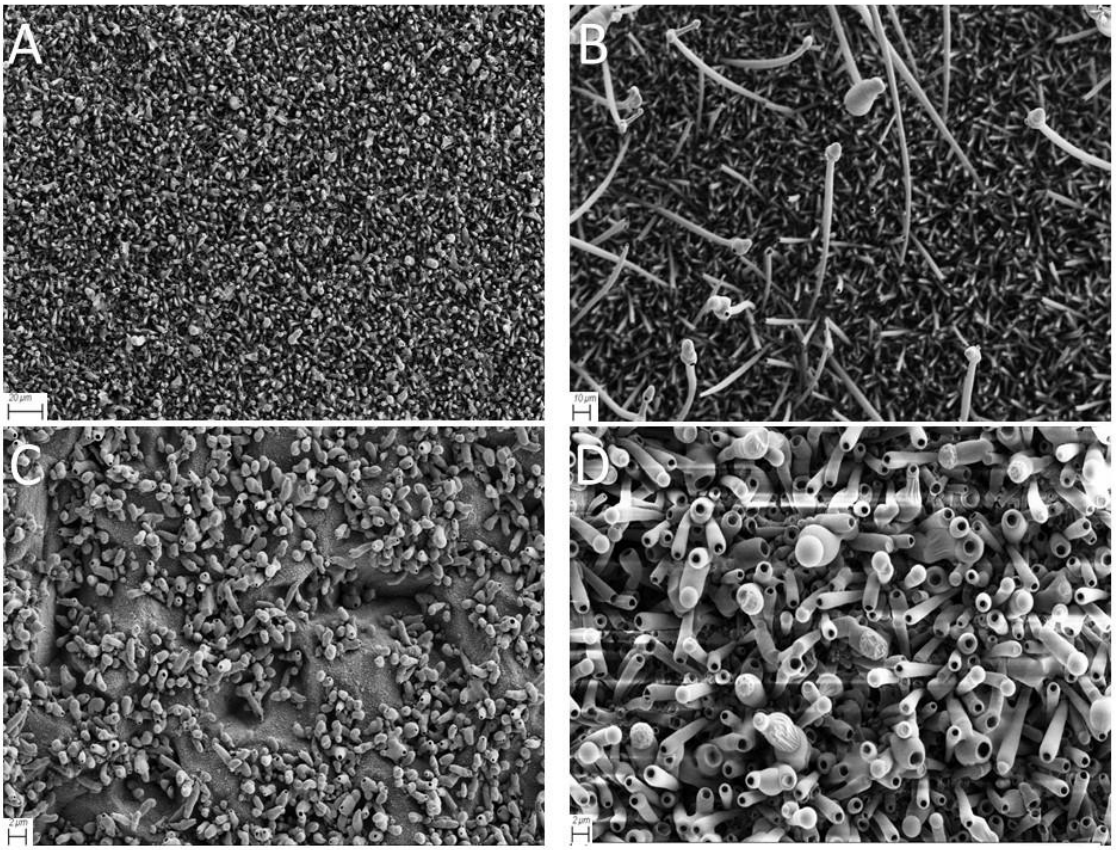

Figure 6. 7: SEM analysis of Si-substrate A) Large area coverage B) Long microtubes C) short microtubes D) empty structures

Quick Raman spectroscopy analysis of Si-substrate revealed the typical E_2g mode of h-BN at 1365 cm^{-1}(Figure 6.8). Peak position for the BN structures is the same as crystalline BN particles due to the large size of the microtubes. The peak at 520 cm^{-1} was originated from Si-substrate.

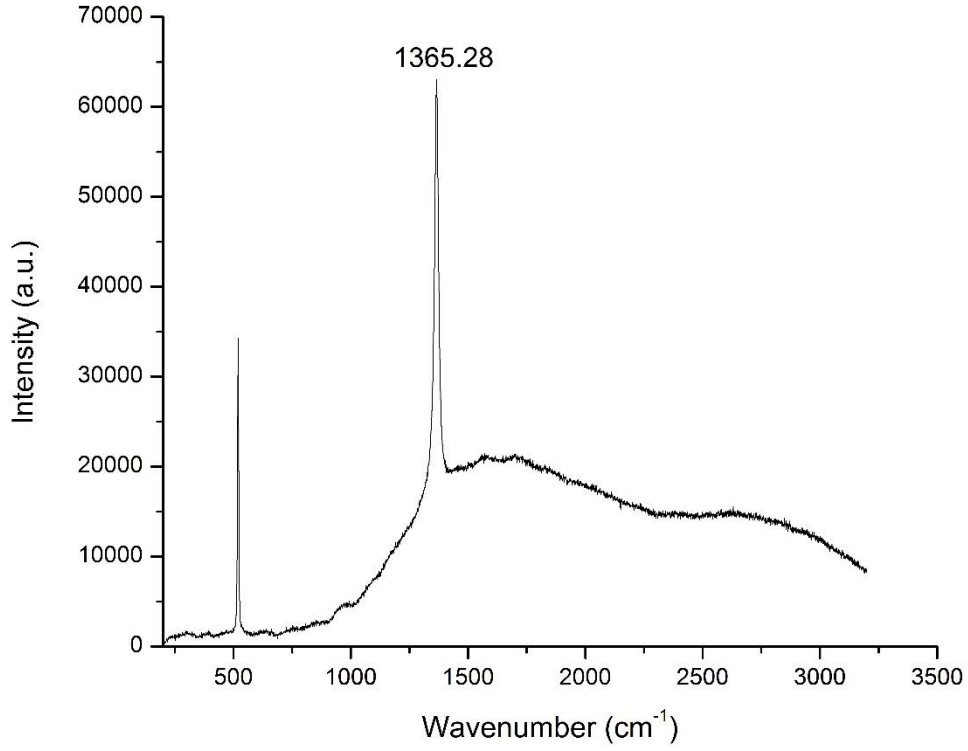

Figure 6. 8: Raman Spectrum of the BNNTs grow on Si-substrate

Other than a silicon wafer, there is white precipitate on the top of the precursor powder. SEM analysis of the sample simply taken by the spatula showed microtubes, which grew directly on the powder (Figure 6.9A-C). The diameter of the microtubes were changing from 1 micron to 5 microns (Figure 6.9D), and length of the tubes were over 50 microns and straight in nature. Some tubes seemed to be filled completely (Figure 6.9E), and some of them have open tips, and some of them were closed (Figure 6.9F).

Additional TEM analysis was performed for further characterization. Microtube structure was observed in the BN synthesis before. In 2009, BN microtubes were

synthesized through Li_2CO_3 and amorphous Boron powder by BOCVD method at 1350 ^oC.[109] Microtubes, which were produced by $NaFeO_2$, were formed in the powder at 900 ^oC. In figure 6.10, TEM analysis of the filled microtubes from Huang et al. work (Fig. 6.10A) and microtubes

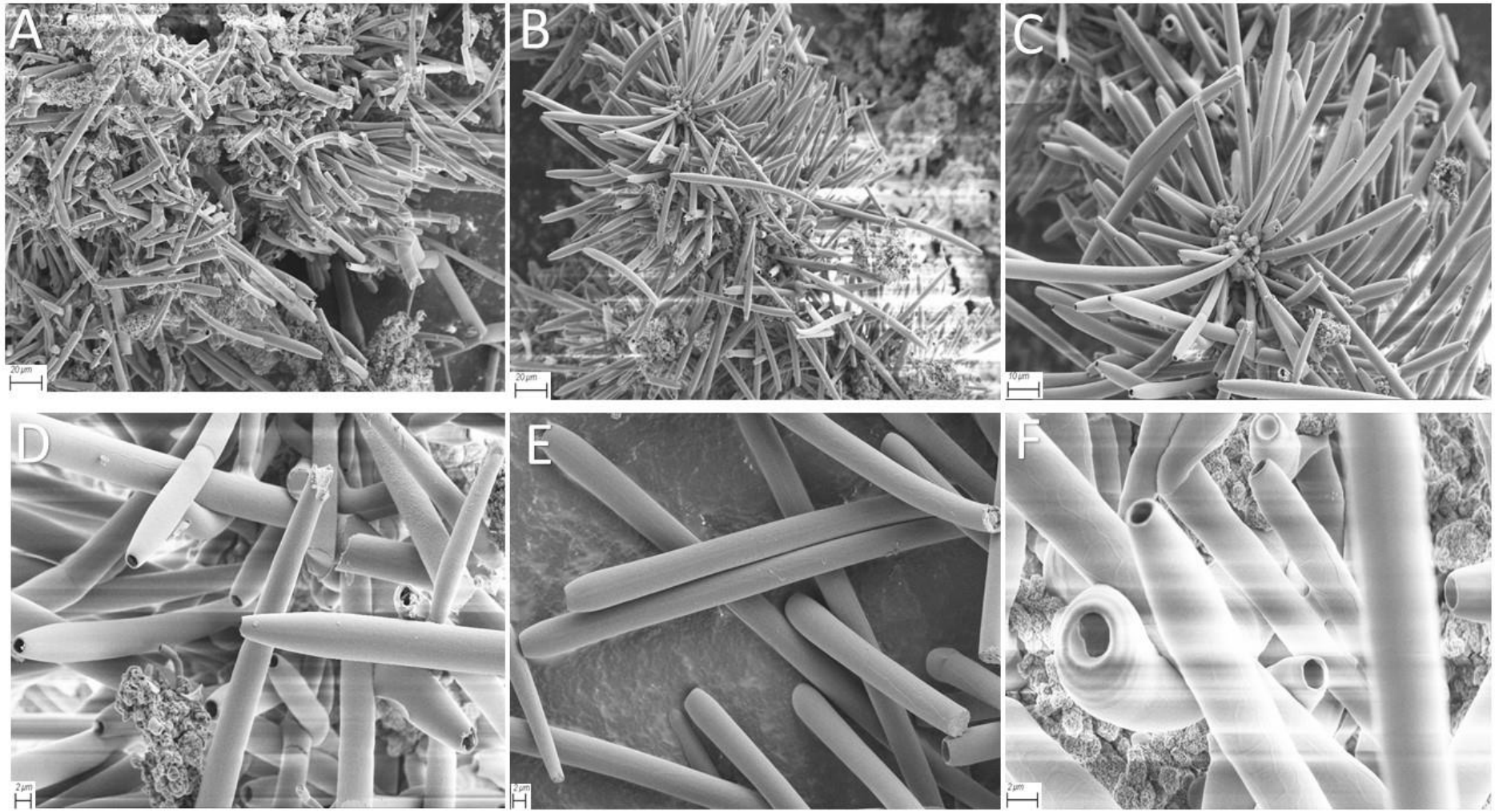

Figure 6. 9: SEM analysis of the microtubes in the powder

from this work shown together (Figure 6.10B). Filled structures were very similar to each other. Closed microtubes probably originated from filling of the metal oxides and open structures are formed through the melting of metals and flowing out from the open end of the BN microtubes by leaving hollow structure behind.

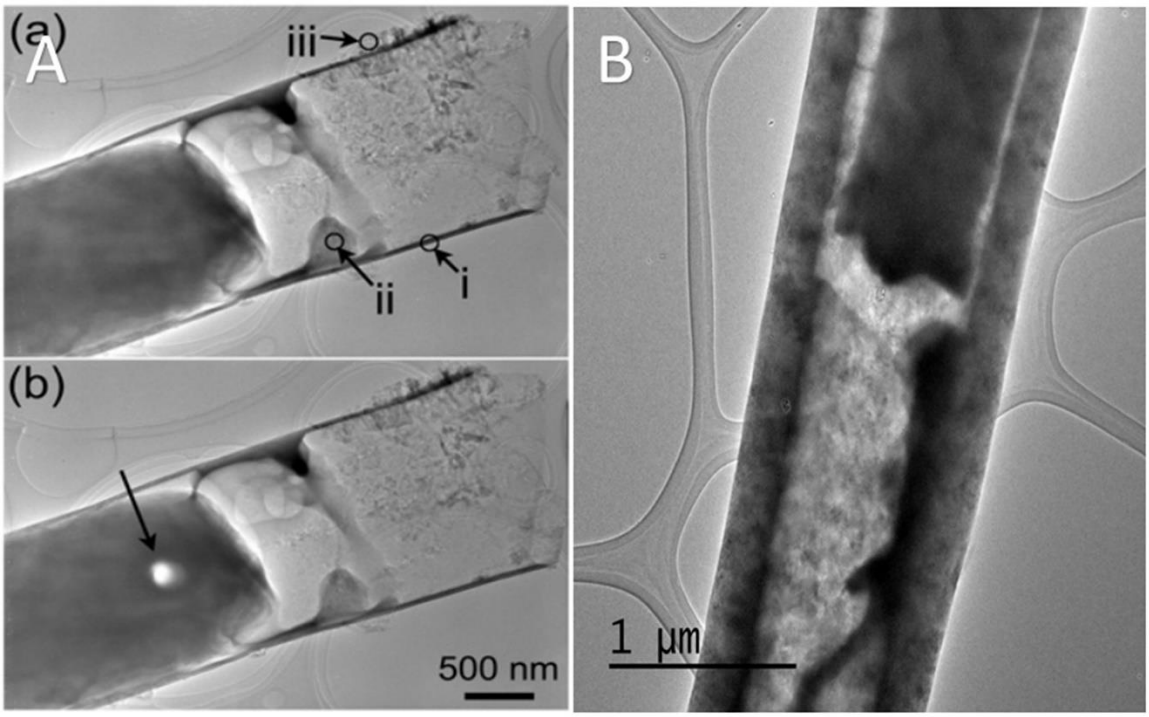

Figure 6. 10: BNNT microtubes A) Synthesized by $LiCO_3$ adapted from reference 109 B) BNNT synthesized in this work by $NaFeO_2$

EDX analysis of the BN microtube was shown in figure 6.11. Although elemental B detection with EDS is challenging to say the least, owing to its low energy and proximity to C K edge, mapping in combination with N can give an understanding of the spatial distribution of the element. As it can be seen in the figure, boron, and nitrogen concentrated of the wall of the microtube, the lesser intensity of the other wall probably originated from absorption of the relatively low energy x-rays originating from N by heavier elements before reaching the detector through the tube due to the high particle size of the microtube over 1 micron. Inside of the tube filled with metal oxides. Most concentrated elements are Na and oxygen. Other elements, K, Si, Al, and Mg probably

originated from the ceramic crucible. Fe is the less intense element that we measured by EDXS, even it was in the catalyst powder. Most reasonable explanation is the lowest partial pressure of iron do not let the iron to go through the inside of the tube by capillary forces.

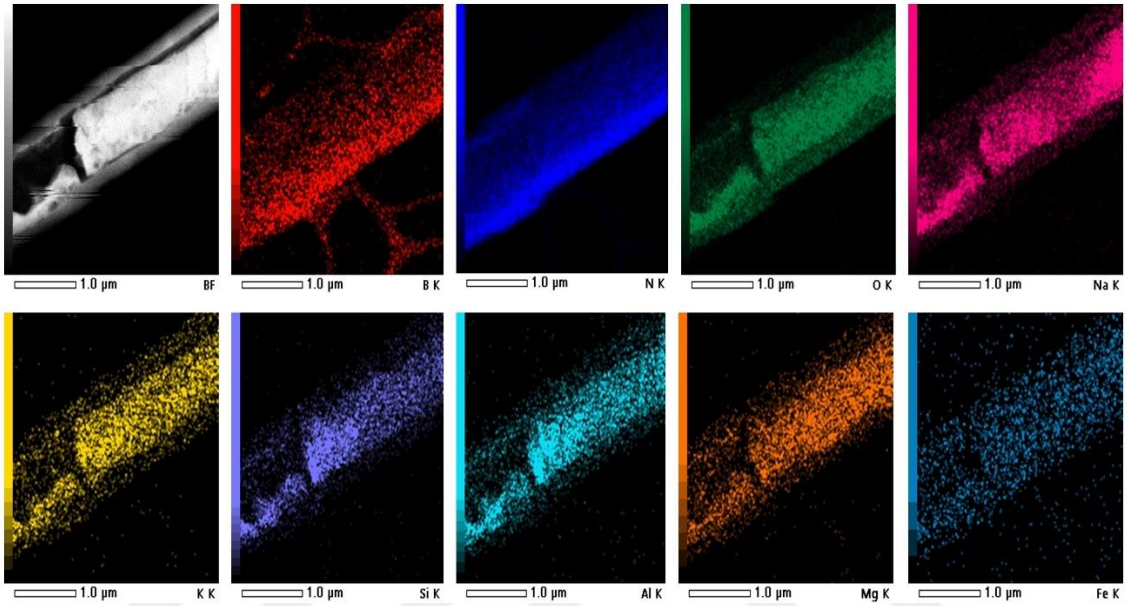

Figure 6. 11: EDX mapping of the filled BN microtube

In discussing growth mechanism of the microtubes, one important fact should be mentioned: VLS growth could not be the only mechanism that explains the growth of the microtubes because vapor phase growth was not necessary since microtubes grew on the powder. Also inside of some microtubes were filled with metal oxides.

Huang et al. suggested that BN microtube growth was directed from VLS and template self-sacrificing process.[109] Combination of these two process was summarized by the first formation of Li_2O-B_2O_3 liquid phase at 1350 ^oC then microdroplets turn into 2LiO-B_2O_3 microparticles, which act as a catalyst (nucleation point) for the growth of lithium borate fibers. With increasing temperature, these fibers segregated to higher lithium content borates and B_2O_3. Then B_2O_3 reacted with NH_3 at the surface and microtubes

were formed. At the end of the process, fibers act as a template for BN microtubes. In our process, we observe microtubes only on the top of the powder, driving force that leads to tube type growth should be the VLS mechanism. With increasing temperature, Na_2O segregated to the surface from the bulk $NaFeO_2$. At the surface, with increasing boron oxidation, B_2O_3 possibly formed and reacted with Na_2O. According to the phase diagram of Na_2O-B_2O_3, at 900 ^oC and low B_2O_3 content, the $3NaO.B_2O_3$ phase was formed, between 10 mol % B_2O_3 to 40 mol % B_2O_3, this phase was in liquid form which acts as a catalytic droplet.[164] In time, more B_2O_3 was created through the oxidation of boron and dissolved in this catalytic droplet. When B_2O_3 content in the melt reached the 50 %, the $Na_2O.B_2O_3$ phase was solidified and precipitated from the droplet. Arguably this solid phase form $NaO.B_2O_3$ fiber. Then, with increasing reaction time, Na evaporated from the fiber and according to the phase diagram B_2O_3 rich phases are form (NB_2, NB_3 and NB_4 (N represent Na_2O, B represent B_2O_3)) therefore surface of the fiber became boron oxide rich and this boron oxide arguably reacted with NH_3 and BN was crystallize at the surface. In the literature, B_2O_3 started to react with NH_3 to form BN, in this reaction alkali metal has a promoter effect on crystallization of BN.[125, 126] Also, Na_2CO_3 was used to catalyzed BN formation from boric acid and urea. It had been found that $NaCO_3$ addition leads to formation of sodium borate melt and h-BN crystallization via the reaction of sodium borate melt and ammonia at 1200 ^oC.[165]

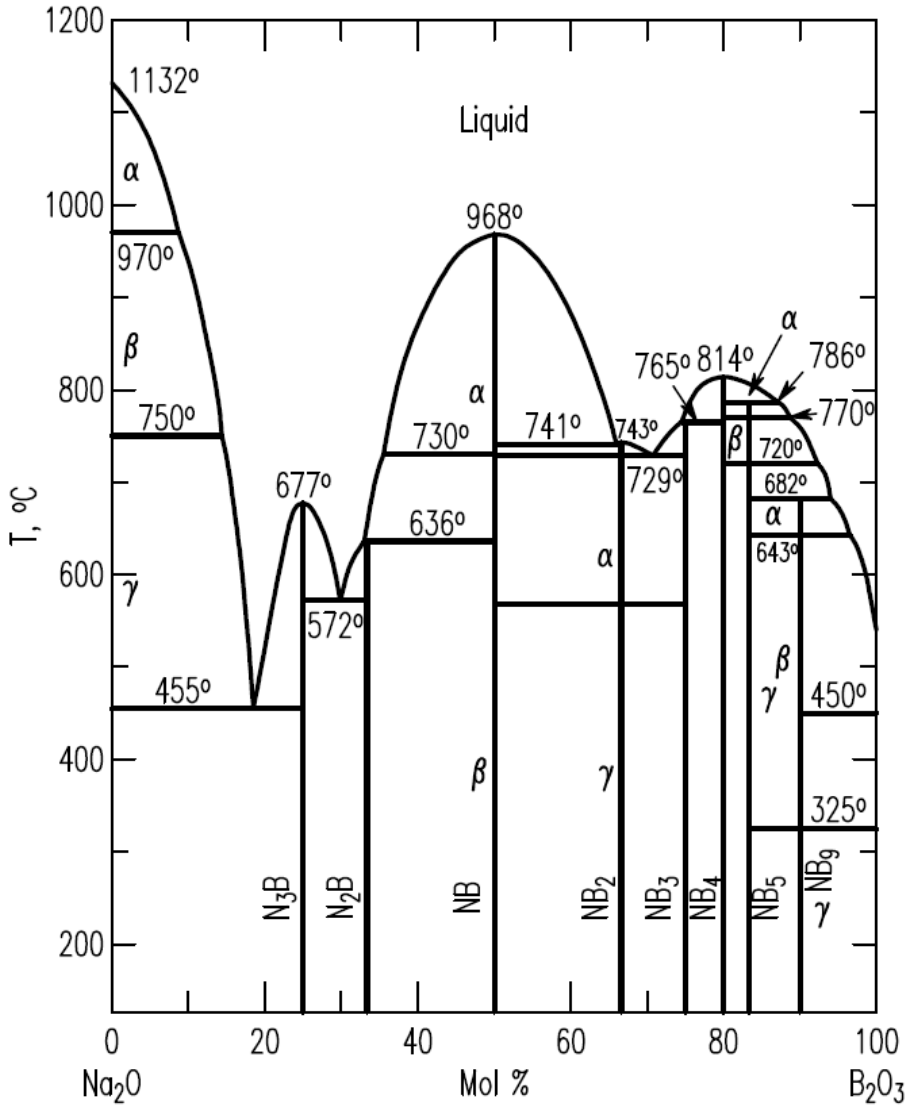

Figure 6. 12: Phase diagram of Na_2O-B_2O_3[164]

6.5 $LiFeO_2$ for BNNT synthesis

Lithium compound is frequently used for h-BN synthesis in the literature. For BNNT synthesis, Li_2O, Li_2CO_3, and $LiNO_3$ have already been used.[29, 30, 109, 163] Since promotion effect of lithium in BN crystallization have already been known, and closed diameter of lithium and magnesium which is the most used catalyst for BNNT make lithium a promising candidate. Also, another important feature of the lithium is the stability of Li_2O compared to the other alkali metal oxide. It can be used directly in the BNNT

growth process. However, the relatively low vapor pressure of lithium does not decrease CVD growth temperature of BNNTs. Even Mg have a lower boiling point than lithium. Above mentioned Li catalyst growth of BNNT processes were conducted at 1350 ºC over the boiling point of metallic lithium. We know that lithium can successfully catalyze the BNNT growth. However the effects of ferrite form such as decreasing temperature and new morphology of lithium on the BNNT formation have not been reported yet. Therefore, $LiFeO_2$ was synthesized like the other ferrites as explained in section 3.4. $LiFeO_2$ attract considerable interest as a cathode for rechargeable lithium batteries due to their low cost and toxicity.[166] $LiFeO_2$ has several polymorphs, whose detailed descriptions can be found elsewhere.[167] With our synthesis route, single-phase α-$LiFeO_2$ with the cubic structure of Fm3m space group (PDF 01-075-2963) was formed (Fig. 6.13). It crystallizes in rocksalt structure within Li, and Fe ions occupied octahedral sites randomly in a cubic close packing of oxygens. Even though as synthesized $LiFeO_2$ seems to be very stable in humid air, resulting product is stored in the glovebox for further use.

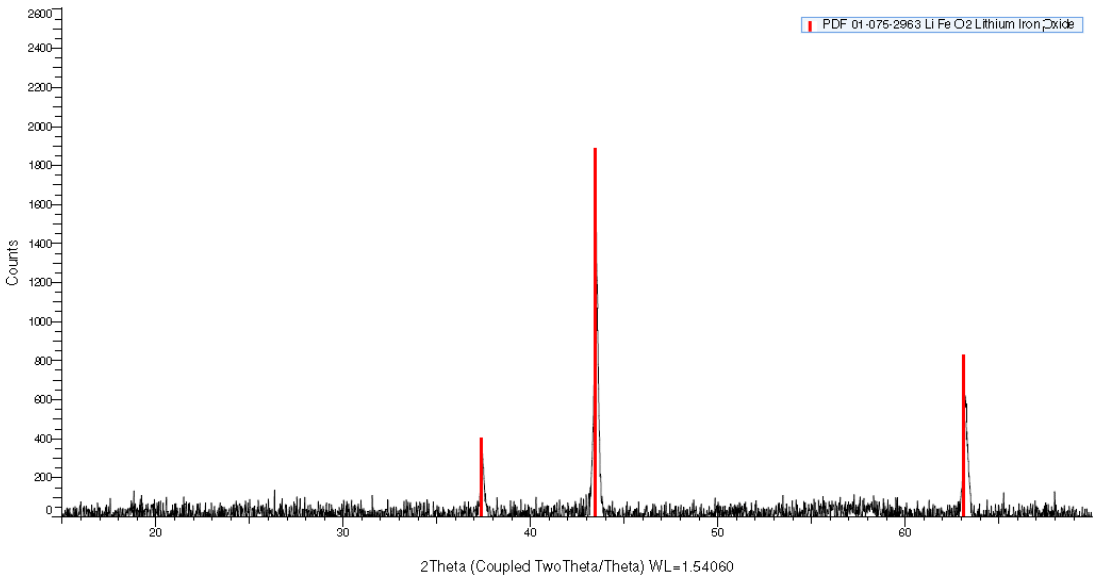

Figure 6. 13: X-ray diffraction pattern of $LiFeO_2$

6.5.1 BNNTs synthesis with $LiFeO_2$

BNNT synthesis with $LiFeO_2$ was conducted the same way as other alkali metal ferrites. Amorphous boron powder and $LiFeO_2$ (2:1 mole ratio) were mixed in the ceramic crucible. TCVD GVT approach was used to grow BNNTs. However, attempts to synthesize BNNT at low temperatures like in the case of $KFeO_2$ and $NaFeO_2$ was failed. Because, trials below 1000 ^oC did not yield any BNNT growth. The maximum temperature was 1100 ^oC for our system and tools. After 1000 ^oC, extensive glass formation occurred at the silica-based combustion boat due to the high flux of boron and lithium. At maximum temperature 1100 ^oC, there was an only small yield of BN structure as expected, since using lithium as an active catalyst (even in the ferrite form) requires high temperatures to desorb lithium and Li_2O species from the compound. Therefore, lithium did not cause any temperature decrease in CVD growth of BNNTs. However interesting BN morphology was achieved at 1100 ^oC with $LiFeO_2$. SEM analysis is represented in Figure 6.14.

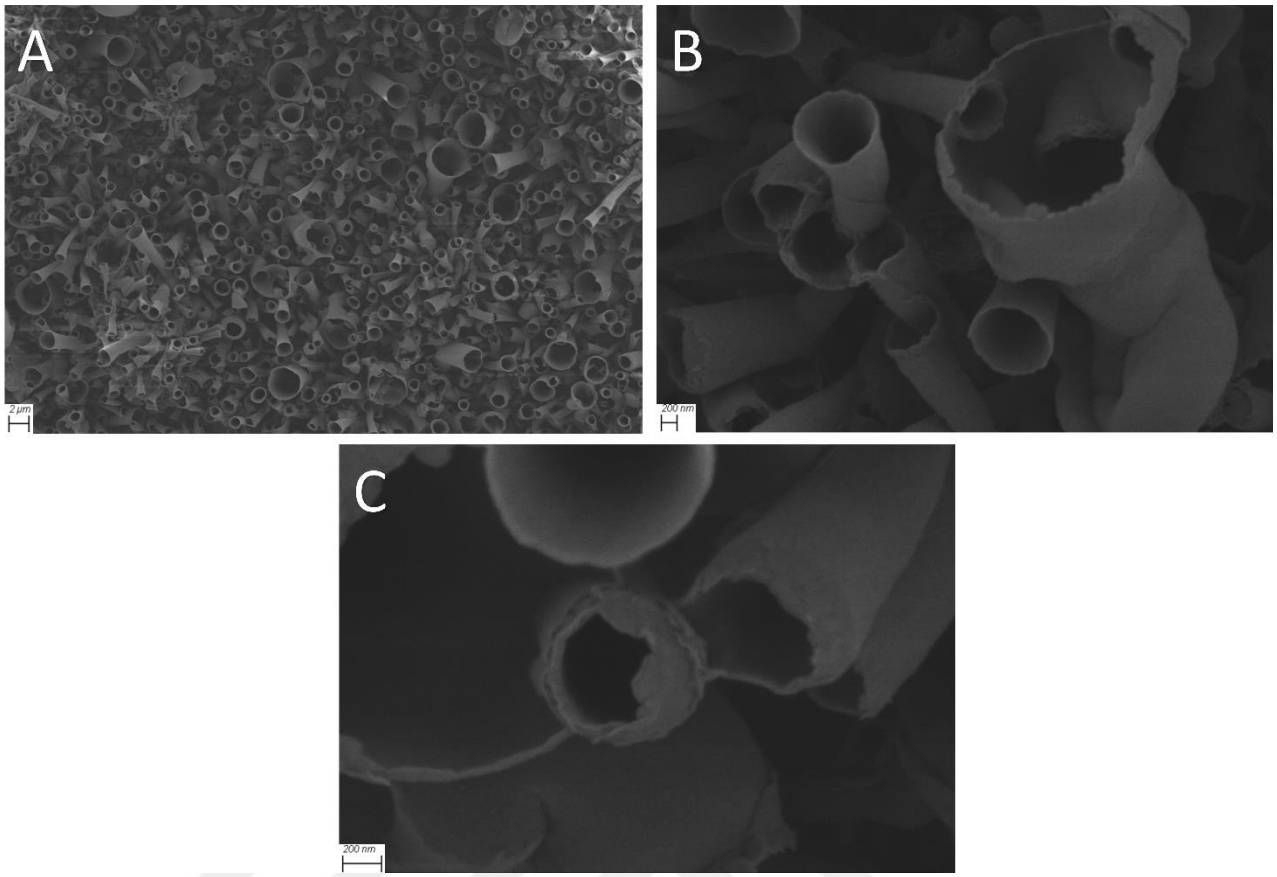

Figure 6. 14: BN morphology with $LiFeO_2$ at 1100 ^oC, A) Conical BN structures coverage B) Length in hollow cones C) Diameters

As it can be observed from the figure 6.14A, many hollow conical BN structures formed at the inner wall of the combustion boat. The lengths were up to two microns (Fig. 6.14B), and the diameters of the top parts were changing from 200 nm to 1 micron (Fig.6.14C). Usually, this type of structures are called nanohorns. However, the tip of the nanohorns are small and conical, and base of the structure are large in diameter, in this instance reverse structure was observed. They grow on the surface of the combustion boat, which means that base attached to the substrate and small in diameter then conically grow through the tip which in case larger in diameter. This type of morphology is often called tadpole-like structure due to the reassembly. Tadpole-like BN structures were synthesized in the literature before from Na_2SiO_3 .$9H_2O$, $Mg(NO_3)_2.6H_2O$ and amorphous boron by using co-precipitation method with CVD at

1250 °C.[168] SEM micrographs of the study were presented in figure 6.15 to observe similarity of the two structures.

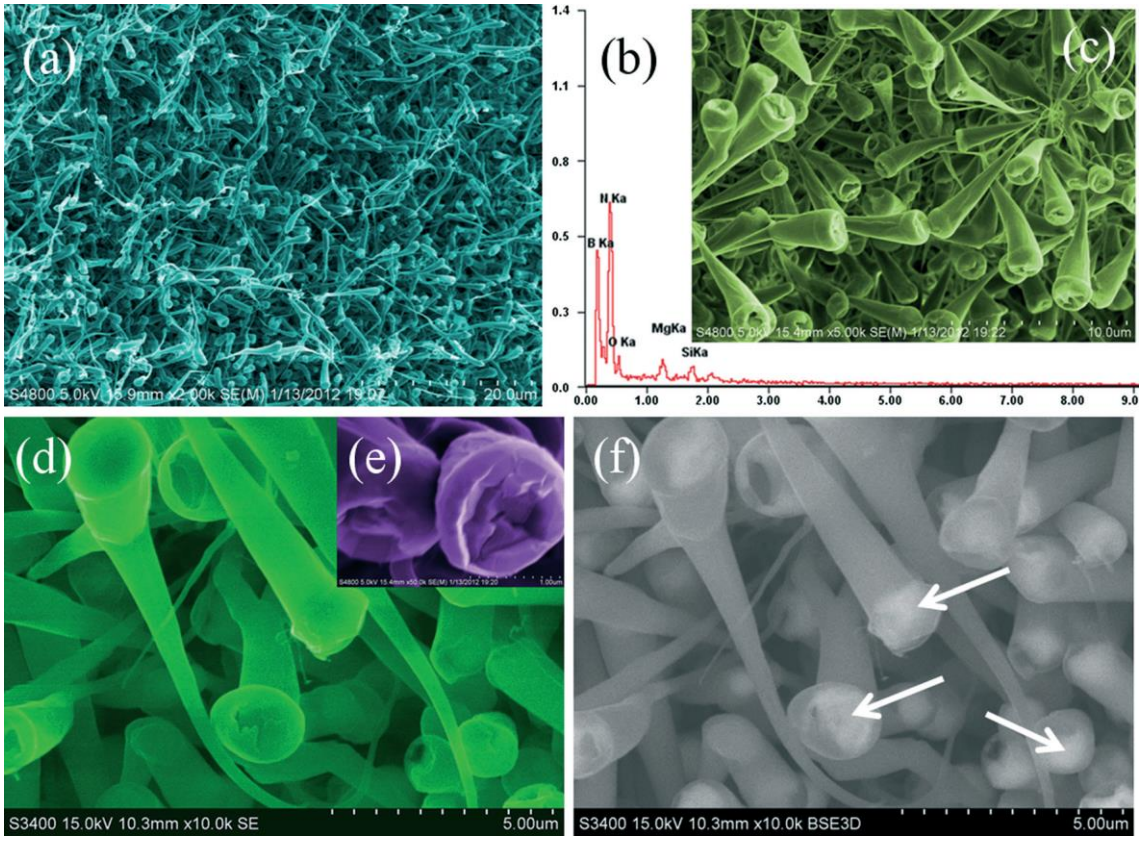

Figure 6. 15: BN tadpole structure synthesis from the literature. (Adapted from reference 168)

In their case, both closed and open structure were observed, on the other hand, we obtained only hollow structures. This could be the result of the formation of the glassy coating inside the crucible through the B and Li flux. They proposed mixed base type VLS and diffusion associated growth mechanism. However, they claim that large head of the structure was the base of the growth due to the catalytic particles they found. On the other hand, in our case base of the growth was small diameter tail of the structure, for this reason, we cannot expect the same growth mechanism. In 2013, tadpole-like CNTs were synthesized with TiO_2 catalyst.[169] They proposed initial step catalyst particle located in the tip of the nanotube and in time, it moved from the head to the tail.

During the movement of the catalyst particle, under prolonged growth conditions, it depleted by high temperature and reducing gas, which result in the smaller tail and larger head. This could be one mechanism for the tadpole-like BN structure formation with $LiFeO_2$. Further investigation and research is necessary for a comprehensive understanding of BN structures with $LiFeO_2$.

Additionally, we observed BNNT coating at the grip of the combustion boat which was affected relatively at low temperatures and only gas phase growth vapor such as B_2O_2 intermediate phase, BN, and catalyst vapor could reached there. SEM image of the BNNTs at the grip was presented in Figure 6.16. However, only a small amount of BNNT were formed during the synthesis due to the very low vapor pressure of the Li catalyst in the growth vapor at 1100 ^oC. The result show that higher temperatures require for the growth of the BNNTs with $LiFeO_2$ catalyst.

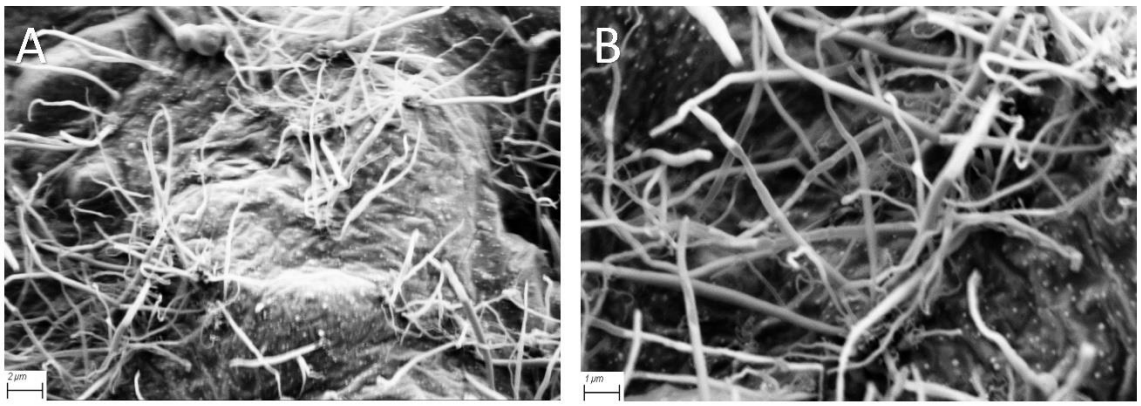

Figure 6. 16: as synthesis BNNTs with $LiFeO_2$ at the grip of the combustion boat

6.6 Conclusion

In conclusion, we demonstrated BNNT synthesis with alkali metal ferrites other than $KFeO_2$. To decrease BNNT growth temperature, we started form highest vapor pressure alkali metal Cs to lowest vapor pressure Li in their ferrite form. $CsFeO_2$ did not yield any BNNT growth between 600 ^oC to 700 ^oC due to the large size of the Cs and low reaction temperatures. After 700 ^oC, growth was not possible because all Cs

evaporated. $NaFeO_2$, on the other hand, gave very high yield for BNNT growth on the combustion boat wall at 900 ^oC (over Na boiling point). Below Na boiling point at 800 ^oC, BNNT growth was not significant unlike $KFeO_2$ case, which BNNTs were successfully grown at 800 ^oC. Mixed morphology thin-straight and thick-curly nanotubes were observed. Base growth VLS mechanism was proposed due to the lack of the tip particle in the TEM analysis. Also, BN microtubes formed at the top of the precursor powders with a $NaFeO_2$ catalyst with diameters changing from 1 ηm to 5 ηm. Suggested growth mechanism is the mix of the base growth VLS and template self-sacrificing process. With $LiFeO_2$, low temperature growth below 1000 ^oC was not achieved due to the high boiling point of Li. However, at 1100 ^oC, BN nano-tadpole like structures and BNNTs were formed, but yield was very low. More investigations were needed to propose growth mechanism of tadpole-like structures. Results suggest that without alkali metal catalyst vapor in the growth vapor, the formation of the BNNTs were not possible. Moreover, BNNT growth temperature highly depends on the boiling point of alkali metals in the ferrite structure.

CHAPTER 7

7 GENERAL CONCLUSIONS

In this study, we have achieved BNNT growth by alkali metal ferrites with CVD method for the first time in the existing literature. Three steps were applied through the whole research. ***i)*** *Before proposed new catalyst for BNNT synthesis, conventional catalyst system (MgO and Fe_2O_3) was used for BNNT synthesis with TCVD GVT approach. Moreover, CVD system parameters were investigated with the existing process. It was found to be the temperature is the most effective factor for BNNTs to form.* ***ii)*** *To reduce BNNT synthesis temperature with TCVD, new catalytic materials were searched. Potassium was found to be the effective catalyst for low temperature (below 1000 ^oC) synthesis of BNNTs due to its high vapor pressure. Through this point, $KFeO_2$ was replaced with the conventional catalyst and BNNT synthesis temperature with TCVD was reduced to as low as 750 ^oC. Growth mechanism and effect of alkali metal were investigated.* ***iii)*** *To support the idea of alkali assisted BNNT synthesis, other alkali metal ferrites from Cs to Li were used in the BNNT synthesis with TCVD. Although reducing BNNT synthesis temperature even more with $CsFeO_2$ was not successful, it was proved to be the without alkali metal catalyst in the growth vapor BNNT synthesis was not possible. Moreover, synthesis temperature was changed depending on the alkali metal used as in ferrite form.*

All conclusions of three steps of BNNT synthesis with alkali metal ferrites were summarized below.

i) Conventional catalyst system

BNNTs were synthesis with TCVD method GVT approach with MgO/Fe_2O_3 conventional catalysis system at 1000 ^oC to 1200 ^oC similar to the literature. Si

substrates were coated with MgO. Because without MgO catalyst vapor, BNNT growth on the substrates was not achieved. Preliminary studies were showed that precursor ratio (amorphous boron powder/MgO/Fe_2O_3) should be 4/1/1 respectively for homogeneity of the BNNT coating on the substrate and reaction time at maximum temperature was stabilized at 30 minutes. UV-vis studies of the extracted nanotubes showed that BNNTs synthesized at different temperatures 1000 ^oC, 1100 ^oC and 1200 ^oC, have almost the same (5.8 eV) band gap, independent of morphology and diameter. TEM analysis showed that BNNTs were hollow, and had a multiwalled structure with the diameters of the BNNTs are changing from 30 nm to 80 nm. Most of the nanotubes are grown in entangled curly fashion and showed cup type bamboo like hollow morphologies. Curved nanotubes have close tips, some of them were incorporated with metal particles and some of them without which suggest the mixed (base and tip) growth mode of the BNNTs. Optimization experiments were carried out to find three main response substrate coverage, film thickness and BNNT aspect ratio to determine effects of CVD process parameters (reaction temperature (f_1), heating rate (f_2) and reactive gas flow rate (f_3)) on the growth quality. SEM analysis (followed by image processing) for nanotube diameter and RAMAN analysis for grown BNNT thickness measurements and substrate surface coverage were used. SEM micrographs were investigated in detail, at constant reactive gas flow rates, BNNT formation efficiency increase with increasing temperature from 1000 ^oC to 1200 ^oC. Likewise, when the reaction temperature kept constant, BNNT yield increased with increasing NH_3 flow rate. Generally, bamboo-like morphologies were observed. However, at lower heating rates different morphologies such as onion like bases were detected. Nanohorn like morphologies which getting thinner through the tip but thicker at the bottom were more frequently observed at low heating rates and low NH_3 flow. Optimization responses concluded that BNNT

synthesis with conventional catalysis system mostly depended on the temperature of the synthesis. Although high aspect ratios can be achieved low temperatures (1000 ^{o}C) below Mg boiling point, BNNT coverage (yield) and the film thickness was low. High coverage, high film thickness and good aspect ratio can be reached at high temperature 1200 ^{o}C (over Mg boiling point), high NH_3 flow rate (200 ^{o}C) and low heating rate 5 ^{o}C/min.

ii) New $KFeO_2$ catalyst

Alternative catalytic parent material ($KFeO_2$) was presented for BNNT synthesis instead of conventional catalytic system (MgO/FeO) used in the literature frequently. By using $KFeO_2$ as a catalyst in BNNT TCVD synthesis energy efficiency of was increased. Moreover, the dependence of the high temperatures (over 1000 ^{o}C) was eliminated where the conventional catalysts do not work.

We demonstrated that high quality, long and straight MWBNNTs can be produced on the ceramic substrate efficiently at low temperatures by using $KFeO_2$ as the parent material for catalyst in TCVD method. Although optimum temperature for our system was 800 ^{o}C, BNNTs can be grown after 750 ^{o}C. The success of the BNNT production via this approach is due to the combination of efficient potassium desorption from the $KFeO_2$ parent material, creation of reactive boron intermediates from potassium and iron oxide species, and nevertheless porous structure of the ceramic substrate. TEM results demonstrated encapsulated catalytic particles in the core of the tips. This behavior suggested that tip growth mechanism is dominant in the synthesized BNNTs. The output of this study is significant that high quality BNNTs could be produced on the porous substrates that are sensitive to high temperatures by using $KFeO_2$ with readily available tube furnace.

iii) Other alkali metal ferrites as a catalyst

We demonstrated BNNT synthesis with alkali metal ferrites other than $KFeO_2$. To decrease BNNT growth temperature, we started form highest vapor pressure alkali metal Cs to lowest vapor pressure Li in their ferrite form. $CsFeO_2$ did not yield any BNNT growth between 600 ^oC to 700 ^oC due to the large size of the Cs and low reaction temperatures. After 700 ^oC, growth was not possible because all Cs was evaporated. $NaFeO_2$, on the other hand, gave very high yield BNNT growth on the combustion boat wall at 900 ^oC (over Na boiling point). Below Na boiling point at 800 ^oC, BNNT growth was not significant, unlike $KFeO_2$ case which BNNTs were successfully grown at 800 ^oC. Mixed morphology thin-straight and thick-curly nanotubes were observed. Base growth VLS mechanism was proposed due to the lack of the tip particle in the TEM analysis. In addition, BN microtubes formed at the top of the precursor powders with a $NaFeO_2$ catalyst with diameters changing from 1 ηm to 5 ηm. Suggested growth mechanism is the mix of the base growth VLS and template self-sacrificing process. With $LiFeO_2$, low temperature growth below 1000 ^oC was not achieved due to the high boiling point of Li. However, at 1100 ^oC, BN nano-tadpole like structures and BNNTs were formed, but yield was very low. More investigation was needed to propose growth mechanism of tadpole-like structures.

References

1. Iijima, S. *Nature* **1991,** 354, (6348), 56-58.

2. Han, W.-Q., Anisotropic Hexagonal Boron Nitride Nanomaterials: Synthesis and Applications. In *Nanotechnologies for the Life Sciences*, Wiley-VCH Verlag GmbH & Co. KGaA: 2007.

3. Golberg, D.; Bando, Y.; Huang, Y.; Terao, T.; Mitome, M.; Tang, C.; Zhi, C. *ACS Nano* **2010,** 4, (6), 2979-2993.

4. Wang, J.; Lee, C. H.; Yap, Y. K. *Nanoscale* **2010,** 2, (10), 2028-2034.

5. Golberg, D.; Bando, Y.; Kurashima, K.; Sato, T. *Scripta Materialia* **2001,** 44, (8), 1561-1565.

6. Zhi, C.; Bando, Y.; Tang, C.; Xie, R.; Sekiguchi, T.; Golberg, D. *Journal of the American Chemical Society* **2005,** 127, (46), 15996-15997.

7. Nakhmanson, S. M.; Calzolari, A.; Meunier, V.; Bernholc, J.; Buongiorno Nardelli, M. *Physical Review B* **2003,** 67, (23), 235406.

8. Yitao, D.; Wanlin, G.; Zhuhua, Z.; Bin, Z.; Chun, T. *Journal of Physics D: Applied Physics* **2009,** 42, (8), 085403.

9. Cohen, M. L.; Zettl, A. *Phys. Today* **2010,** 63, (11), 34-38.

10. Li, L. H.; Chen, Y. *Langmuir* **2010,** 26, (7), 5135-5140.

11. Lee, C. H.; Drelich, J.; Yap, Y. K. *Langmuir* **2009,** 25, (9), 4853-4860.

12. Rubio, A.; Corkill, J. L.; Cohen, M. L. *Physical Review B* **1994,** 49, (7), 5081.

13. Chopra, N. G.; Luyken, R. J.; Cherrey, K.; Crespi, V. H.; Cohen, M. L.; Louie, S. G.; Zettl, A. *Science* **1995,** 269, (5226), 966-967.

14. Wang, J.; Lee, C. H.; Bando, Y.; Golberg, D.; Yap, Y. K., Multiwalled Boron Nitride Nanotubes: Growth, Properties, and Applications. In *B-C-N Nanotubes and Related Nanostructures*, Springer New York: New York, NY, 2009; pp 23-44.

15. Ahmad, P.; Khandaker, M. U.; Khan, Z. R.; Amin, Y. M. *RSC Advances* **2015,** 5, (44), 35116-35137.

16. Terrones, M.; Romo-Herrera, J. M.; Cruz-Silva, E.; López-Urías, F.; Muñoz-Sandoval, E.; Velázquez-Salazar, J. J.; Terrones, H.; Bando, Y.; Golberg, D. *Materials Today* **2007,** 10, (5), 30-38.

17. Ma, R.; Golberg, D.; Bando, Y.; Sasaki, T. *Philosophical Transactions of the Royal Society of London. Series A: Mathematical, Physical and Engineering Sciences* **2004,** 362, (1823), 2161-2186.

18. Sen, R.; Satishkumar, B. C.; Govindaraj, A.; Harikumar, K. R.; Raina, G.; Zhang, J.-P.; Cheetham, A. K.; Rao, C. N. R. *Chemical Physics Letters* **1998,** 287, (5), 671-676.

19. Shelimov, K. B.; Moskovits, M. *Chemistry of Materials* **2000,** 12, (1), 250-254.

20. Lourie, O. R.; Jones, C. R.; Bartlett, B. M.; Gibbons, P. C.; Ruoff, R. S.; Buhro, W. E. *Chemistry of Materials* **2000,** 12, (7), 1808-1810.

21. Kim, M. J.; Chatterjee, S.; Kim, S. M.; Stach, E. A.; Bradley, M. G.; Pender, M. J.; Sneddon, L. G.; Maruyama, B. *Nano Letters* **2008,** 8, (10), 3298-3302.

22. Tang, C.; Bando, Y.; Sato, T.; Kurashima, K. *Chemical Communications* **2002**, (12), 1290-1291.

23. Zhi, C.; Bando, Y.; Tan, C.; Golberg, D. *Solid State Communications* **2005,** 135, (1), 67-70.

24. Chee Huei, L.; Jiesheng, W.; Vijaya, K. K.; Jian, Y. H.; Yoke Khin, Y. *Nanotechnology* **2008,** 19, (45), 455605.

25. Lee, C. H.; Xie, M.; Kayastha, V.; Wang, J.; Yap, Y. K. *Chemistry of Materials* **2010,** 22, (5), 1782-1787.

26. Ahmad, P.; Khandaker, M. U.; Amin, Y. M. *Physica E: Low-dimensional Systems and Nanostructures* **2015,** 67, 33-37.

27. Amir, P.; Chunyi, Z.; Yoshio, B.; Tomonobu, N.; Dmitri, G. *Nanotechnology* **2012,** 23, (21), 215601.

28. Oku, T.; Koi, N.; Suganuma, K.; Belosludov, R. V.; Kawazoe, Y. *Solid State Communications* **2007,** 143, (6), 331-336.

29. Yang, H.; Jing, L.; Chengchun, T.; Yoshio, B.; Chunyi, Z.; Tianyou, Z.; Benjamin, D.; Takashi, S.; Dmitri, G. *Nanotechnology* **2011,** 22, (14), 145602.

30. Li, L.; Liu, X.; Li, L.; Chen, Y. *Microelectronic Engineering* **2013,** 110, 256-259.

31. Balmain, W. H. *Journal für Praktische Chemie* **1842,** 27, (1), 422-430.

32. Alterovitz, S. A.; Pouch, J. J., *Synthesis and properties of boron nitride*. Trans Tech: Aedermannsdorf, Switzerland, 1990; p 415 p.

33. Pakdel, A.; Bando, Y.; Golberg, D. *Chemical Society Reviews* **2014,** 43, (3), 934-959.

34. Meng, Y.; Mao, H.-k.; Eng, P. J.; Trainor, T. P.; Newville, M.; Hu, M. Y.; Kao, C.; Shu, J.; Hausermann, D.; Hemley, R. J. *Nat Mater* **2004,** 3, (2), 111-114.

35. Zhang, W. J.; Bello, I.; Lifshitz, Y.; Lee, S. T. *MRS Bulletin* **2011,** 28, (3), 184-188.

36. Mirkarimi, P. B.; McCarty, K. F.; Medlin, D. L. *Materials Science and Engineering: R: Reports* **1997,** 21, (2), 47-100.

37. Blase, X.; Rubio, A.; Louie, S. G.; Cohen, M. L. *EPL (Europhysics Letters)* **1994,** 28, (5), 335.

38. Tiano, A. L.; Park, C.; Lee, J. W.; Luong, H. H.; Gibbons, L. J.; Chu, S.-H.; Applin, S. I.; Gnoffo, P.; Lowther, S.; Kim, H. J. **2014**.

39. Wilder, J. W. G.; Venema, L. C.; Rinzler, A. G.; Smalley, R. E.; Dekker, C. *Nature* **1998,** 391, (6662), 59-62.

40. Zhi, C.; Bando, Y.; Terao, T.; Tang, C.; Kuwahara, H.; Golberg, D. *Advanced Functional Materials* **2009,** 19, (12), 1857-1862.

41. Kang, J. H.; Sauti, G.; Park, C.; Yamakov, V. I.; Wise, K. E.; Lowther, S. E.; Fay, C. C.; Thibeault, S. A.; Bryant, R. G. *ACS Nano* **2015,** 9, (12), 11942-11950.

42. Keun Su, K.; Myung Jong, K.; Cheol, P.; Catharine, C. F.; Sang-Hyon, C.; Christopher, T. K.; Benoit, S. *Semiconductor Science and Technology* **2017,** 32, (1), 013003.

43. Kim, K. S.; Kingston, C. T.; Hrdina, A.; Jakubinek, M. B.; Guan, J.; Plunkett, M.; Simard, B. *ACS Nano* **2014,** 8, (6), 6211-6220.

44. Golberg, D.; Bando, Y.; Tang, C. C.; Zhi, C. Y. *Advanced Materials* **2007,** 19, (18), 2413-2432.

45. Chen, Y.; Zou, J.; Campbell, S. J.; Caer, G. L. *Applied Physics Letters* **2004,** 84, (13), 2430-2432.

46. Xiao, Y.; Yan, X. H.; Cao, J. X.; Ding, J. W.; Mao, Y. L.; Xiang, J. *Physical Review B* **2004,** 69, (20), 205415.

47. Chang, C. W.; Fennimore, A. M.; Afanasiev, A.; Okawa, D.; Ikuno, T.; Garcia, H.; Li, D.; Majumdar, A.; Zettl, A. *Phys Rev Lett* **2006,** 97, (8), 085901.

48. Chopra, N. G.; Zettl, A. *Solid State Communications* **1998,** 105, (5), 297-300.

49. Hernández, E.; Goze, C.; Bernier, P.; Rubio, A. *Physical Review Letters* **1998,** 80, (20), 4502-4505.

50. Dumitrică, T.; Bettinger, H. F.; Scuseria, G. E.; Yakobson, B. I. *Physical Review B* **2003,** 68, (8), 085412.

51. Tanur, A. E.; Wang, J.; Reddy, A. L. M.; Lamont, D. N.; Yap, Y. K.; Walker, G. C. *The Journal of Physical Chemistry B* **2013,** 117, (16), 4618-4625.

52. Golberg, D.; Bai, X. D.; Mitome, M.; Tang, C. C.; Zhi, C. Y.; Bando, Y. *Acta Materialia* **2007,** 55, (4), 1293-1298.

53. Miyamoto, Y.; Rubio, A.; Cohen, M. L.; Louie, S. G. *Physical Review B* **1994,** 50, (7), 4976-4979.

54. Kim, Y.-H.; Chang, K. J.; Louie, S. G. *Physical Review B* **2001,** 63, (20), 205408.

55. Ishigami, M.; Sau, J. D.; Aloni, S.; Cohen, M. L.; Zettl, A. *Phys Rev Lett* **2005,** 94, (5), 056804.

56. Khoo, K. H.; Mazzoni, M. S. C.; Louie, S. G. *Physical Review B* **2004,** 69, (20), 201401.

57. Ahmad, P.; Khandaker, M. U.; Amin, Y. M. *Ceramics International* **2015,** 41, (3), 4544-4548.

58. Kalay, S.; Yilmaz, Z.; Sen, O.; Emanet, M.; Kazanc, E.; Çulha, M. *Beilstein Journal of Nanotechnology* **2015,** 6, 84-102.

59. Li, L. H.; Chen, Y.; Glushenkov, A. M. *Journal of Materials Chemistry* **2010,** 20, (43), 9679-9683.

60. Yu, J.; Qin, L.; Hao, Y.; Kuang, S.; Bai, X.; Chong, Y.-M.; Zhang, W.; Wang, E. *ACS Nano* **2010,** 4, (1), 414-422.

61. Mpourmpakis, G.; Froudakis, G. E. *Catalysis today* **2007,** 120, (3), 341-345.

62. Ma, R.; Bando, Y.; Zhu, H.; Sato, T.; Xu, C.; Wu, D. *Journal of the American Chemical Society* **2002,** 124, (26), 7672-7673.

63. Tang, C.; Bando, Y.; Ding, X.; Qi, S.; Golberg, D. *Journal of the American Chemical Society* **2002,** 124, (49), 14550-14551.

64. Kim, K. S.; Jakubinek, M. B.; Martinez-Rubi, Y.; Ashrafi, B.; Guan, J.; O'Neill, K.; Plunkett, M.; Hrdina, A.; Lin, S.; Denommee, S.; Kingston, C.; Simard, B. *RSC Advances* **2015,** 5, (51), 41186-41192.

65. Zhi, C.; Bando, Y.; Tang, C.; Honda, S.; Kuwahara, H.; Golberg, D. *Journal of Materials Research* **2006,** 21, (11), 2794-2800.

66. Zhi, C. Y.; Bando, Y.; Wang, W. L.; Tang, C. C.; Kuwahara, H.; Golberg, D. *Journal of Nanomaterials* **2008,** 2008, 1-5.

67. Watts, P. C. P.; Fearon, P. K.; Hsu, W. K.; Billingham, N. C.; Kroto, H. W.; Walton, D. R. M. *Journal of Materials Chemistry* **2003,** 13, (3), 491-495.

68. Pham, J. Q.; Mitchell, C. A.; Bahr, J. L.; Tour, J. M.; Krishanamoorti, R.; Green, P. F. *Journal of Polymer Science Part B: Polymer Physics* **2003,** 41, (24), 3339-3345.

69. Huang, X.; Zhi, C.; Jiang, P.; Golberg, D.; Bando, Y.; Tanaka, T. *Advanced Functional Materials* **2013,** 23, (14), 1824-1831.

70. Terao, T.; Zhi, C.; Bando, Y.; Mitome, M.; Tang, C.; Golberg, D. *The Journal of Physical Chemistry C* **2010,** 114, (10), 4340-4344.

71. Bansal, N. P.; Hurst, J. B.; Choi, S. R. *Journal of the American Ceramic Society* **2006,** 89, (1), 388-390.

72. Qing, H.; Yoshio, B.; Xin, X.; Toshiyuki, N.; Chunyi, Z.; Chengchun, T.; Fangfang, X.; Lian, G.; Dmitri, G. *Nanotechnology* **2007,** 18, (48), 485706.

73. Golberg, D.; Bando, Y.; Dorozhkin, P.; Dong, Z.-C. *MRS bulletin* **2004,** 29, (1), 38-42.

74. Golberg, D.; Dorozhkin, P. S.; Bando, Y.; Dong, Z.-C.; Tang, C. C.; Uemura, Y.; Grobert, N.; Reyes-Reyes, M.; Terrones, H.; Terrones, M. *Applied Physics A* **2003,** 76, (4), 499-507.

75. Watanabe, K.; Taniguchi, T.; Kanda, H. *Nat Mater* **2004,** 3, (6), 404-409.

76. Huang, Q.; Bando, Y.; Zhao, L.; Zhi, C. Y.; Golberg, D. *Nanotechnology* **2009,** 20, (41), 415501.

77. Loiseau, A.; Willaime, F.; Demoncy, N.; Hug, G.; Pascard, H. *Physical Review Letters* **1996,** 76, (25), 4737-4740.

78. Narita, I.; Oku, T. *Solid State Communications* **2002,** 122, (9), 465-468.

79. Yahachi, S.; Masatomo, M.; Takehisa, M. *Japanese Journal of Applied Physics* **1999,** 38, (1R), 159.

80. Altoe, M. V. P.; Sprunck, J. P.; Gabriel, J.-C. P.; Bradley, K. *Journal of Materials Science* **2003,** 38, (24), 4805-4810.

81. Lee, C. M.; Choi, S. I.; Choi, S. S.; Hong, S. H. *Current Applied Physics* **2006,** 6, (2), 166-170.

82. Golberg, D.; Bando, Y.; Eremets, M.; Takemura, K.; Kurashima, K.; Yusa, H. *Applied Physics Letters* **1996,** 69, (14), 2045-2047.

83. Yu, D. P.; Sun, X. S.; Lee, C. S.; Bello, I.; Lee, S. T.; Gu, H. D.; Leung, K. M.; Zhou, G. W.; Dong, Z. F.; Zhang, Z. *Applied Physics Letters* **1998,** 72, (16), 1966-1968.

84. Lee, R. S.; Gavillet, J.; Chapelle, M. L. d. l.; Loiseau, A.; Cochon, J. L.; Pigache, D.; Thibault, J.; Willaime, F. *Physical Review B* **2001,** 64, (12), 121405.

85. Arenal, R.; Stephan, O.; Cochon, J.-L.; Loiseau, A. *Journal of the American Chemical Society* **2007,** 129, (51), 16183-16189.

86. Michael, W. S.; Kevin, C. J.; Cheol, P.; Jae-Woo, K.; Peter, T. L.; Roy, C.; Joycelyn, S. H. *Nanotechnology* **2009,** 20, (50), 505604.

87. Fathalizadeh, A.; Pham, T.; Mickelson, W.; Zettl, A. *Nano Letters* **2014,** 14, (8), 4881-4886.

88. Chen, Y.; Fitz Gerald, J.; Williams, J. S.; Bulcock, S. *Chemical Physics Letters* **1999,** 299, (3), 260-264.

89. Lu Hua, L.; Ying, C.; Alexey, M. G. *Nanotechnology* **2010,** 21, (10), 105601.

90. Li, L.; Li, L. H.; Chen, Y.; Dai, X. J.; Xing, T.; Petravic, M.; Liu, X. *Nanoscale Research Letters* **2012,** 7, (1), 417.

91. Han, W.; Bando, Y.; Kurashima, K.; Sato, T. *Applied Physics Letters* **1998,** 73, (21), 3085-3087.

92. Golberg, D.; Bando, Y.; Kurashima, K.; Sato, T. *Chemical Physics Letters* **2000,** 323, (1), 185-191.

93. Bechelany, M.; Bernard, S.; Brioude, A.; Cornu, D.; Stadelmann, P.; Charcosset, C.; Fiaty, K.; Miele, P. *The Journal of Physical Chemistry C* **2007,** 111, (36), 13378-13384.

94. Wang, Y.; Shimada, S.; Yamamoto, Y.; Miyaura, N. *Materials Research Bulletin* **2008,** 43, (2), 251-256.

95. Xu, L.; Peng, Y.; Meng, Z.; Yu, W.; Zhang, S.; Liu, X.; Qian, Y. *Chemistry of Materials* **2003,** 15, (13), 2675-2680.

96. Dai, J.; Xu, L.; Fang, Z.; Sheng, D.; Guo, Q.; Ren, Z.; Wang, K.; Qian, Y. *Chemical Physics Letters* **2007,** 440, (4), 253-258.

97. Chatterjee, S.; Kim, M. J.; Zakharov, D. N.; Kim, S. M.; Stach, E. A.; Maruyama, B.; Sneddon, L. G. *Chemistry of Materials* **2012,** 24, (15), 2872-2879.

98. Ma, R.; Bando, Y.; Sato, T. *Chemical Physics Letters* **2001,** 337, (1), 61-64.

99. Ma, R.; Bando, Y.; Sato, T.; Kurashima, K. *Chemical Physics Letters* **2001,** 350, (5), 434-440.

100. Ma, R.; Bando, Y.; Sato, T.; Kurashima, K. *Chemistry of Materials* **2001,** 13, (9), 2965-2971.

101. Guo, L.; Singh, R. N. *Nanotechnology* **2008,** 19, (6), 065601.

102. Guo, L.; Singh, R. N. *Physica E: Low-dimensional Systems and Nanostructures* **2009,** 41, (3), 448-453.

103. Su, C.-Y.; Chu, W.-Y.; Juang, Z.-Y.; Chen, K.-F.; Cheng, B.-M.; Chen, F.-R.; Leou, K.-C.; Tsai, C.-H. *The Journal of Physical Chemistry C* **2009,** 113, (33), 14732-14738.

104. Tang, C. C.; Lamy de la Chapelle, M.; Li, P.; Liu, Y. M.; Dang, H. Y.; Fan, S. S. *Chemical Physics Letters* **2001,** 342, (5), 492-496.

105. Wei, X.; Wang, M.-S.; Bando, Y.; Golberg, D. *Advanced Materials* **2010,** 22, (43), 4895-4899.

106. Yamaguchi, M.; Tang, D.-M.; Zhi, C.; Bando, Y.; Shtansky, D.; Golberg, D. *Acta Materialia* **2012,** 60, (17), 6213-6222.

107. Tang, C. C.; Bando, Y.; Sato, T. *Applied Physics A* **2002,** 75, (6), 681-685.

108. Tang, C.; Bando, Y.; Golberg, D. *Journal of Solid State Chemistry* **2004,** 177, (8), 2670-2674.

109. Yang, H.; Yoshio, B.; Chengchun, T.; Chunyi, Z.; Takeshi, T.; Benjamin, D.; Takashi, S.; Dmitri, G. *Nanotechnology* **2009,** 20, (8), 085705.

110. Sinitskii, A.; Erickson, K. J.; Lu, W.; Gibb, A. L.; Zhi, C.; Bando, Y.; Golberg, D.; Zettl, A.; Tour, J. M. *ACS Nano* **2014,** 8, (10), 9867-9873.

111. Maria Nithya, J. S.; Pandurangan, A. *RSC Advances* **2014,** 4, (51), 26697-26705.

112. Wang, L.; Li, T.; Long, X.; Wang, X.; Xu, Y.; Yao, Y. *Nanoscale* **2017,** 9, (5), 1816-1819.

113. Ferreira, T. H.; Silva, P. R. O.; Santos, R. G.; Sousa, E. M. B. *Journal of Biomaterials and Nanobiotechnology* **2011,** Vol.02No.04, 9.

114. Seo, D.; Kim, J.; Park, S.-H.; Jeong, Y.-U.; Seo, Y.-S.; Lee, S.-H.; Kim, J. *Journal of Industrial and Engineering Chemistry* **2013,** 19, (4), 1117-1122.

115. Özmen, D.; Sezgi, N. A.; Balcı, S. *Chemical Engineering Journal* **2013,** 219, 28-36.

116. Kalay, S.; Yilmaz, Z.; Çulha, M. *Beilstein Journal of Nanotechnology* **2013,** 4, 843-851.

117. Yördem, O. S.; Papila, M.; Menceloğlu, Y. Z. *Materials & Design* **2008,** 29, (1), 34-44.

118. Khuri, A. I.; Cornell, J. A., *Response surfaces: designs and analyses*. CRC press: 1996; Vol. 152.

119. Tang, C. C.; Ding, X. X.; Huang, X. T.; Gan, Z. W.; Qi, S. R.; Liu, W.; Fan, S. S. *Chem Phys Lett* **2002,** 356.

120. Zhi, C.; Bando, Y.; Tan, C.; Golberg, D. *Solid State Commun* **2005,** 135.

121. Zhuang, C.; Xu, H.; Li, L.; Liu, Y.; Ban, C.; Liu, X. *RSC Advances* **2016,** 6, (114), 113415-113423.

122. Merkulov, V. I.; Melechko, A. V.; Guillorn, M. A.; Lowndes, D. H.; Simpson, M. L. *Applied Physics Letters* **2001,** 79, (18), 2970-2972.

123. Kuhner, G.; Knorre, H., Production of boron nitride. Google Patents: 1968.

124. Terauchi, M.; Tanaka, M.; Suzuki, K.; Ogino, A.; Kimura, K. *Chemical Physics Letters* **2000,** 324, (5), 359-364.

125. Bartnitskaya, T. S.; Lyashenko, V. I.; Kurdyumov, A. V.; Ostrovskaya, N. F.; Rogovaya, I. G. *Powder Metallurgy and Metal Ceramics* **1995,** 33, (7), 335-340.

126. Bartnitskaya, T. S.; Kurdyumov, A. V.; Lyashenko, V. I.; Ostrovskaya, N. F.; Rogovaya, I. G. *Powder Metallurgy and Metal Ceramics* **1996,** 35, (5), 296-300.

127. Howard, S. *SD School of Mines and Technology, Rapid City, SD* **2006**.

128. Kotarba, A.; Barański, A.; Hodorowicz, S.; Sokołowski, J.; Szytuła, A.; Holmlid, L. *Catalysis Letters* **2000,** 67, (2), 129-134.

129. Meima, G. R.; Menon, P. G. *Applied Catalysis A: General* **2001,** 212, (1), 239-245.

130. Joseph, Y.; Ketteler, G.; Kuhrs, C.; Ranke, W.; Weiss, W.; Schlogl, R. *Physical Chemistry Chemical Physics* **2001,** 3, (18), 4141-4153.

131. Ndlela, S. C.; Shanks, B. H. *Industrial & Engineering Chemistry Research* **2003,** 42, (10), 2112-2121.

132. Nemanich, R. J.; Solin, S. A.; Martin, R. M. *Physical Review B* **1981,** 23, (12), 6348-6356.

133. Wu, J.; Han, W.-Q.; Walukiewicz, W.; Ager, J. W.; Shan, W.; Haller, E. E.; Zettl, A. *Nano Letters* **2004,** 4, (4), 647-650.

134. Arenal, R.; Ferrari, A. C.; Reich, S.; Wirtz, L.; Mevellec, J. Y.; Lefrant, S.; Rubio, A.; Loiseau, A. *Nano Letters* **2006,** 6, (8), 1812-1816.

135. Celik-Aktas, A.; Zuo, J.-M.; Stubbins, J. F.; Tang, C.; Bando, Y. *Acta Crystallographica Section A* **2005,** 61, (6), 533-541.

136. Golberg, D.; Mitome, M.; Bando, Y.; Tang, C. C.; Zhi, C. Y. *Applied Physics A* **2007,** 88, (2), 347-352.

137. Garel, J.; Leven, I.; Zhi, C.; Nagapriya, K. S.; Popovitz-Biro, R.; Golberg, D.; Bando, Y.; Hod, O.; Joselevich, E. *Nano Letters* **2012,** 12, (12), 6347-6352.

138. Erickson, K. J.; Gibb, A. L.; Sinitskii, A.; Rousseas, M.; Alem, N.; Tour, J. M.; Zettl, A. K. *Nano Letters* **2011,** 11, (8), 3221-3226.

139. Wang, J.; Kayastha, V. K.; Yap, Y. K.; Fan, Z.; Lu, J. G.; Pan, Z.; Ivanov, I. N.; Puretzky, A. A.; Geohegan, D. B. *Nano Letters* **2005,** 5, (12), 2528-2532.

140. Kotarba, A.; Hagström, M.; Engvall, K.; Pettersson, J. B. C. *Catalysis Letters* **2004,** 95, (1), 93-97.

141. Yamaguchi, N.; Kobayashi, A.; Sodesawa, T.; Nozaki, F. *Reaction Kinetics and Catalysis Letters* **1984,** 25, (1), 11-15.

142. Chukeaw, T.; Seubsai, A.; Phon-in, P.; Charoen, K.; Witoon, T.; Donphai, W.; Parpainainar, P.; Chareonpanich, M.; Noon, D.; Zohour, B.; Senkan, S. *RSC Advances* **2016,** 6, (61), 56116-56126.

143. Ueshima, M.; Saito, N.; Shimizu, N., 1.6 Role of Acid and Base Properties of V2O5-Base Metal Oxide Catalysts for Partial Oxidation of p-Substituted Toluene. In *Studies in Surface Science and Catalysis*, Hattori, H.; Misono, M.; Ono, Y., Eds. Elsevier: 1994; Vol. 90, pp 59-66.

144. Hill, A. K.; Torrente-Murciano, L. *Applied Catalysis B: Environmental* **2015,** 172-173, (Supplement C), 129-135.

145. Hill, A. K.; Torrente-Murciano, L. *International Journal of Hydrogen Energy* **2014,** 39, (15), 7646-7654.

146. Srifa, A.; Okura, K.; Okanishi, T.; Muroyama, H.; Matsui, T.; Eguchi, K. *Applied Catalysis B: Environmental* **2017,** 218, (Supplement C), 1-8.

147. Anikanova, L. G.; Dvoretskii, N. V. *Catalysis in Industry* **2013,** 5, (1), 74-79.

148. Kano, Y.; Ohshima, M. a.; Kurokawa, H.; Miura, H. *Reaction Kinetics, Mechanisms and Catalysis* **2013,** 109, (1), 29-41.

149. Shekhtman, G. S.; Burmakin, E. I.; Antonov, B. D. *Russian Journal of Electrochemistry* **2012,** 48, (10), 1011-1016.

150. Campaña, A. G.; Fuentes, N.; Gómez-Bengoa, E.; Mateo, C.; Oltra, J. E.; Echavarren, A. M.; Cuerva, J. M. *The Journal of Organic Chemistry* **2007,** 72, (21), 8127-8130.

151. Mogilaiah, K.; Reddy, C. S. *Synthetic Communications* **2003,** 33, (18), 3131-3134.

152. Gopalakrishnan, M.; Sureshkumar, P.; Kanagarajan, V.; Thanusu, J. *Letters in Organic Chemistry* **2005,** 2, (5), 444-446.

153. Leung, D. Y. C.; Guo, Y. *Fuel Processing Technology* **2006,** 87, (10), 883-890.

154. Sato, S.; Ohhara, M.; Sodesawa, T.; Nozaki, F. *Applied Catalysis* **1988,** 37, (Supplement C), 207-215.

155. Nguyen, T. S.; Lefferts, L.; Sai Sankar Gupta, K. B.; Seshan, K. *ChemCatChem* **2015,** 7, (12), 1833-1840.

156. Okada, S.

157. Zhao, J.; Zhao, L.; Dimov, N.; Okada, S.; Nishida, T. *Journal of The Electrochemical Society* **2013,** 160, (5), A3077-A3081.

158. Schmitt, W.; Hill, J. P.; Malik, S.; Volkert, C. A.; Ichinose, I.; Anson, C. E.; Powell, A. K. *Angewandte Chemie International Edition* **2005,** 44, (43), 7048-7053.

159. Wei, H.; Ren, Y.; Wang, A.; Liu, X.; Liu, X.; Zhang, L.; Miao, S.; Li, L.; Liu, J.; Wang, J.; Wang, G.; Su, D.; Zhang, T. *Chemical Science* **2017,** 8, (7), 5126-5131.

160. Blesa, M. C.; Amador, U.; Morán, E.; Menéndez, N.; Tornero, J. D.; Rodríguez-Carvajal, J. *Solid State Ionics* **1993,** 63-65, (Supplement C), 429-436.

161. Takeda, Y.; Akagi, J.; Edagawa, A.; Inagaki, M.; Naka, S. *Materials Research Bulletin* **1980,** 15, (8), 1167-1172.

162. El-Shobaky, G. A.; Ibrahim, A. A.; El-Defrawy, S. *Thermochimica Acta* **1988,** 131, (Supplement C), 115-123.

163. Matveev, A. T.; Firestein, K. L.; Steinman, A. E.; Kovalskii, A. M.; Lebedev, O. I.; Shtansky, D. V.; Golberg, D. *Nano Research* **2015,** 8, (6), 2063-2072.

164. Wang, C.; Yu, H.; Liu, H. S.; Jin, Z. P. *J. Phase Equilib.* **2003,** 24, (1), 12-20.

165. Çamurlu, H. E. *Ceramics International* **2011,** 37, (6), 1993-1999.

166. Armstrong, A. R.; Tee, D. W.; La Mantia, F.; Novák, P.; Bruce, P. G. *Journal of the American Chemical Society* **2008,** 130, (11), 3554-3559.

167. Abdel-Ghany, A. E.; Mauger, A.; Groult, H.; Zaghib, K.; Julien, C. M. *Journal of Power Sources* **2012,** 197, (Supplement C), 285-291.

168. Wang, J.; Gu, Y.; Li, Z.; Du, X.; Zhang, Z.; Wang, W.; Wang, Y.; Wang, H.; Fu, Z. *CrystEngComm* **2014,** 16, (13), 2746-2753.

169. Zhang, L.; Liu, C.; Liu, B.; Yu, W.-J.; Hou, P.-X.; Cheng, H.-M. *Carbon* **2013,** 55, (Supplement C), 253-259.